Ultimate behavior of confined fluids under very high pressure and shear stress

Serigne Ndiaga Ndiaye

N°d'ordre NNT : 2017LYSEI104

THESE de DOCTORAT DE L'UNIVERSITE DE LYON

INSA de Lyon

Ecole Doctorale N° 162

Mécanique, Energétique, Génie civil, Acoustique (MEGA)

Spécialité/ discipline de doctorat :

Génie Mécanique

Soutenue publiquement le 03/11/2017, par :

Serigne Ndiaga Ndiaye

Ultimate behavior of confined fluids under very high pressure and shear stress

---

Devant le jury composé de :

BRUNETIERE, Noël	Chargé de Recherche HDR Université de Poitiers	Rapporteur
MARTINIE, Laetitia	Maître de Conférences INSA de Lyon	Co-directrice de thèse
PHILIPPON, David	Maître de Conférences INSA de Lyon	Examinateur
POLL, Gerhard	Professeur, Leibniz Universitaet Hannover	Rapporteur
SEABRA, Jorge	Professeur, Universidade do Porto	Examinateur
VERGNE, Philippe	Directeur de Recherches	Directeur de thèse
MARGUERITAT, Jérémie	Chargé de Recherche, UCBL1	Invité
MORALES-ESPEJEL, Guillermo	Principal Scientist, SKF-ERC	Invité

Département FEDORA – INSA Lyon - Ecoles Doctorales – Quinquennal 2016 2020

SIGLE	ECOLE DOCTORALE	NOM ET COORDONNEES DU RESPONSABLE
CHIMIE	**CHIMIE DE LYON** **http://www.edchimie-lyon.fr** Sec : Renée EL MELHEM Bat Blaise Pascal 3e etage secretariat@edchimie-lyon.fr Insa : R. GOURDON	M. Stéphane DANIELE Institut de Recherches sur la Catalyse et l'Environnement de Lyon IRCELYON-UMR 5256 Équipe CDFA 2 avenue Albert Einstein 69626 Villeurbanne cedex directeur@edchimie-lyon.fr
E.E.A.	**ELECTRONIQUE, ELECTROTECHNIQUE, AUTOMATIQUE** **http://edeea.ec-lyon.fr** Sec : M.C. HAVGOUDOUKIAN Ecole-Doctorale.eea@ec-lyon.fr	M. Gérard SCORLETTI Ecole Centrale de Lyon 36 avenue Guy de Collongue 69134 ECULLY Tél : 04.72.18 60.97 Fax : 04 78 43 37 17 Gerard.scorletti@ec-lyon.fr
E2M2	**EVOLUTION, ECOSYSTEME, MICROBIOLOGIE, MODELISATION** **http://e2m2.universite-lyon.fr** Sec : Sylvie ROBERJOT Bât Atrium - UCB Lyon 1 04.72.44.83.62 Insa : H. CHARLES secretariat.e2m2@univ-lyon1.fr	M. Fabrice CORDEY CNRS UMR 5276 Lab. de géologie de Lyon Université Claude Bernard Lyon 1 Bât Géode 2 rue Raphaël Dubois 69622 VILLEURBANNE Cédex Tél : 06.07.53.89.13 cordey@ univ-lyon1.fr
EDISS	**INTERDISCIPLINAIRE SCIENCESSANTE** **http://www.edisslyon.fr** Sec : Sylvie ROBERJOT Bât Atrium - UCB Lyon 1 04.72.44.83.62 Insa : M. LAGARDE secretariat.ediss@univ-lyon1.fr	Mme Emmanuelle CANET-SOULAS INSERM U1060, CarMeN lab, Univ. Lyon 1 Bâtiment IMBL 11 avenue Jean Capelle INSA de Lyon 696621 Villeurbanne Tél : 04.72.68.49.09 Fax :04 72 68 49 16 Emmanuelle.canet@univ-lyon1.fr
INFOMATHS	**INFORMATIQUE ET MATHEMATIQUES** **http://edinfomaths.universite-lyon.fr** Sec : Renée EL MELHEM Bat Blaise Pascal, 3e étage Tél : 04.72. 43. 80. 46 Fax : 04.72.43.16.87 infomaths@univ-lyon1.fr	M. Luca ZAMBONI Bâtiment Braconnier 43 Boulevard du 11 novembre 1918 69622 VILLEURBANNE Cedex Tél :04 26 23 45 52 zamboni@maths.univ-lyon1.fr

Matériaux	**MATERIAUX DE LYON** **http://ed34.universite-lyon.fr** Sec : Marion COMBE Tél:04-72-43-71-70 –Fax : 87.12 Bat. Direction ed.materiaux@insa-lyon.fr	M. Jean-Yves BUFFIERE INSA de Lyon MATEIS Bâtiment Saint Exupéry 7 avenue Jean Capelle 69621 VILLEURBANNE Cedex Tél : 04.72.43 71.70 Fax 04 72 43 85 28 Ed.materiaux@insa-lyon.fr
MEGA	**MECANIQUE, ENERGETIQUE, GENIE CIVIL, ACOUSTIQUE** **http://edmega.universite-lyon.fr/** Sec : Marion COMBE Tél:04-72-43-71-70 –Fax : 87.12 Bat. Direction mega@insa-lyon.fr	M. Philippe BOISSE INSA de Lyon Laboratoire LAMCOS Bâtiment Jacquard 25 bis avenue Jean Capelle 69621 VILLEURBANNE Cedex Tél : 04.72 .43.71.70 Fax : 04 72 43 72 37 Philippe.boisse@insa-lyon.fr
ScSo	**ScSo*** **http://ed483.univ-lyon2.fr/** Sec : Viviane POLSINELLI Brigitte DUBOIS Insa : J.Y. TOUSSAINT Tél : 04 78 69 72 76 viviane.polsinelli@univ-lyon2.fr	M. Christian MONTES Université Lyon 2 86 rue Pasteur 69365 LYON Cedex 07 Christian.montes@univ-lyon2.fr

*ScSo : Histoire, Géographie, Aménagement, Urbanisme, Archéologie, Science politique, Sociologie, Anthropologie

Comportement ultime des fluides confinés sous forte pression et contrainte de cisaillement

Résumé

L'étude du frottement dans les contacts lubrifiés fortement chargés est un sujet complexe. En effet, le frottement dépend fortement du comportement rhéologique du lubrifiant dans le centre du contact et, celui-ci n'est pas bien connu à pression et taux de cisaillement élevé. Diverses méthodes expérimentales ont été développées pour expliquer le comportement plateau dans les courbes de frottement, associé à l'existence d'une contrainte limite de cisaillement, mais aucune d'elles n'a fourni une image complète des mécanismes réels impliqués. Dans la continuité de ces efforts, des études sont présentées dans ce mémoire.

Le premier défi dans ce travail est d'effectuer des mesures de frottement dans des conditions isothermes nominales, ce qui signifie que même si des effets thermiques doivent se produire dans toute mesure de frottement, il est possible de les minimiser et de rendre les résultats insensibles à une faible dissipation d'énergie dans le volume expérimental d'intérêt. La minimisation de l'échauffement du lubrifiant aide à se focaliser sur l'origine mécanique de la contrainte limite de cisaillement et de mieux caractériser sa dépendance à la pression et à la température. C'est pourquoi, tout d'abord, une série d'expériences a été réalisée sur deux lubrifiants, un diester pur (benzyl benzoate) et une huile minérale de turbine (Shell T9) avec des vitesses d'entraînement variables. Cela nous permet d'abord d'observer directement l'influence des effets thermiques sur les valeurs de la contrainte limite de cisaillement et ensuite, de déterminer les conditions expérimentales qui limitent ces effets tout en assurant un régime en film complet.

Le deuxième objectif est de caractériser le comportement en frottement des lubrifiants sous conditions isothermes nominales et sur une large gamme de pression (jusqu'à 3 GPa) et de température (jusqu'à 80°C) afin d'établir un nouveau modèle découplé permettant de décrire la dépendance à la température et à la pression de la contrainte limite sous fortes charges.

Enfin, l'étude se focalise sur la compréhension du comportement microscopique des lubrifiants dans des conditions extrêmes de cisaillement et de pression. Des mesures in situ de spectroscopie Raman et Brillouin ont été également effectuées sous conditions statiques, afin d'étudier le changement de phase du lubrifiant.

Mots clés : contrainte limite de cisaillement, lubrification élastohydrodynamique, contacts lubrifiés fortement chargés, mesure in situ, coefficient de frottement, transition vitreuse.

Ultimate behavior of confined fluids under very high pressure and shear stress

Abstract

Friction in highly loaded lubricated contacts is a complex issue. Indeed, it highly depends on the lubricant rheological behaviour in the Hertzian region, which is not well known under such high pressure and high shear stress. Various experimental methods have been developed to explain the plateau-like behaviour in friction curves referred to as the limiting shear stress (LSS), but none of them provided a full picture of the real mechanisms involved. In a continuation of these efforts, some investigations are presented in this manuscript.

The first challenge in this work is to carry out friction measurements under nominal isothermal conditions, meaning that even if thermal effects must occur in any friction measurement, it is possible to minimize them and to make the results almost insensitive to a weak energy dissipation within the experimental volume of interest. Minimizing shear heating of the lubricant help us to focus on the mechanical origin of the LSS and to better characterize its dependence to pressure and temperature. That's why, first of all, a series of experiments was performed on two lubricants, a pure diester fluid (benzyl benzoate), and a commercial turbine mineral oil (Shell T9) with varying entrainment velocities. This allow us first to directly observe the influence of the lubricant shear heating on the LSS values and then to determine the experimental conditions which limit this thermal effect while ensuring a full film regime.

The second objective is to characterize the frictional behavior of both lubricants under nominal isothermal conditions and over a wide range of pressure (up to 3 GPa) and temperature (up to 80°C) in order to establish a new uncoupled model to describe the temperature and pressure dependence of the limiting shear stress under highly loaded conditions.

Finally, the study focuses on the understanding of the microscopic behavior of lubricants under extreme shear and pressure conditions. In situ Raman and Brillouin spectroscopy investigations were also conducted under static conditions, in order to study the lubricant phase changes under various pressure and temperature conditions.

Keywords: limiting shear stress, elastohydrodynamic lubrication, highly loaded contacts, in situ measurement, friction coefficient, glass transition.

Table of contents

List of figures

List of tables

Nomenclature

a_{Hertz}	Hertzian radius of contact (mm)
$A_1, A_2, b_1, b_2, C_1, C_2$	Modified WLF constants (-)
CF_X	Friction coefficient (-)
C_p	Specific heat capacity (J/kgK)
E	Young's modulus (GPa)
E_{eq}	Reduced Young's modulus (GPa)
$F(P)$	variation of the thermal expansion coefficient with pressure (GPa)
F_X	Friction force (N)
F_Z	Normal load (N)
G	Shear modulus (GPa)
G_∞	Limiting elastic shear modulus (GPa)
G_{eq}	Equivalent shear modulus (GPa)
G_1	Shear modulus of the ball (GPa)
G_2	Shear modulus of the disc (GPa)
h_c	Central film thickness (nm)
h_m	Minimum film thickness (nm)
k	Thermal conductivity (W/mK)
P	Pressure (GPa)
$\bar{P}$	Mean contact pressure $= \frac{2}{3} P_{Hertz}$ (MPa)
P_g	Mean contact pressure (GPa)
P_{Hertz}	Hertzian contact pressure (GPa)
P_{atm}	Atmospheric pressure (MPa)
R_{eq}	Equivalent radius (°C)
r_s	Solid ratio (-)
r_f	Fluid ratio (-)
T_R	Reference temperature (°C)
S	Contact surface (mm^2)
T	Temperature (°C)
T_g	Glass transition temperature (°C)
T_{in}	Inlet temperature (°C)
T_R	Reference temperature (°C)
T_0	Ambient temperature (°C)
U_{ball}	Ball velocity (m/s)

U_{disc}	Ball velocity (m/s)
U_e	Entrainment velocity (m/s)
ΔU	Sliding velocity (m/s)
τ	Shear stress (Pa)
τ_0	Reference shear stress (Pa)
$\bar{\tau}$	Mean shear stress (Pa)
τ_L	Limiting shear stress (MPa)
$\bar{\tau_L}$	Mean limiting shear stress (MPa)
τ_{L0}	Limiting shear stress extrapolated at ambient pressure (MPa)
γ	Limiting shear stress pressure coefficient (-)
β	Limiting shear stress temperature coefficient (MPa/°C)
$\dot{\gamma}$	Shear rate (s^{-1})
η_0	Viscosity of the lubricant at atmospheric pressure (Pa.s)
η / μ	Viscosity of the lubricant for a given pressure (Pa.s)
μ_g	Viscosity of the lubricant at glassy state (Pa.s)
$\bar{\eta}$	Mean effective viscosity (Pa.s)
η_{eff}	Effective viscosity of the lubricant (Pa.s)
α^*	Reciprocal asymptotic isoviscous pressure (GPa^{-1})
ν	Poisson's coefficient (-)
ν_{eq}	Equivalent Poisson's coefficient (-)
ν_1	Poisson's coefficient of the ball (-)
ν_2	Poisson's coefficient of the disc (-)
ν_0	Frequency of the incident radiation (GHZ)
$\bar{\nu}$	Wave number (cm^{-1})
ρ	Density (kg/m^3)
$\sigma_{specimen}^{RMS}$	RMS roughness of a specimen (nm)
Σ	Combined roughness of the specimen surfaces (nm)
ϕ_T	Film thickness thermal reduction coefficient according Cheng (-)
$\Delta\upsilon_B$	Brillouin frequency (cm^{-1})
n	Refractive index (-)
λ_0	Excitation wavelength (nm)
$FWHM$	Full width at half maximum

Abbreviations

EHD	Elastohydrodynamic
EHL	Elastohydrodynamic Lubrication
$FWHM$	Full width at half maximum
LSS	Limiting shear stress
SRR	Slide-to-roll ratio
SRR_{LSS}	Slide-to-roll ratio at LSS onset

Résumé étendu

Introduction et objectifs

Le frottement est un mécanisme de dissipation d'énergie rencontré dans la vie quotidienne, comme lors du frottement des deux mains, du brossage des dents, etc. Il a des effets positifs comme des effets négatifs, l'homme ne pourrait pas marcher sans frottement, la tenue d'une voiture sur une route dépend directement du frottement entre les pneus et la route. Généralement, le frottement généré par le mouvement relatif des surfaces en contact est exprimé par un coefficient qui tient compte de plusieurs facteurs, tels que la déformation élastique des solides, la rugosité des surfaces en contact, la pression, l'adhérence des surfaces, etc. Les premières études sur le frottement ont été réalisées par Leonardo da Vinci (1452-1519) : il a mesuré la force minimale requise pour faire glisser une masse sur une surface. Des années plus tard, Amontons [1] et Coulomb [2] ont mené d'autres études sur le frottement. De leurs expériences découlent trois lois de frottement :

- la force de frottement est directement proportionnelle à la charge normale appliquée,
- la force de frottement est indépendante de la surface de glissement,
- la force de frottement est indépendante de la vitesse de glissement relative des surfaces.

L'étude du frottement, de la lubrification et de l'usure a été successivement établie par Hertz [3], Reynolds [4], et Bowden et Tabor [5]. Le frottement conduit à une consommation d'énergie dans un système mécanique. Ainsi, la réduction du frottement aide à améliorer l'efficacité des systèmes mécaniques (moteur à combustion, turbine, compresseur, etc.).

Une façon de réduire le frottement dans les contacts est la lubrification. Le lubrifiant peut être liquide, gazeux ou même solide. En plus de réduire le frottement et l'usure, les huiles lubrifiantes sont également nécessaires pour remplir d'autres fonctions, telles que la prévention de la corrosion, l'évacuation de la chaleur et des particules d'usure dans le contact [6, 7]. Pour les huiles moteur, la différence de consommation en carburant entre une huile optimisée de faible frottement et une huile standard peut atteindre 5% [8]. Récemment, Holmberg *et al.* [9] ont montré que près d'un tiers du carburant est dépensé pour surmonter le frottement dans les voitures particulières. Les pertes par frottement direct, freinage exclus, représentent 28% de l'énergie du combustible. Au total, 21.5% de l'énergie du combustible est utilisé pour déplacer la voiture. Les pertes d'énergie dues au frottement dans les voitures pourraient être réduites de 18% au cours des 5 à 10 prochaines années, ce qui entraînerait des économies globales de carburant de 117 000 millions de litres chaque année, de 61% au cours des 15 à 25 prochaines années, et génèrerait des économies de carburant de 385 000 millions de litres chaque année [10]. En conséquence, l'amélioration de l'efficacité énergétique dans les voitures particulières réduirait les émissions de CO_2 respectivement 290 millions et 960 millions de tonnes par an. Aujourd'hui, des efforts considérables sont consacrés à la

réduction des pertes d'énergie, non seulement pour des raisons économiques, mais aussi pour lutter contre le réchauffement climatique. L'Union Européenne vise à limiter l'émission de dioxyde de carbone dans les voitures à moins de 95 $gCO_2.km^{-1}$ en 2020 [11]. La réduction du frottement, de l'usure et la stabilité du lubrifiant sont les paramètres les plus importants à prendre en compte pour évaluer l'impact environnemental des lubrifiants.

Motivations industrielles et défis scientifiques

Les progrès technologiques dans le domaine de la lubrification et les questions environnementales ont conduit aux industriels à fournir des roulements de hautes performances sur le marché. Le marché mondial des roulements à billes a été évalué à 81,6 milliards d'USD en 2015 et devrait croître de manière significative (Figure 0-1), en raison de l'augmentation de la fabrication de machines lourdes.

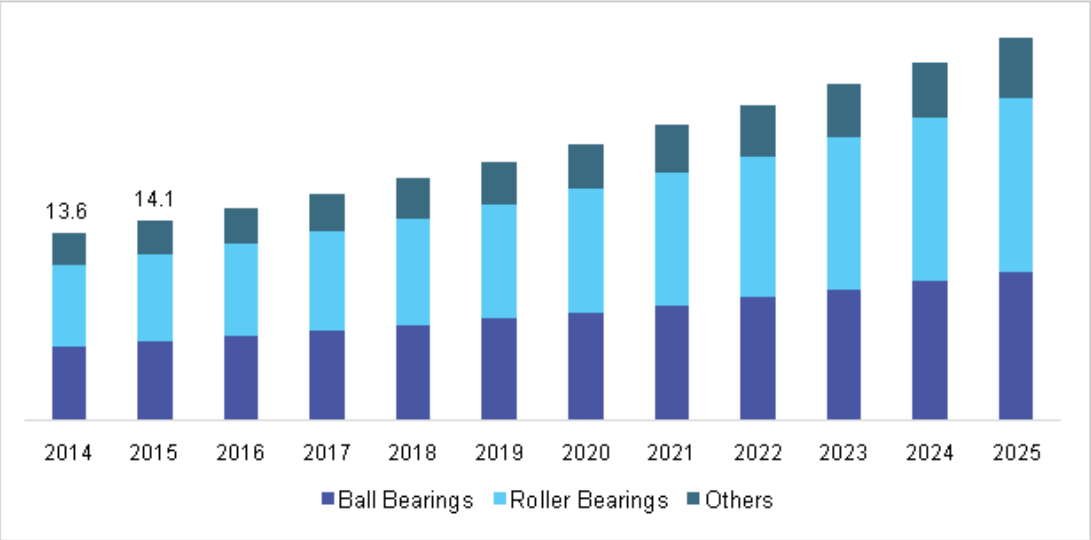

Figure 0-1 : Marché des roulements à billes par produit, 2014-2025 (en milliards de dollars). (http://www.grandviewresearch.com/industry-analysis/bearings-market).

L'un des défis techniques auxquels sont confrontés les industriels est comment réduire le frottement dans les roulements à billes afin de diminuer la consommation d'énergie due au frottement. En effet, la réduction des pertes d'énergie dans les roulements peut améliorer leur efficacité et permettre une diminution de leurs coûts de production. Le potentiel d'économie d'énergie est considérable car les roulements sont largement utilisés dans de nombreuses applications. En outre, la fabrication de roulements de haute qualité permettra de réduire la pollution de l'air par la diminution des émissions de CO_2. Cependant, il devient nécessaire de pouvoir estimer avec précision les pertes par frottement afin d'optimiser leur conception. Le frottement est l'un des principaux indicateurs de performance pour un roulement, et il est principalement régi par le mécanisme de lubrification. Les roulements à billes fonctionnent

dans le régime de lubrification élastohydrodynamique (EHL). La compréhension du frottement dans les contacts lubrifiés fortement chargés aidera à réduire le frottement dans les roulements à billes.

La principale motivation industrielle de ce travail est donc d'améliorer la prédiction du frottement dans les contacts lubrifiés fortement chargés comme ceux rencontrés dans les roulements à billes. Cela permettra d'optimiser leur durée de vie et leurs performances.

Objectifs et problématique de l'étude

La pression générée dans les contacts élastohydrodynamique (EHD) est suffisamment élevée pour induire une déformation élastique significative des surfaces en contact. Le coefficient de frottement dépend, parmi d'autres paramètres, de la vitesse de glissement relative (donnée par le rapport slide-to-roll-ratio, SRR) entre les deux corps solides. Expérimentalement, dans la gamme de pressions de contact modérées et à faible valeur de SRR, le coefficient de frottement augmente avec le SRR. Cependant, pour des pressions de contact élevées, le coefficient de frottement présente un comportement semblable à un plateau, qui est représentatif de ce qu'on appelle la contrainte limite de cisaillement (limiting shear stress, LSS). Plusieurs scénarios sont proposés dans la littérature pour tenter d'expliquer ses origines physiques. Cependant, la LSS n'a jamais été mesurée simultanément pour valider l'un d'entre eux. Par conséquent, il est important de comprendre les phénomènes responsables de la LSS afin de prédire avec précision le coefficient de frottement dans les contacts fortement chargés. Cette thèse est donc consacrée à l'étude du frottement dans les contacts circulaires fortement chargés. Une compréhension plus approfondie des caractéristiques et du comportement de ces contacts est nécessaire pour améliorer la prédiction du frottement dans les roulements à billes. Des expériences ont été effectuées sur deux lubrifiants, un composé organique, le benzyl benzoate et une huile minérale pour turbine, T9.

Ce manuscrit est organisé en trois chapitres : le premier présente un état de l'art des différents scénarios de LSS proposés dans la littérature pour expliquer son origine physique. Certaines équations trouvées dans la littérature pour décrire le comportement du lubrifiant dans des conditions extrêmes de pression, de température et de vitesse de cisaillement sont présentées. Ensuite, les différents modèles existants pour décrire la dépendance à la pression et à la température de la LSS sont présentés.

Le deuxième chapitre est divisé en deux sections : l'influence de l'échauffement du lubrifiant sur la réponse en frottement est étudiée dans la première. Cette partie vise à définir des conditions expérimentales optimales pour éviter au mieux cet échauffement. La seconde est consacrée à évaluer la relation entre pression, température et LSS.

Le troisième chapitre est consacré à l'étude du comportement du lubrifiant sous haute pression. Dans cette partie, nous nous sommes concentrés sur le régime linéaire du frottement (à très faible SRR (≤ 0.3%)) dans lequel une viscosité efficace a été déduite. Les spectroscopies Raman et Brillouin sont également utilisées pour étudier le changement de phase du lubrifiante sous pression, en condition statique.

Enfin, une conclusion générale est tirée des différents résultats présentés et discutés dans ce travail.

Etat de l'art : scénarios de la LSS, modèles de LSS

Scénarios de la LSS

Cette section rapporte les différents scenarios proposés dans la littérature pour expliquer l'origine physique de la LSS.

Glissement au niveau des parois

En mécanique des fluides, il est souvent admis qu'il y'a pas de glissement à l'interface solide/liquide. Cette hypothèse a été largement utilisée pour la conception de roulements hydrodynamiques, d'engrenages, etc. Récemment, la validité de cette hypothèse est remise en question. En effet, dans certaines conditions opératoires, le glissement du fluide à l'interface a été démontré expérimentalement [12, 13] et validé par des simulations de dynamiques moléculaires [14]. Schnell a montré expérimentalement qu'il existe un glissement à l'interface eau/surface hydrophobe [15]. Ceci est aussi observé pour les liquides simples (comme l'hexadécane) et aussi pour les fluides complexes (comme les polymères) [16]. Des résultats expérimentaux [17] ont montré que le glissement à l'interface fluide/solide se produit si la contrainte de cisaillement critique à l'interface est plus petite que la contrainte limite de cisaillement du fluide. Différentes techniques expérimentales, telles que la redistribution de fluorescence après photo-blanchiment [18] et la microscopie atomique [12] ont été largement utilisées pour confirmer la présence du glissement à l'interface liquide/solide. Ce glissement à l'interface a été considéré comme responsable de l'apparition de la contrainte limite, mais cette hypothèse n'a pas confirmée par des mesures simultanées de frottement.

Localisation du cisaillement

Pour expliquer l'évolution du coefficient de frottement observé dans les contacts lubrifiés fortement chargés, Evans et Johnson [19] ont proposé que la transition non linéaire soit attribuée au modèle d'activation thermique d'Eyring et que la contrainte limite de cisaillement s'explique par l'apparition de bandes de cisaillement. En raison de la forte dépendance de la

viscosité du lubrifiant à la température, un cisaillement inhomogène peut avoir lieu à travers l'épaisseur de film. Des résultats expérimentaux récents ont montré que deux types de cisaillement localisé peuvent être observés : un cisaillement isotherme et non isotherme [20]. L'apparition de bandes de cisaillement a été observée expérimentalement par Bair *et al*. [21]. Selon Plint [22], la LSS est atteinte lorsque le cisaillement du lubrifiant devient localisé. Les résultats de Bair [23] suggèrent que les bandes de cisaillement sont à l'origine de la LSS.

Ecoulement de type plug

Jacobson [24] a été parmi les premiers à proposer que le lubrifiant ne se comporte pas comme un fluide dans un contact EHD. Selon lui, une zone très fine près des surfaces solides est cisaillée alors qu'une grande partie du film lubrifiant se comporte comme un noyau de solide ou un plug. Ce type d'écoulement peut être considéré comme un cas particulier de la localisation du cisaillement, avec un cisaillement localisé près des surfaces solides. La vélocimétrie par images de particules a été utilisée [25] pour mettre en évidence ce type d'écoulement du lubrifiant dans un contact EHD.

Changement de phase de lubrifiant

L'état de la structure d'un lubrifiant soumis à de forte pression (> 1 GPa) n'est pas bien compris. Plusieurs études expérimentales et numériques ont été réalisées afin de comprendre le comportement du lubrifiant dans un contact fortement chargé. Selon de nombreux auteurs, parmi lesquels Alsaad *et al*. [26], de nombreux lubrifiants sont dans l'état vitreux dans un contact EHD chargé. Par ailleurs, la transition vitreuse d'un lubrifiant dans le contact peut également affecter l'épaisseur du film : cela pourrait donc remettre en question la prédiction de l'épaisseur du film. Récemment, des mesures de profils de vitesse dans un contact EHD ont été réalisées dans des conditions de glissement pur [27] en utilisant la redistribution de fluorescence après photoblanchiment. Les profils de vitesse obtenus s'écartent des modèles linéaires prédits par l'équation de Reynolds et mettent en évidence l'existence d'un changement de phase du lubrifiant à haute pression, ce dernier étant considéré comme étant l'origine de la LSS.

Modèles de LSS

La dépendance de la LSS avec les conditions opératoires, notamment la température et la pression a été étudiée par plusieurs auteurs. Cependant, il n'existe pas de modèle général qui permet de décrire la variation de la LSS avec la pression et la température pour tous les lubrifiants (d'origine minérale ou synthétique). L'une des premières études portant sur les différents paramètres pouvant affecter la LSS a été réalisée par Johnson et Tevaarwerk [28]. Ils ont effectué des mesures de frottement en utilisant une machine à disque. À partir de leurs

expériences, ils on établit une relation linéaire de la contrainte limite de cisaillement avec la pression.

$$\tau_L = \tau_0 + \gamma p \qquad (0\text{-}1)$$

avec τ_0 la contrainte limite à pression nulle.
D'autres études ont été réalisées en utilisant une cellule haute pression [29, 30], une machine à disque [31, 32] ou l'impact d'une bille [32]. Cependant, les différentes modèles de LSS proposés sont tous différents les uns des autres. On peut noter aussi que dans ces modèles, il existe un terme de couplage entre pression et température. Ceci rend impossible la séparation des contributions mécanique et thermique sur la LSS et laisse penser que ce couplage entre pression et température pourrait être dû à l'échauffement du lubrifiant à vitesse de cisaillement élevée.

Dépendance de la contrainte limite de cisaillement avec la pression et la température

Comme mentionné précédemment, plusieurs modèles de LSS couplés ont été proposés dans la littérature pour décrire la dépendance de la LSS avec la pression et la température. En plus du terme de couplage, ces modèles incluent un coefficient pression-contrainte limite de cisaillement qui peut différer d'un auteur à l'autre.
On présente une approche phénoménologique pour décrire la dépendance de la LSS avec la pression et la température. Un modèle dérivé d'expériences de frottement menées dans des conditions isothermes nominales en utilisant un tribomètre bille sur disque est proposé. Dans un premier temps, des conditions expérimentales ont été définies pour réduire autant que possible l'échauffement du lubrifiant à l'entrée et dans le contact, afin de découpler les contributions mécaniques et thermiques sur LSS. Dans un deuxième temps, la dépendance de la LSS avec la pression et la température est étudiée pour deux types de lubrifiants, un fluide pur (benzyl benzoate) et une huile minérale de turbine (T9).

Propriétés des lubrifiants

Deux lubrifiants ont été testés. Le premier est le benzyl benzoate (acheté à abcr GmbH, pureté 99%, CAS 120-51-4), un composé organique de formule $C_6H_5CO_2CH_2C_6H_5$. Sa caractérisation rhéologique a été réalisée suivant l'approche décrite en détail dans [33]. Ses propriétés rhéologiques sur une large gamme de températures et de pressions sont décrites dans l'Annexe A. Le choix de ce lubrifiant a été motivé par son signal intense en spectroscopie Raman. Sa caractérisation optique sera décrite ultérieurement.

Le second fluide est une huile minérale de turbine (Shell T9). Cette dernière a été largement étudiée dans la littérature et les propriétés rhéologiques du lot spécifique utilisé dans ce mémoire sont décrites dans Wheeler *et al.* [34]. Ses propriétés rhéologiques sont données dans l'Annexe B.

Conditions opératoires

La première étape consiste à définir les conditions expérimentales qui permettent d'éviter l'échauffement du lubrifiant. En effet, la dissipation thermique tend à diminuer le coefficient de frottement au-delà d'une valeur critique de SRR. Cette section vise donc à trouver les conditions opératoires optimales pour limiter autant que possible l'influence des effets thermiques sur les mesures de frottement qui seront utilisées pour évaluer la dépendance à la pression et à la température de la LSS. Pour cela, une série d'expériences a été réalisée pour mettre en évidence la dépendance de la LSS à l'échauffement des deux lubrifiants.

Montage expérimental

Les mesures de frottement ont été réalisées sur un tribomètre bille sur disque appelé Jerotrib (Figure 0-2). Les deux éprouvettes sont entrainées indépendamment par deux moteurs équipés de codeurs optiques de 2.10^4 pas par tour, combinés à une discrétisation de 8 bits pour appliquer avec une grande précision toute valeur de SRR souhaitée. Trois configurations ont été utilisées: une bille en acier 100C6 contre un disque en acier 100C6 ou en saphir, et une bille en carbure de tungstène (WC) contre un disque en WC. Les propriétés des différents matériaux sont données dans le Tableau 0-1. La rugosité de surface des éprouvettes est pour la bille en acier $\sigma^{RMS}_{bille\ acier} \sim$ 5 nm, le disque acier $\sigma^{RMS}_{disque\ en\ acier} \sim$ 10 et le disque saphir $\sigma^{RMS}_{disque\ en\ saphir} \sim$ 8 nm. Pour les éprouvettes WC, la rugosité est la même pour la bille et le disque : $\sigma^{RMS}_{WC} \sim$ 20 nm. Le glissement relatif des deux spécimens ou SRR peut être exprimé comme suit:

$$SRR = \frac{\Delta U}{U_e} = 2\frac{U_{bille} - U_{disque}}{U_{bille} + U_{disque}} \quad (0\text{-}2)$$

$$U_e = \frac{U_{bille} + U_{disque}}{2} \quad (0\text{-}3)$$

avec U_e, la vitesse moyenne d'entrainement, U_{bille}, la vitesse de la bille et U_{disque}, la vitesse du disque. Le diamètre de l'éprouvette à bille est de 25.4 mm.

Matériaux	E (GPa)	ν (-)	ρ (kg/m^3)	k (W/mK)	C_p (J/kgK)
Acier 100 C6	210	0.30	7850	46	470
Saphir	360	0.34	4000	40	750
Carbure de tungstène (WC)	610	0.258	14850	29.3	194.7

Tableau 0-1 : Propriétés des matériaux utilisés.

Le rayon de contact sur le disque peut être compris entre 30 mm et 36 mm et est systématiquement contrôlé. Pour une vitesse d'entrainement U_e de 3 m/s et SRR = 1%, l'incertitude relative sur SRR est inférieure à 6% et cette valeur chute de manière significative lorsque le SRR augmente.

La charge normale maximale appliquée peut atteindre 400 N. Les forces normales et de frottement (F_Z and F_X, respectivement) sont mesurées simultanément à l'aide d'un capteur à jauge multiaxes avec une incertitude maximale de 0,82% pour la première et de 0,35% pour la dernière. Le coefficient de frottement, calculé comme le rapport entre la force tangentielle mesurée sur le disque et la charge normale appliquée sur la bille, présente une incertitude de $\Delta CF_X/CF_X = 1.17\%$. Les forces suivant les trois directions sont enregistrées en permanence à une fréquence de 100 Hz. Les forces de frottement obtenues à SRR de même intensité mais avec des signes opposés ont été systématiquement moyennées. En outre, certains tests ont été répétés, ce qui a entraîné un écart type relatif moyen (compte tenu des valeurs obtenues à SRR> 0 et SRR <0) de l'ordre de 2,8% avec une dispersion assez faible.

Le contact et le lubrifiant sont isolés thermiquement et maintenus à température constante par une boucle de fluide en circulation. La partie centrale du tribomètre a été conçue de manière à limiter tout transfert de chaleur vers la zone de contact, ce qui permet des conditions isothermes nominales lorsque des conditions opératoires appropriés sont appliquées.

Afin de minimiser les effets thermiques, la durée des paliers de frottement à chaque SRR appliqué est limitée à 10s, à l'exception de SRR = 0 où une durée de 30 s a été imposée pour permettre la stabilisation des conditions opératoires. La force de frottement mesurée, F_X est moyennée sur une durée de 7 s, en ignorant la première et les deux dernières secondes pour éliminer le temps de latence des moteurs. La température à l'entrée du contact, T_{in} est enregistrée tout au long de la mesure avec une précision de ± 0,1°C par une sonde de platine située juste en dessous de la de bille.

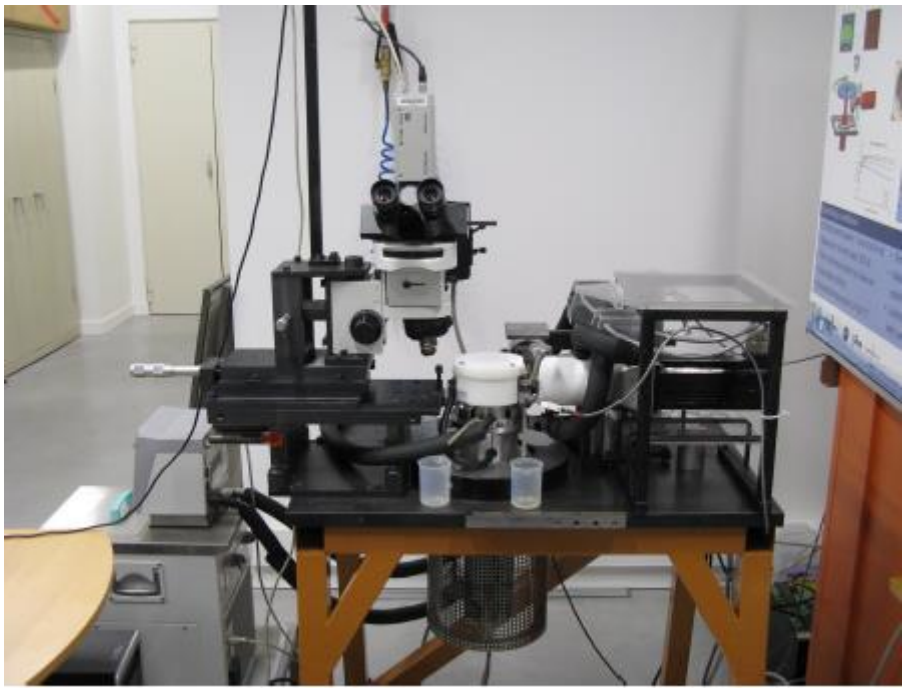

Figure 0-2 : Dispositif bille plan Jerotrib

Critère de contrainte limite de cisaillement

Comme montré dans le premier chapitre, à SRR moyen, le frottement peut présenter un comportement plateau associé à la contrainte limite de cisaillement (LSS). Dans cette étude, nous considérons que la LSS est atteinte lorsque la variation relative du coefficient de frottement entre deux valeurs de SRR successives ne dépasse pas l'incertitude de mesure sur le coefficient de frottement ($\Delta CF_X/CF_X = 1.17\%$). Ceci définit un critère de LSS qui a été appliqué à tous les résultats expérimentaux.

La LSS est défini comme étant la contrainte maximale que peut supporter un lubrifiant. Sa valeur moyenne, $\overline{\tau_L}$, est calculée en supposant que la LSS est atteinte dans toute la zone de contact. Il est calculé en divisant la force tangentielle maximale $max(F_X)$, par la surface de contact Hertzien S.

$$\overline{\tau_L} = \frac{max(F_X)}{S} \tag{0-4}$$

avec $S = \pi a^2$ et a le rayon Hertzien de contact

L'erreur relative sur la LSS est inférieure à 1.2%. Elle est obtenue à partir de la propagation des incertitudes :

$$\frac{\Delta\overline{\tau_L}}{\overline{\tau_L}} = \frac{\Delta F_X}{F_X} + \frac{2}{3} * \frac{\Delta F_Z}{F_Z} \tag{0-5}$$

L'influence de l'échauffement du lubrifiants sur la LSS

En régime EHL, la température dans le film lubrifiant peut augmenter de manière significative lorsque la vitesse de glissement (ou le SRR) augmente. L'augmentation de la température provient de deux principales sources de chaleur: l'échauffement du lubrifiant dû au cisaillement et l'échauffement par compression dû à des variations de pression dans la zone de contact. Ce dernier reste faible par rapport au premier. L'énergie générée par cisaillement chauffe le lubrifiant et réduit ainsi sa viscosité. L'étude des effets thermiques dans un contact EHL a été réalisée par Cheng [35]. Ses résultats numériques, prenant en compte à la fois le transfert de chaleur du lubrifiant aux surfaces solides et la convection, ont montré que le coefficient de frottement est affecté par l'augmentation de température dans le film [36]. Récemment, Habchi *et al*. [37] ont démontré que la LSS peut être influencée de manière significative par une augmentation de la température à travers le film de lubrifiant. En effet, négliger la chaleur générée à haute vitesse de glissement ou d'entraînement entraîne une surestimation des épaisseurs du film et aussi du coefficient de frottement. Ceci est dû à l'apparition d'effets thermiques importants à l'entrée et dans la zone centrale du contact, respectivement. Lorsque l'échauffement du lubrifiant prédomine sa réponse, le coefficient de frottement commence à décroitre.

Pour mettre en évidence l'influence des effets thermiques sur LSS, une série d'expériences a été effectué en premier sur le benzyl benzoate en variant U_e de 0.5 à 6.5 m/s. L'augmentation de la vitesse d'entraînement a des effets antagonistes. D'une part, elle tend à augmenter l'épaisseur du film selon la prédiction de Hamrock et Dowson [38]. Cependant elle conduit à une augmentation du taux de cisaillement, ce qui tend à augmenter la température du lubrifiant. Cette augmentation de température implique une diminution de la viscosité et donc une réduction de l'épaisseur du film. Plus U_e (ou SRR) est élevé, plus l'échauffement du lubrifiant est important.

Les expériences ont été réalisées avec une bille en acier et un disque en saphir. Pour chaque test, la pression appliquée est maintenue à P_{Hertz} = 1.68 GPa et la température T à 40 °C. Les conditions opératoires et les valeurs de LSS résultantes sont indiquées dans le Tableau 0-2 avec h_c, l'épaisseur centrale du film calculée avec l'expression de Hamrock et Dowson [38] et h_m, l'épaisseur minimale du film prédite à partir du model de Chevalier étendu [39]. Le coefficient de réduction thermique de l'épaisseur du film, ϕ_T, proposé par Cheng [36], a été calculé avant toute mesure. Il est représentatif de l'apparition d'effets thermiques significatifs à l'entrée de contact: $\phi_T \ll 1$ implique un échauffement important qui peut affecter la réponse du fluide alors qu'un ϕ_T proche de 1 représente un régime isotherme à l'entrée de contact. Seules les conditions opératoires donnant des valeurs de ϕ_T supérieures à 0.96 ont été retenues. En effet, dans de telles conditions, l'écoulement du lubrifiant peut être considéré

comme isotherme. ϕ_T est également donné dans le Tableau 0-2. Les résultats expérimentaux sont présentés sur la Figure 0-3, qui montre plus clairement les différentes variations. On observe que quelle que soit U_e, toutes les courbes de frottement se chevauchent bien à faible SRR. Pour les vitesses d'entraînement les plus faibles (0.5 et 0.8 m/s), CF_X augmente continument (même au-delà d'un SRR de 20%), tandis que pour les valeurs les plus élevées (5 et 6.5 m/s), il atteint un maximum très rapidement à faible SRR, puis diminue en raison des effets thermiques.

Pour chaque courbe de frottement, nous considérons que la LSS est atteinte si notre critère de stabilité défini précédemment est satisfait. Par conséquent, le SRR est étendu jusqu'à 20% pour certaines conditions opératoires. Les courbes de frottement ont conduit à différentes valeurs de LSS qui sont rapportées dans le Tableau 0-2, ainsi que le paramètre de lubrification h_m/Σ défini comme le rapport entre l'épaisseur minimale du film et la rugosité combinée des surfaces solides ($\Sigma = \sqrt{{\sigma_{bille}^{RMS}}^2 + {\sigma_{disque}^{RMS}}^2}$). Ce rapport est représentatif du régime de lubrification dans le contact. Un ratio de 3 est généralement considéré comme la limite entre le régime de lubrification dit film complet et le régime de mixte [40]. Les deux expériences à faible U_e peuvent être considérées comme étant dans le régime de lubrification mixte.

U_e (m/s)	0.5	0.8	1.5	1.5	2	2	2.5	3.5	5	6.5
φ_T (-)	1.0	0.99	0.99	0.99	0.99	0.99	0.98	0.97	0.96	0.95
h_c (nm)	31	43	65	65	79	79	92	115	146	174
h_m (nm)	< 10	13	20	20	25	25	31	43	60	76
h_m/Σ $(-)$	1	1.4	2.1	2.1	2.7	2.7	3.3	4.5	6.3	8
SRR_{LSS} (%)	17.5	17.5	10	12.5	10	10	7.5	5	5	4
$\overline{\tau_L}$ (MPa)	73.0	72.0	70.9	70.0	69.9	69.6	69.3	68.9	67.9	67.3

Tableau 0-2 : Conditions opératoires des mesures de frottement en acier/saphir et valeurs de LSS résultantes, benzyl benzoate à 40°C et 1.68 GPa

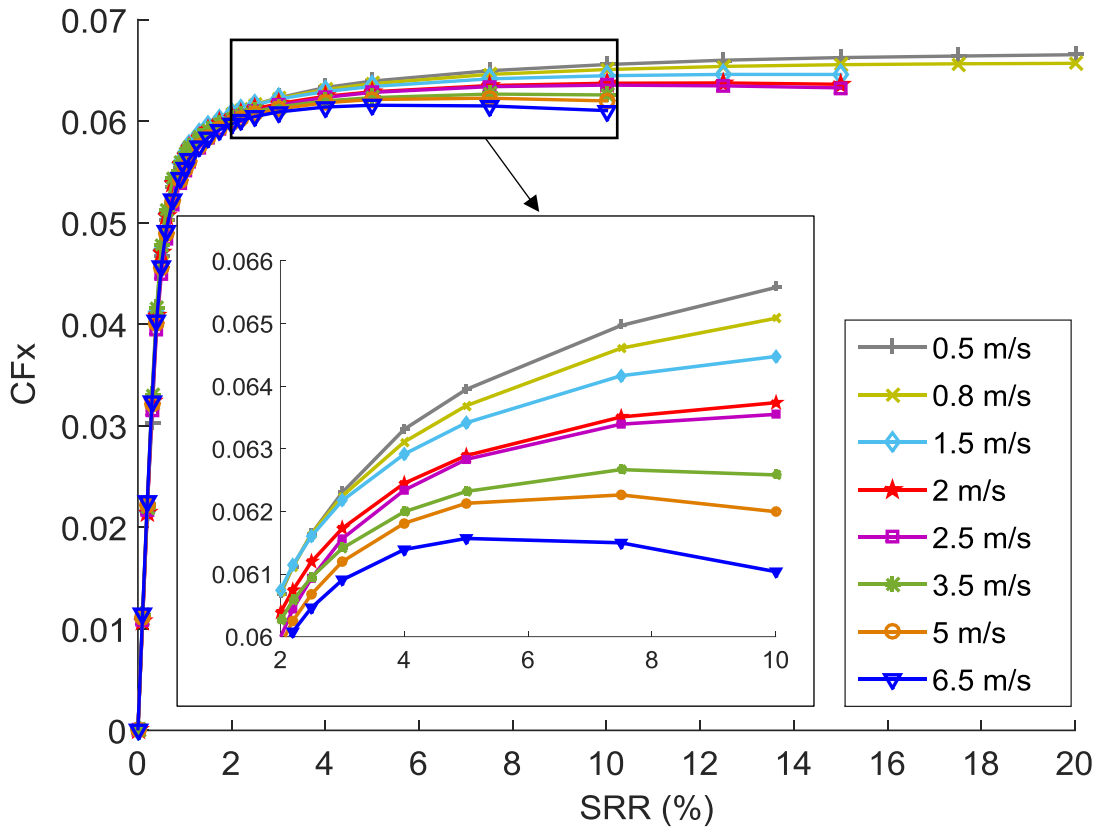

Figure 0-3 : Courbes de frottement du benzyl benzoate à différentes vitesses d'entraînement, à une pression de Hertz de 1.68 GPa et à 40°C.

Les valeurs de LSS dérivées des courbes de frottement obtenues à différentes vitesse d'entrainement U_e sont tracées Figure 0-4, tout en indiquant à partir de quelle valeur de U_e les régimes de lubrification en film complet et mixte ont lieu. Les résultats montrent clairement un très bon accord entre la prédiction du régime de lubrification par le rapport h_{min}/Σ et la mesure de LSS : les résultats suivent deux pentes différentes, en fonction du régime de lubrification. Dans le régime dit film complet, il existe une dépendance entre la valeur LSS et le cisaillement du lubrifiant ou la vitesse d'entraînement. Plus le lubrifiant est cisaillé, plus la valeur de LSS est faible. Comme l'auto-échauffement du lubrifiant induit une diminution de LSS, la mesure d'une LSS induite (uniquement) mécaniquement nécessiterait de minimiser cet échauffement et donc, idéalement, d'appliquer une vitesse d'entraînement nulle. Cependant, la baisse de U_e entraîne une réduction de l'épaisseur du film, jusqu'à atteindre un régime de lubrification mixte (partie gauche de la Figure 0-4). Sur le côté droit de la Figure 0-4, donc pour les vitesses plus élevés, la LSS continue de diminuer sous l'influence des effets thermiques. La baisse de LSS dans le régime EHD est cependant moins importante que dans le régime mixte.

Il est néanmoins nécessaire de définir des conditions expérimentales optimales afin de minimiser l'influence des effets thermiques, tout en veillant à rester dans le régime de

lubrification en film complet. Selon la Figure 0-4, une vitesse d'entraînement de 2.5 m/s est un choix adéquat pour pouvoir mesurer les valeurs de "LSS induite mécaniquement", dans des conditions isothermes nominales.

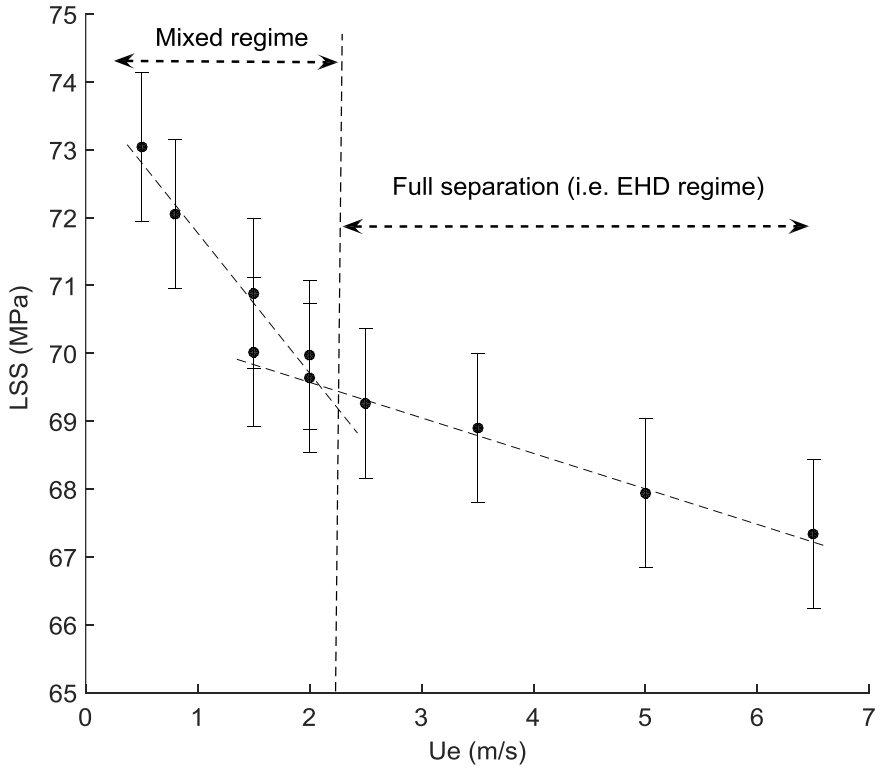

Figure 0-4 : variation de la LSS du benzyl benzoate avec la vitesse d'entraînement, à une pression de Hertz de 1.68 GPa et à de 40°C.

Validation avec un lubrifiant industriel

Comme démontré avec le benzyl benzoate, la vitesse d'entrainement est un paramètre déterminant pour réaliser des expériences dans des conditions isothermes nominales. Pour mettre en évidence l'influence des effets thermiques sur la LSS de l'huile minérale T9, nous avons appliqué le même protocole expérimental que celui défini pour le benzyl benzoate. En raison de sa viscosité élevée, U_e varie de 0.3 à 6.5 m/s. Les expériences ont également été réalisées avec une bille en acier et un disque en saphir à une pression Hertzienne constante de 1.70 GPa et à 40 °C. Les résultats expérimentaux sont résumés dans la Figure 0-5.

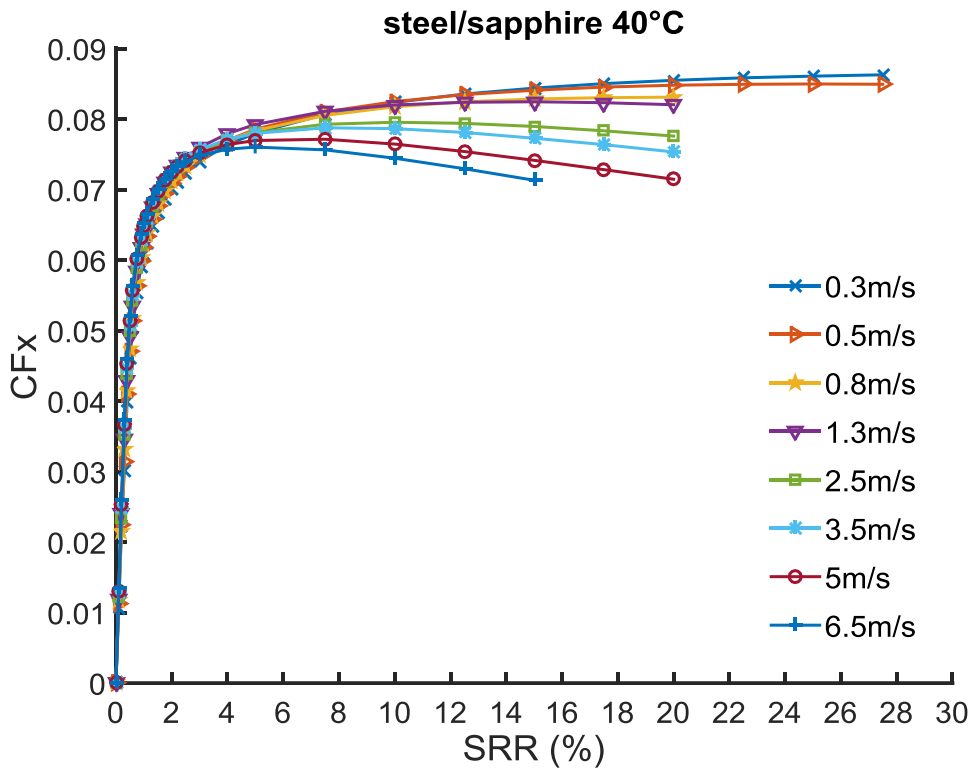

Figure 0-5 : courbes de frottement de la T9 à différentes vitesses d'entraînement, à une pression de Hertz de 1.70 GPa et à 40°C.

On peut observer que, quelle que soit U_e appliquée, toutes les courbes de friction se chevauchent complètement à très faible SRR. L'influence des effets thermiques et rhéologiques sur le coefficient de frottement devient de plus en plus importante lorsque la vitesse d'entrainement augmente. Comme dans le cas du benzyl benzoate, il existe une dépendance entre le U_e et la LSS. Dans la Figure 0-6, la LSS est tracée en fonction de U_e. Encore une fois, deux régions linéaires peuvent être observées : pour U_e <1m/s, la pente de LSS = f(U_e) est supérieure. En se basant sur le rapport h_{min}/Σ décrit précédemment, un régime mixte est prévu pour U_e inférieur à 1 m/s et un régime en film complet pour $U_e \geq 1$ m/s. On peut noter que la baisse de la valeur de LSS dans le régime EHD pour l'huile minérale T9 est plus importante que celle du benzyl benzoate. Ceci est dû au fait que la LSS est une propriété intrinsèque à chaque fluide.

Les deux lubrifiants décrits ci-dessus (benzyl benzoate et T9) ont été utilisés dans ce qui suit pour étudier la dépendance de la LSS avec la température et la pression. Nous présentons d'abord les résultats expérimentaux obtenus avec le benzyl benzoate, puis ceux obtenus avec le lubrifiant industriel T9.

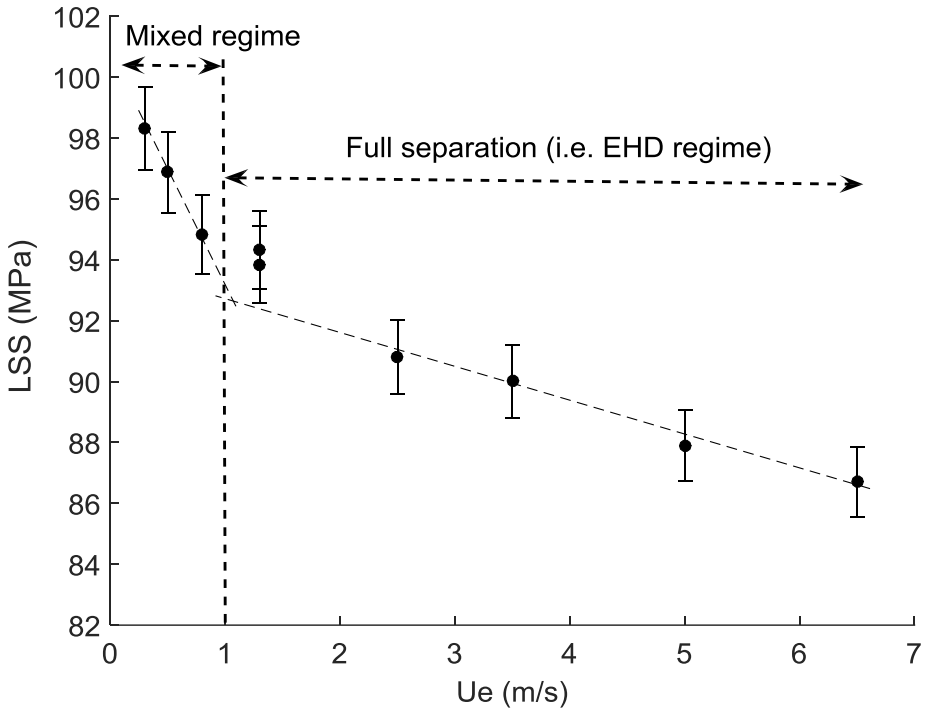

Figure 0-6 : Variation de la LSS de la T9 avec la vitesse d'entraînement à pression de Hertz constante de 1.70 GPa et à température de 40°C.

Mesures de frottement

Conditions opératoires

Les conditions opératoires sont définies afin d'effectuer des mesures de frottement dans des conditions isothermes nominales. Pour cette raison, le SRR appliqué pour le benzyl benzoate est limité à ± 10% afin d'éviter l'influence des effets thermiques sur la réponse du fluide. Pour toutes les conditions testées, φ_T, est supérieur à 0.96. U_e est adapté pour chaque température appliquée de manière à garder presque constante l'épaisseur du film de lubrifiant pour toutes les conditions opératoires. L'épaisseur centrale du lubrifiant (h_c) est déterminée avec le modèle de Hamrock et Dowson [38].

Pour varier la gamme de pression de contact, les trois configurations, acier/acier, acier/ saphir et WC/WC ont été testées. La pression maximale dans le contact P_{Hertz} est donnée par la théorie de Hertz :

$$P_{Hertz} = \frac{3F_Z}{2\pi a^2} \tag{0-6}$$

Les températures appliquées sont de 20, 40, 60 et 80 ° C. Les conditions expérimentales sont données à l'Annexe C, U_e appliqué varie de 1.3 m/s à 20 °C à 6.5 m/s à 80 °C afin de maintenir une épaisseur centrale de film quasi constante.

Les courbes de frottement obtenues présentent une tendance proche. Selon la température et la pression appliquées, trois régimes sont distingués selon la valeur de SRR :

• une région linéaire à très faible SRR, où le coefficient de frottement augmente linéairement avec SRR (réponse "visqueuse" ou linéaire),

• un comportement rhéofluidifiant à SRR intermédiaire, où le coefficient de frottement augmente plus lentement avec le SRR,

• un comportement semblable à un plateau (ou régime LSS) pour certaines courbes de frottement à SRR plus élevé.

Dans tous les cas, aucune diminution significative du coefficient de frottement, qui caractérise la prédominance des effets thermiques, n'est observée.

Dépendance de la contrainte limite de cisaillement avec la pression et la température

- Benzyl benzoate

Après avoir démontré qu'aucun effet thermique significatif n'est observé dans les mesures de frottement, la dépendance à la température et à la pression de la LSS est étudiée. Les valeurs de LSS dérivées des courbes de frottement du benzyl benzoate sont tracées dans la Figure 0-7 en fonction de pression moyenne ($\bar{P} = 2/3P_{Hertz}$) et de la température. Toutes les valeurs de LSS ont été calculées en utilisant l'équation (0-4).

Pour la clarté de la figure, les intervalles de confiance à 95% de ± 5.6% (c'est-à-dire deux fois l'écart-type relatif) sont tracés pour les températures de 20 et 80 ° C.

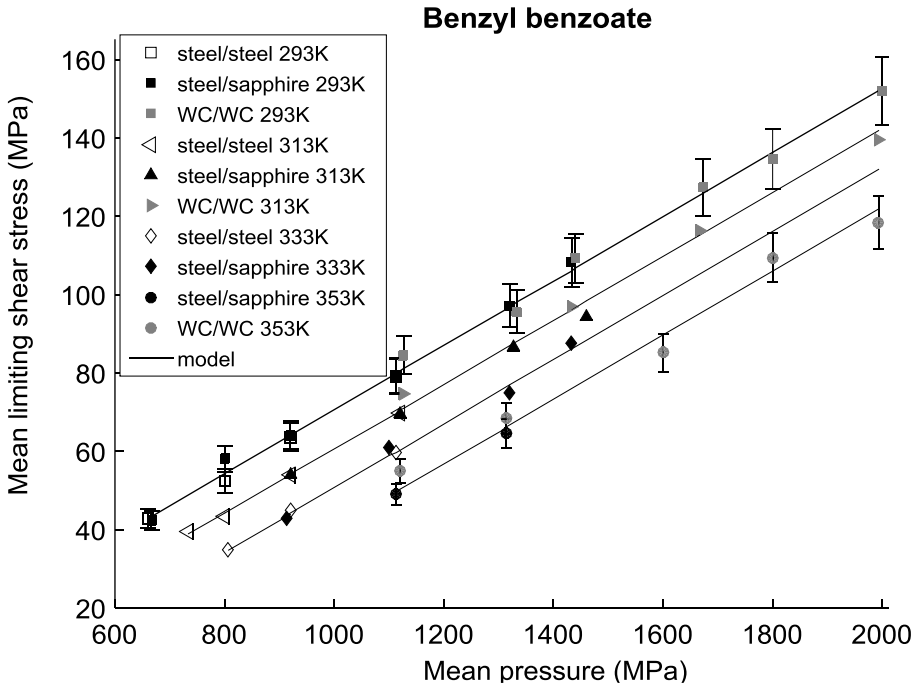

Figure 0-7 : Dépendance de la contrainte limite cisaillement avec la pression et la température du benzyl benzoate.

Tout d'abord, on observe un recouvrement entre les valeurs de LSS obtenues avec les différents matériaux des éprouvettes (acier, saphir et carbure de tungstène), ce qui signifie qu'il n'y a pas d'influence de la nature des matériaux de contact sur la LSS. La LSS dépend linéairement de la pression et de la température : elle augmente avec la pression et diminue avec l'augmentation de la température. Une régression optimale sur toutes valeurs de LSS a conduit aux relations suivantes:

$$\overline{\tau_L} = \gamma\overline{P} - \beta T \quad (0\text{-}7)$$

avec T en °C, et

$$\overline{\tau_L} = \gamma\overline{P} - \beta T + \tau_{L0} \quad (0\text{-}8)$$

avec T en K, et $\tau_{L0} = \beta \times 273.15$. L'équation (0-8) est retenue pour ce qui suit.

γ et β sont respectivement les coefficients de LSS-pression et LSS-température. Les valeurs des paramètres du modèle sont donnés dans le Tableau 0-3 : ils ont été obtenus avec un coefficient de corrélation $R^2 = 0.996$.

γ	β (MPa/K)	τ_{L0} (MPa)
0.082	0.5044	136.9

Tableau 0-3 : Paramètres du modèle dérivés des mesures de frottement du benzyl benzoate allant jusqu'à 3GPa et 80°C.

Ces coefficients sont constants quelles que soient les surfaces en contact (acier/acier, acier/saphir ou WC/WC), τ_{L0} est une constante égale à 136.9 MPa qui correspond à la LSS extrapolée à pression ambiante et à 0 K.

Contrairement aux modèles précédents de la littérature [29, 41], nos résultats expérimentaux ne montrent aucun couplage entre pression et température. Au mieux de nos connaissances, c'est la première fois qu'un tel modèle bilinéaire dérivé d'un grand ensemble de données expérimentales est obtenu. Généralement, les modèles de LSS trouvés dans la littérature proviennent de tests de frottement réalisés à des vitesses d'entrainement et de SRR élevées [29] avec $\phi_T \ll 0.96$ ce qui a du induire une élévation de température dans le film de lubrifiant. En se basant sur nos résultats expérimentaux, nous pensons que l'échauffement du lubrifiant pourrait être responsable du terme complémentaire de couplage dans les modèles LSS trouvés dans la littérature. L'avantage de l'équation (0-8) est que les influences de la pression et de la température apparaissent découplées, de sorte que les contributions mécaniques et thermiques sur la LSS sont séparées. Par conséquent, ce modèle pourrait permettre de décrire la variation de la LSS des lubrifiants si les résultats obtenus jusqu'à présent sont confirmés sur d'autres fluides. Dans la partie suivante, la dépendance de la LSS avec la température et la pression de l'huile minérale T9 est étudiée.

- T9

Le même traitement que pour le benzyl benzoate a été appliqué à l'huile T9. Les résultats sont résumés dans la Figure 0-8. La LSS est tracée en fonction de la pression moyenne pour chaque température appliquée. Des tendances similaires à celles du benzyl benzoate sont observées sur l'évolution de la LSS, avec un bon recouvrement des résultats des différents matériaux. De même, on trouve un modèle bilinéaire découplé : la LSS varie linéairement avec la pression et la température. Une régression linéaire sur toutes les valeurs avec un coefficient de corrélation $R^2 = 0.989$ a conduit à des valeurs de γ, β et τ_{L0} données dans le Tableau 0-4. On peut noter que ces coefficients sont supérieurs à ceux obtenus avec le benzyl benzoate, ce qui montre qu'ils dépendent de la nature et de la composition chimique du lubrifiant.

γ	β (MPa/K)	τ_{L0} (MPa)
0.101	0.622	174.9

Tableau 0-4 : Paramètres du modèle dérivés des mesures de frottement de la T9 jusqu'à 3 GPa.

Ce résultat obtenu dans une gamme de pression allant jusqu'à 3GPa confirme, pour un autre lubrifiant de nature différente que le benzyl benzoate, la variation linéaire de la LSS avec la pression et la température. De même, les matériaux en contact n'ont eu aucune influence sur la LSS.

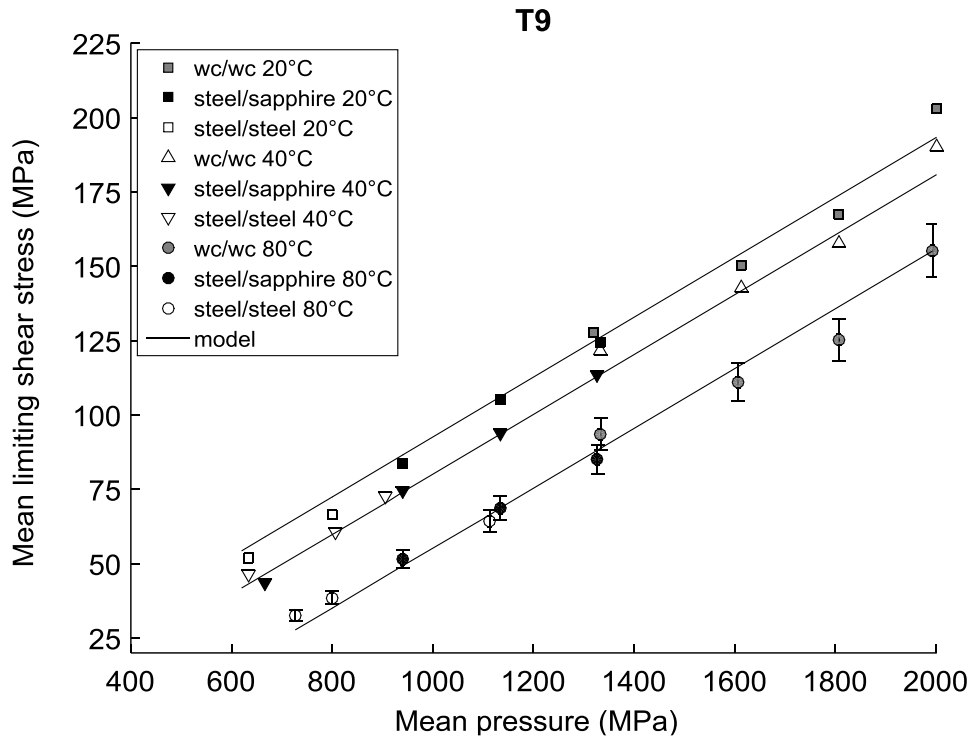

Figure 0-8 : Dépendance de la contrainte limite cisaillement avec la pression et la température de la T9.

Caractérisation de l'état microstructural du lubrifiant

Le comportement d'un lubrifiant soumis à des conditions extrêmes de cisaillement et de pression n'est pas bien compris. Mais, il est généralement admis que lorsque la vitesse de glissement est suffisamment petite pour éviter un échauffement du lubrifiant, une viscosité effective moyenne peut être déduite de la région linéaire de la courbe de frottement. Par ailleurs, les techniques in situ, adaptées à la problématique du contact EHD sont de plus en plus utilisé pour expliquer l'état de structure du lubrifiant. Ces techniques sont essentielles pour mieux comprendre les phénomènes physiques et chimiques qui contrôlent les propriétés macroscopiques du lubrifiant telles que la viscosité ou la densité.

Ce chapitre est divisé en deux sections, la première concerne le comportement macroscopique du lubrifiant dans un contact fortement chargé. La pression de transition vitreuse du lubrifiant (comportement solide du lubrifiant) est estimée à partir du modèle de viscosité WLF modifié et comparée aux propriétés effectives du lubrifiant déduites des mesures de frottement. La seconde partie concerne l'évolution de la microstructure du lubrifiant sous pression avec des mesures in situ, telles que la spectroscopie Raman et Brillouin.

Viscosité effective

Le modèle WLF[42] est utilisé pour calculer les pressions de transition vitreuse du benzyl benzoate et de la T9. Ceci permet d'avoir un ordre de grandeur des conditions de pression et de température à partir desquelles le lubrifiant subit une transition vers un comportement vitreux. Les P_g estimées pour chaque température sont résumées dans le Tableau 0-5 et le Tableau 0-6.

T(°C)	P_g (GPa)
20	0.80
40	0.98
60	1.17

Tableau 0-5 : Pressions de transition vitreuse du benzyl benzoate estimées avec le modèle de viscosité WLF.

T(°C)	P_g (GPa)
20	1.12
40	1.46
80	2.24

Tableau 0-6 : pressions de transition vitreuse de la T9 estimées avec le modèle de viscosité WLF.

Tout d'abord, nous avons étudié l'influence des matériaux en contact sur les propriétés effectives du lubrifiant en utilisant l'approche décrite par Bair [21]. Il en résulte que la déformation élastique des matériaux en contact peut être négligée dans nos mesures de frottement. Ensuite, la viscosité effective, caractéristique du comportement du lubrifiant dans le contact est calculée pour chaque pression et température appliquée à partir de la pente du régime linéaire. Les résultats obtenus avec le benzyl benzoate et la T9 sont résumés dans la Figure 0-9 et la Figure 0-10, respectivement. L'axe des ordonnées est en échelle logarithmique. Pour chaque température, nous avons rajouté la pression de transition vitreuse estimée en utilisant le modèle WLF modifié.

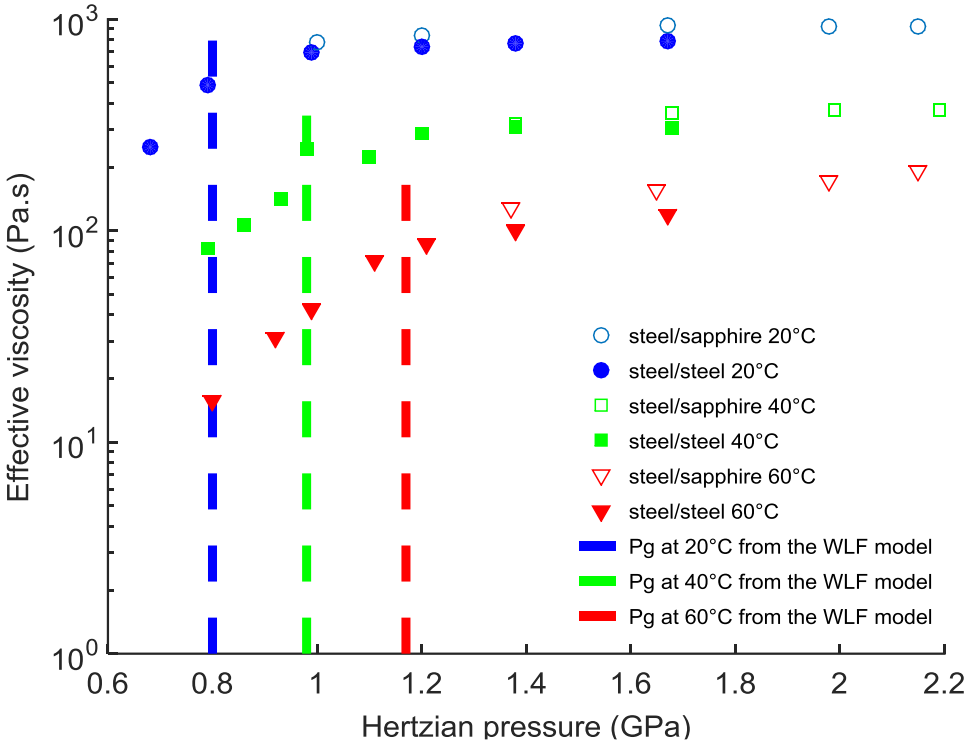

Figure 0-9 : Variation de la viscosité effective déduite de la région linéaire des courbes de frottement du benzyl benzoate avec la pression de Hertz.

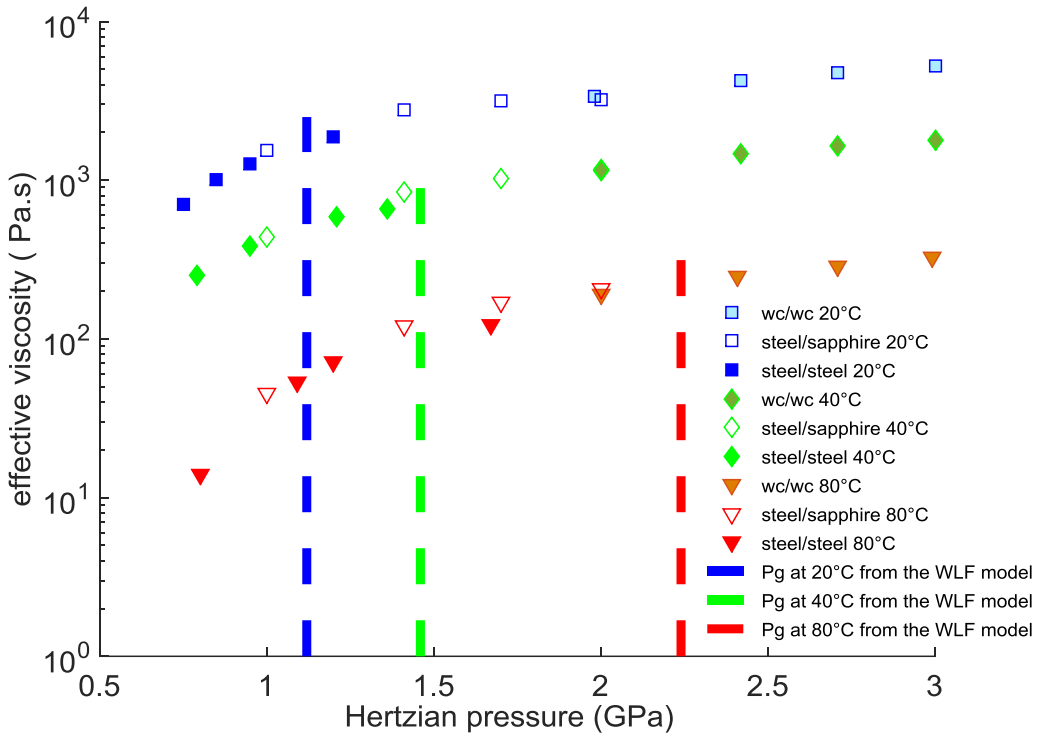

Figure 0-10 : Variation de la viscosité effective déduite de la région linéaire des courbes de frottement de la T9 avec la pression de Hertz.

Les deux figures présentent les mêmes tendances. Pour chaque température, deux régimes peuvent être observés : une variation exponentielle de la viscosité effective (correspondant à la partie linéaire sur la courbe) avec la pression jusqu'à une valeur critique de pression, à partir de laquelle la viscosité effective devient quasiment indépendante de la pression de Hertz. Cette pression critique semble correspondre à la pression de transition vitreuse du lubrifiant estimée avec le modèle WLF. Ceci pourrait s'expliquer par le fait que le lubrifiant reste dans un état liquide pour des $P_{Hertz} < P_g$ et que au-delà de cette pression critique le lubrifiant présente un comportement semblable à un solide vitreux. Ce résultat est en adéquation avec les résultats de Johnson et Cameron [43].

Cependant, les techniques spectroscopiques adaptées à l'étude de l'évolution de la structure du lubrifiant dans le contact EHD présentent un intérêt majeur car elles sont basées sur l'interaction lumière/matière. La section suivante démontre le potentiel de la spectroscopie Raman et Brillouin à l'étude des interactions moléculaires du benzyl benzoate, par l'analyse des fréquences vibratoires, des intensités des pics et les largeurs à mi-hauteur (FWHM). Le benzyl benzoate satisfait les diverses exigences des techniques Raman et Brillouin. La molécule possède deux cycles aromatiques, et un groupement ester.

Spectroscopie Raman

Le changement de phase du benzyl benzoate est étudié en condition statique (hors contact EHD) en utilisant la spectroscopie Raman couplée à une cellule haute pression. L'échantillon est confiné dans une cellule à enclume de diamant (DAC) pour appliquer une pression hydrostatique [44]. La cellule a été conçue pour travailler en "basse pression", les expériences couvrent une gamme allant jusqu'à 1.2 GPa. Un spectromètre U1000 Jobin-Yvon couplé à un microscope optique est utilisé avec un laser de type argon ionisé de longueur d'onde de 514.532 nm. Les mesures sont réalisées avec un objectif longue distance de travail X50. La pression à l'intérieur de la cellule est déterminée, avec une précision de 50 MPa, par le décalage du pic rubis R1 sous l'effet de la pression [45]. Un spectre Raman du benzyl benzoate à pression atmosphérique est représenté sur la Figure 0-11. La dépendance à la pression des pics les plus intenses, associés au mode de vibration de déformation -C = C- aromatique (1003 cm^{-1}) et d'élongation C = C (1601 cm^{-1}) et le troisième, moins intense, associé au groupe carbonyle -C = O, situé à 1715 cm^{-1} a été étudiée.

Pour les deux températures, 20 et 40 °C, nous avons calculé les rapports d'intensité entre les trois pics. Pour la température de 20 °C (Figure 0-12), la variation du rapport d'intensité entre le mode de déformation C = C et le mode C = O, semble montrer une rupture de pente autour de 0.5-0.6 GPa. Ceci est dû à un changement de propriétés du fluide et correspond à la transition de l'état liquide à un état vitreux du benzyl benzoate. Pour la température de 40 °C (Figure 0-13), les résultats semblent montrer une rupture de pente à 0.9 GPa entre le mode de déformation C = C et le mode d'élongation C = C.

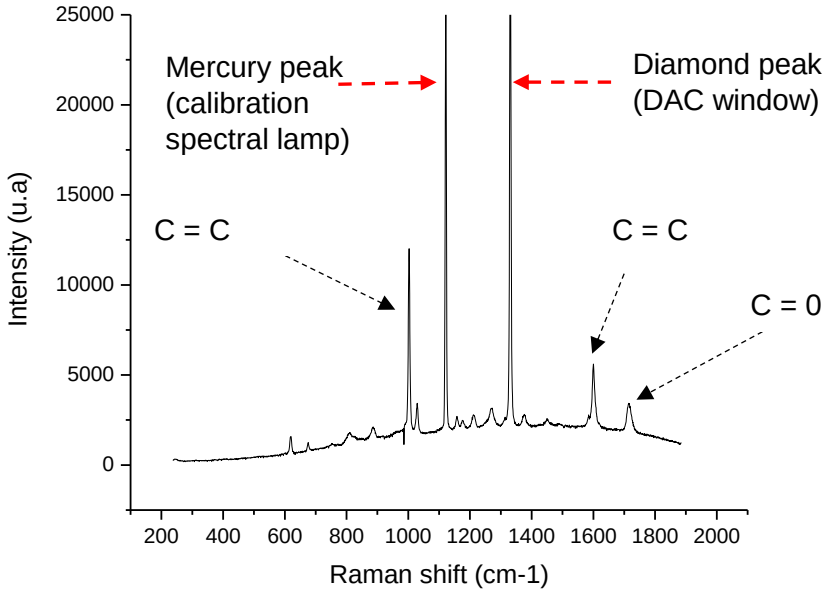

Figure 0-11 : Spectre Raman du benzyl benzoate à pression atmosphérique et à 20°C.

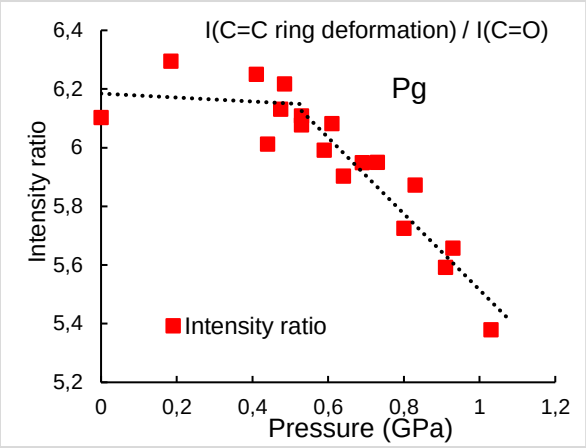

Figure 0-12 : Variation du rapport d'intensité avec la pression à 40°C.

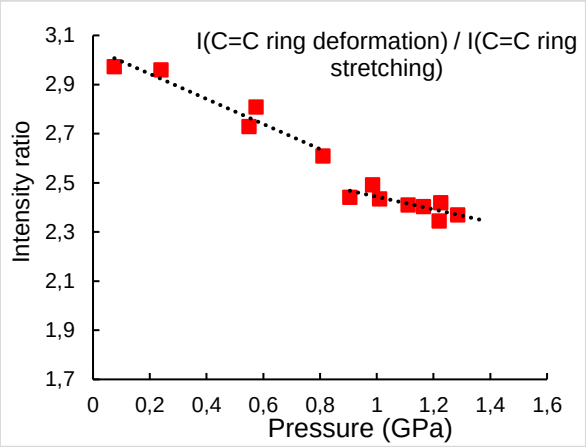

Figure 0-13 : Variation du rapport d'intensité avec la pression à 20°C.

Spectroscopie Brillouin

La spectroscopie Brillouin est aussi utilisée pour étudier les interactions locales se produisant dans un fluide sous l'effet de la pression. Des expériences ont été réalisées en collaboration avec Jérémie Margueritat, chercheur de l'Institut Lumière Matière (ILM) - UMR5306, à l'Université Claude Bernard Lyon1. Trois températures ont été étudiées : 20 °C, 40 °C et 60 °C. Les expériences ont été effectuées en utilisant une cavité Fabry Perot tandem Sandercock [46] couplé à un microscope. Un laser YAG / Nd^{3+} de longueur d'onde 532 nm a été utilisé pour sonder l'échantillon avec une puissance en sotie de microscope de 5 mW. La pression dans la cellule a été mesurée à partir de la fluorescence des particules de rubis. L'erreur sur la pression est estimée à ± 0.50 MPa. Un objectif x10 a été utilisé pour les expériences à 20 °C et 40 °C et x20 pour les expériences à 60 °C. Pour chaque température, les spectres Brillouin ont été mesurés pendant la phase de compression et de décompression. Il en résulte que les spectres de Brillouin sont complètement réversibles et reproductibles. De même que pour le Raman, une fonction gaussienne a été utilisée pour représenter les pics, donnant accès

à la fois à l'intensité du pic, à la fréquence de vibration et à la largeur à mi-hauteur (FWHM). Les résultats obtenus pour les différentes températures sont représentés sur la Figure 0-14 à Figure 0-16.

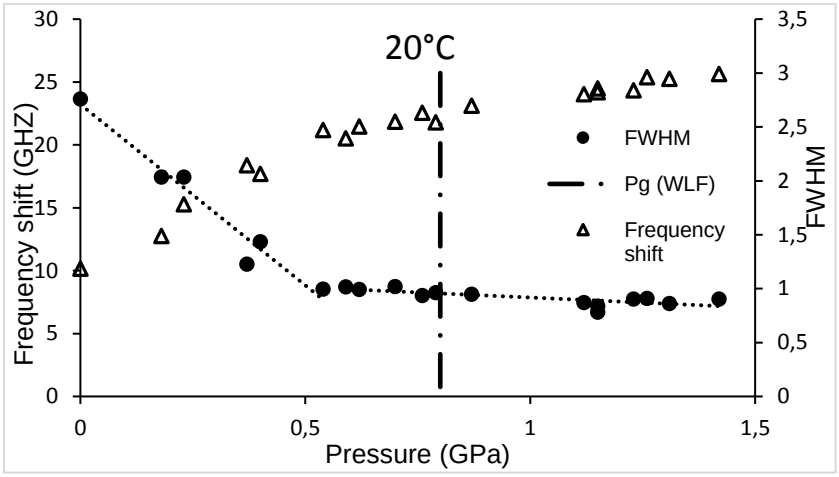

Figure 0-14 : Variation de la fréquence de vibration et de la largeur à mi-hauteur en fonction de la pression à 20°C.

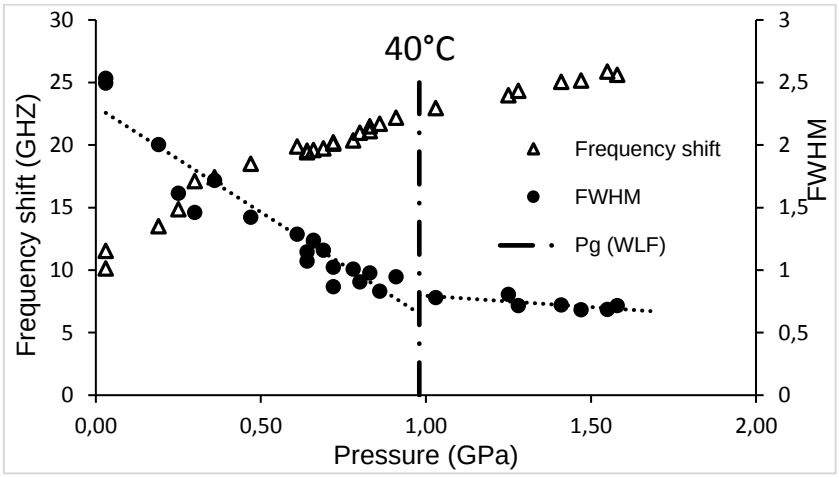

Figure 0-15 : Variation de la fréquence de vibration et de la largeur à mi-hauteur en fonction de la pression à 40°C.

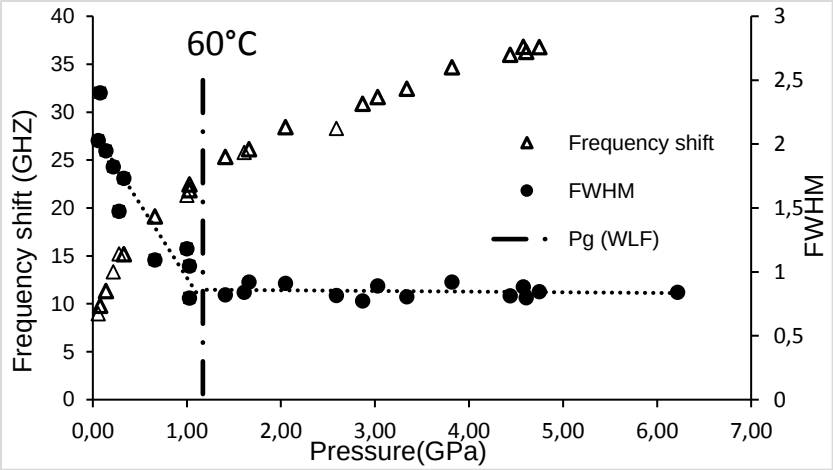

Figure 0-16 : Variation de la fréquence de vibration et de la largeur à mi-hauteur en fonction de la pression à 60°C.

Les trois figures montrent une augmentation de la fréquence avec la pression. En effet l'augmentation de la pression entraine la diminution de la mobilité des cycles aromatiques et, par conséquent, une augmentation de l'indice de réfraction. Le changement de phase du benzyl benzoate se traduit par un changement de pente dans la variation de la FWHM en fonction de la pression. Le premier régime est représentatif d'un comportement liquide, le second d'un comportement vitreux ou solide. La transition vitreuse du fluide se produit à des pressions de 0,5, 1 et 1,2 GPa à 20, 40 et 60 °C, respectivement. Ces pressions de transition sont du même ordre de grandeur que celles trouvées avec la spectroscopie Raman et sont plus proches de celles dérivées du modèle de viscosité WLF modifié, représentées par les droites verticales (*Figure 0-14* to *Figure 0-16*). On peut aussi remarquer que les pressions de transition à 20 ° C affichent la différence la plus marquée pour les trois méthodes utilisées.

Conclusion

Cette thèse a été consacrée à l'étude du frottement généré au sein des contacts lubrifiés fortement chargés. Une compréhension plus approfondie du comportement du lubrifiant dans ces conditions extrêmes de pression et de cisaillement est obligatoire pour améliorer la prédiction du frottement, dans les roulements à billes par exemple.

Tout d'abord, l'impact environnemental et le potentiel économique que représente la réduction du frottement dans les systèmes mécaniques a été présenté. Actuellement, des efforts considérables sont faits dans des secteurs tels que l'automobile et l'aéronautique afin de minimiser la consommation d'énergie due au frottement, non seulement pour des raisons économiques, mais aussi pour lutter contre le réchauffement climatique. La réduction du frottement implique une compréhension profonde des phénomènes qui se déroulent dans un contact lubrifié. Par conséquent, la principale motivation industrielle de ce travail était d'améliorer notre compréhension du frottement dans les contacts lubrifiés fortement chargés

comme ceux formés dans les roulements à billes lubrifiés par un film complet. Dans de tels contacts fortement chargés, le frottement présente un comportement plateau associé à la contrainte limite de cisaillement du lubrifiant au-delà d'une valeur critique de la vitesse de glissement.

Le premier chapitre était consacré à l'état de l'art des différents scénarios proposés dans la littérature pour expliquer l'origine physique de la contrainte limite et sa dépendance aux conditions opératoires. Des modèles rhéologiques incluant une contrainte limite obtenus soit avec une cellule haute pression, soit avec une machine bi-disque ou une bille impactante ont été présentés pour décrire le comportement du lubrifiant sous des conditions extrêmes de pression et de vitesse de cisaillement. Ensuite, les différents scénarios qui peuvent déclencher la LSS ont été examinés afin de mieux comprendre les différents phénomènes physiques qui pourraient entrer en jeu. Cependant, aucun des scénarios n'a été validé puisque la LSS n'a jamais été mesurée simultanément. Enfin, les différents modèles existants pour décrire la dépendance à la pression et à la température de la LSS ont également été présentés. Des modèles empiriques qui considèrent uniquement l'influence de la pression, ou de la pression et de la température, mais toujours à travers un terme de couplage entre ces deux paramètres, ont été proposés dans la littérature. Cependant il semble que le terme de couplage rencontré dans ces modèles pourrait être dû à l'échauffement du lubrifiant à l'entrée et dans le contact.

Le deuxième chapitre était consacré à l'étude de la dépendance à la pression et à la température de la LSS. Dans une première étape, une série d'expériences a été effectuée sur les deux lubrifiants, un diester pur (benzyl benzoate) et une huile minérale de turbine (Shell T9), avec des vitesses d'entraînement variables. Les résultats nous ont permis d'observer directement l'influence de l'échauffement du lubrifiant sur les valeurs de LSS. De plus, cette étape nous a conduits à définir les conditions expérimentales optimales qui limitent les effets thermiques tout en assurant un régime en film complet.
Ensuite, une série de mesures de frottement avec différents matériaux de contact, acier/acier, acier/saphir et WC/WC a été effectué dans des conditions isothermes nominales et à des pressions allant jusqu'à 3 GPa. Nous avons établi un nouveau modèle bilinéaire pour décrire la dépendance à la température et à la pression de la LSS du benzyl benzoate. Ce modèle bilinéaire a été ensuite validé sur l'huile minérale T9. C'est la première fois qu'un tel modèle qui découple les contributions mécaniques et thermiques sur la LSS a été présenté. Ces résultats contredisent les modèles rencontrés dans la littérature dans lesquels la pression et la température sont couplées.

Le troisième chapitre visait à améliorer notre compréhension du comportement microscopique des lubrifiants soumis à des conditions extrêmes de cisaillement et de pression. Nous avons

mis l'accent sur un possible changement de phase du lubrifiant, qui est une des hypothèses considérée comme étant responsable de l'apparition de la LSS. Une viscosité efficace a été déduite de la pente des courbes de frottement dans le régime linéaire. Son évolution avec la pression appliquée a été comparée à la pression de transition vitreuse P_g du lubrifiant estimée avec le modèle de viscosité WLF modifié. Pour les deux fluides étudiés, nous avons constaté que la viscosité effective augmente exponentiellement avec la pression pour $P_{Hertz} < P_g$ ce qui peut être associée à un comportement visqueux du lubrifiant. Ensuite, pour $P_{Hertz} > P_g$, la viscosité effective du lubrifiant reste quasiment constante, ce qui peut être associé à un comportement solide ou vitreux du lubrifiant.

En outre, nous avons étudié le changement de phase du benzyl benzoate sous pression avec des mesures telles que la spectroscopie Raman et Brillouin. Les deux techniques nous ont permis de déterminer une pression critique représentative d'un changement de comportement du fluide sous pression, que nous avons identifiée comme étant la pression de transition vitreuse. De plus, les pressions de transition vitreuse obtenues avec ces deux techniques à 40 et 60°C ont montré un bon accord entre elles, et aussi avec celles estimées à partir du modèle WLF.

I General introduction and objectives

Friction is a common dissipation mechanism encountered in everyday life, such as during rubbing both hands together, brushing teeth etc. It has both positive and negative effects: for instance, man would not be able to walk without friction and, the handling of a car directly depends on the friction between the tires and the road. Generally, friction generated by the relative motion of the contacting surfaces is expressed as a coefficient which can take into account several factors, such as the elastic deformation of the solids, the roughness/smoothness of the contacting surfaces, the pressure, the adhesion of the surfaces etc. The earliest studies on friction were carried out by Leonardo de Vinci (1452-1519): he measured the minimum force required for sliding a mass across a surface. Years later, other studies on friction were done by Amontons [1] and Coulomb [2]. From their experiments, three laws of friction were proposed:

-the friction force is directly proportional to the applied normal load,

-the friction force is independent of the sliding surface area,

-and the friction force is independent of the relative sliding velocity of the surfaces.

Friction leads to a higher energy consumption of a mechanical system. The scientific basis for the modern understanding of friction, lubrication, and wear were successively established by Hertz [3], Reynolds [4], and Bowden and Tabor [5], among others. From an energy point of view, reducing friction helps to improve the efficiency in mechanical systems (combustion engine, turbine, compressor etc.).

One way to reduce friction in contacts is lubrication. The lubricant can be liquid, gaseous or even solid. There is a high interest in producing lubricants which give low friction in order to minimize energy losses in transmissions and other lubricated systems. In addition to reduce friction and wear, lubricating oils are also required to carry out a range of other functions, such as corrosion prevention, providing a liquid seal at moving contacts and removal of heat and wear particles [6, 7]. The efficiency of a lubricating oil in reducing friction and wear is significantly depends on its viscosity. For car engine oils, the difference in fuel consumption between an optimised low friction oil and a standard oil can be as high as 5% [8].

Recently, Holmberg et al. [9] showed that nearly one-third of the fuel's energy is spent to overcome friction in passenger cars. The direct frictional losses, with braking friction excluded, represent 28% of the fuel energy. In total, 21.5% of the fuel energy is used to move the car. Energy losses due to friction in cars could be reduced by 18% within the next 5 to 10 years, which would result in global fuel savings of 117,000 million litres annually, and by 61% within the next 15 to 25 years, and would finally lead to fuel savings of 385,000 million litres annually [10]. In consequence, fuel efficiency improvement in passenger cars would reduce CO_2 emission by 290 million and 960 million tons per year, respectively. Today, significant effort is being devoted to reduce energy losses, not only for economic reasons, but also to fight against global warming. The European Union aims at limiting carbon dioxide emission in cars to less

than 95 $gCO_2.km^{-1}$ in 2020 [11]. Friction, wear reduction and lubricant stability are the most important parameters to be considered in assessing the environmental impact of lubricants.

I.1 Industrial motivations and scientific challenges

Technological advances in lubrication domain and environmental questions have led bearings manufacturers to provide high-performance bearings in the market. The global rolling element bearings market was valued at USD 81.6 billion in 2015 and is expected to grow significantly (*Figure I-1*), owing to the increasing heavy machinery manufacturing.

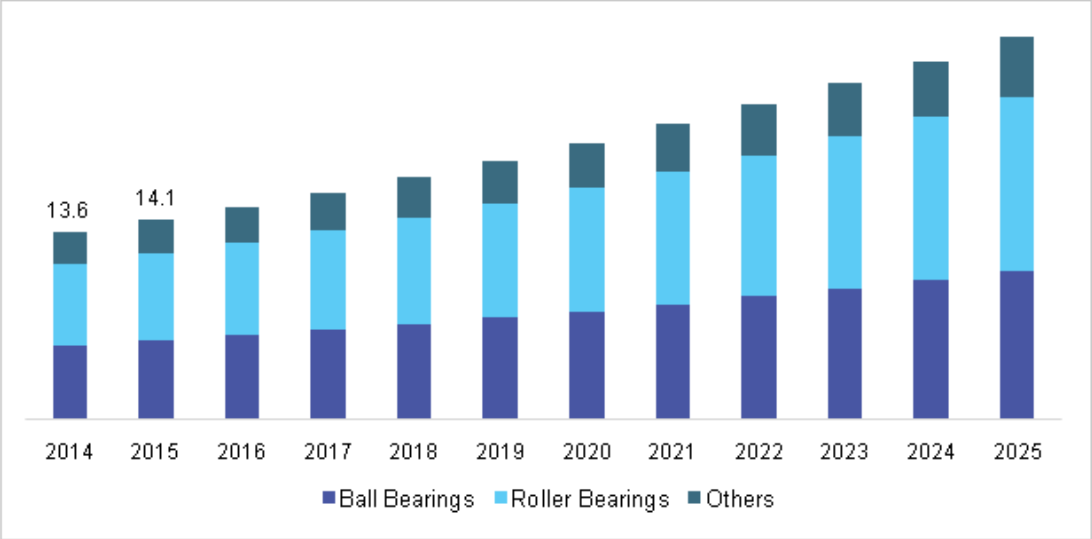

Figure I-1: U.S. rolling element bearings market by product, 2014-2025 (USD Billion) (http://www.grandviewresearch.com/industry-analysis/bearings-market).

Nowadays one of the technical challenges the bearings manufacturers are facing is how to minimize energy consumption due to friction as the mechanisms are increasingly heavily loaded. The reduction of energy losses inside bearings may improve their efficiency and allow a decrease of their operating costs. The energy saving potential is considerable because rolling element bearings are widely used in many applications. In addition, manufacturing high quality bearings will allow to reduce the pollution impact of air pollution by the decrease of CO_2 emissions in the surrounding air.

However, bearings manufacturers need to be able to estimate accurately the friction losses in order to optimize bearings design. In fact, rolling bearings operates in the elastohydrodynamic lubrication (EHL) regime.

Much effort has been made to provide the highest quality products and services for a wide range of applications. But up to now, increasing rolling element bearings life, performance and maintenance periods remains a difficult challenge for bearings manufacturers. When designing a rolling element bearing, every decision affects the performance and reliability. Friction is one

of the main performance indicators for a rolling element bearing, and it is mainly governed by the lubrication mechanisms. A thin lubricant film must be present to reduce friction in bearings. Friction reduction implies a deep understanding of the multi-physical phenomena that take place in a lubricated contact.
The main aim of this work is thus to improve friction prediction in lubricated contacts as those formed in rolling element bearings under full film conditions. This will contribute to optimize bearings life and performance, which is the industrial motivation of this study.

I.2 Outline

The pressure generated in elastohydrodynamic (EHD) contacts is high enough to induce a significant elastic deformation of the contacting bodies. The friction coefficient depends among other parameters on the relative sliding velocity (given by the slide-to-roll-ratio, SRR) between the two solid bodies. Experimentally, in the range of moderate contact pressures and relatively small SRR values, the friction coefficient increases with SRR. However, for high contact pressures, the friction coefficient displays a plateau-like behavior, which is representative of what is called the Limiting Shear Stress (LSS). Several scenarios are proposed in literature to explain its physical origins: however, LSS has never been simultaneously measured to validate any of them. Up to now, its physical origins are still a matter of debate. Therefore, it is important to understand the phenomena responsible for the LSS in order to predict accurately friction in highly loaded contacts. This remains an important scientific challenge because everything is not currently fully understood about the mechanisms at the origin of friction.
This work is dedicated to the investigation of friction occurring in highly loaded circular contacts formed between a ball and disc. A deeper understanding of these contacts characteristics and behavior is mandatory for an improvement of friction prediction in rolling element bearings. Experiments have been performed on two lubricants: an organic compound, benzyl benzoate, and a commercial turbine mineral oil, T9.

This manuscript is organized in three chapters: the first one is devoted to an overview of the different scenarios of LSS proposed to explain its physical origin. Some rheological equations found in literature to describe the lubricant behavior under extreme conditions of pressure, temperature and shear rate are presented. Then the different existing models to describe the pressure and temperature dependence of LSS are reviewed

The second chapter is divided into two sections: the first one concerns the influence of the lubricant viscous heating on the frictional response. This part aims to design optimal experimental conditions to avoid thermal heating during friction measurements. The second one is dedicated to the evaluation of the relationship between pressure, temperature and LSS.

In the third chapter the lubricant behavior under high pressure is investigated. In this part, we focus on the linear friction regime, at very low SRR (≈ 0.3%) for which an effective viscosity was deduced. Raman and Brillouin spectroscopy are also performed to study the lubricant phase change under static pressure. This chapter aims at understanding the microscopic behavior and the molecular interactions of lubricant under highly loaded contact.
Finally, a general conclusion is drawn from the different results presented and discussed in this work, and recommendations for future works are proposed.

I.3 State of the art on the limiting shear stress

This section aims to provide an overview of the LSS. It is divided into three main parts.
-The first one provides an overview of the different rheological equations including LSS proposed in literature to describe the lubricant behavior in EHL.
-The second one details the different scenarios proposed in literature to explain the physical origin of the LSS.
-The final part gives an overview of the different existing models of LSS which describe the pressure and temperature dependence of LSS.

I.3.1 Friction in EHL

EHL is a lubrication regime in which the normal load is concentrated over a very small area. The high pressures generated in the contact, typically between 1 and 3 GPa, induce two main effects: an elastic deformation of the contacting surfaces and a large increase of the lubricant viscosity [47]. The combination of these two effects with the imposed entrainment velocity leads to the formation of a thin lubricant film with thicknesses below a few hundreds of nanometers. In practice, this regime is typical of non-conformal contact encountered in several mechanical systems such as gears, rolling element bearings, cam-tappet systems, etc…
Pioneering research on EHD focused on the prediction of the lubricant film thickness. The main purpose was to obtain a sufficient thickness to ensure a full separation between the solids to prevent the failure of the mechanical components. The prediction of the lubricant film thickness in EHL contact was achieved in the 1950s [48, 49], based on rather strong assumptions such as a Newtonian behaviour of the lubricant [50], isothermal condition within the contact, and a pressure viscosity dependence described by the Barus equation [51].
In the 1960s, two techniques have been widely used to investigate EHL films, such as capacitance measurement [52, 53] and optical interferometry [54, 55]. The predicted shape of the lubricant film has been confirmed experimentally by Crook [52]. He observed the lubricant film shape by using a four-disc arrangement in which a chromium capacitance electrode was deposited on a central glass disc.

Unfortunately when it comes to friction, the EHL theory fails to predict the experiments especially in the case of highly loaded contacts. Friction is overestimated when considering a Newtonian behaviour of the lubricant.

The difficulty to predict friction in EHL is mainly due to the lack of understanding of the lubricant behavior in the Hertzian region, where the lubricant properties can vary drastically with pressure [56]. Indeed, in the EHL regime, friction in lubricated contacts is mainly caused by the shearing of the lubricant film in the highly pressurized contact area. The rheological behaviour of lubricants under conditions of high pressure, high shear and during short duration is still not well known.

Over the last decades, friction tests have been performed in order to better understand the friction mechanisms in highly loaded contacts. Macroscopically, the friction coefficient is defined as the ratio between tangential (or friction) force, F_X and the applied normal force, F_Z

$$CF_X = \frac{F_X}{F_Z} \tag{I-9}$$

The pioneering experimental work on friction in EHL has been done by Crook [57], by using a two-disc machine, as shown on *Figure I-2*. A series of friction tests have been made in order to make a comparison with the results from the EHL theory. The numerical simulations by Cheng [36] which were based on thermal analysis showed large discrepancies at low sliding with Crook experimental results (Figure I-3). For low sliding velocities, Tennapel et al. [58] provided an analysis based on the Newtonian behavior and the Roelands pressure-viscosity relation to calculate friction coefficients. Their values showed an acceptable agreement with Crook's experimental results. Another thermal solution was proposed by Cameron [59] which used the Slotte's equation to describe more accurately the temperature dependence of the viscosity.

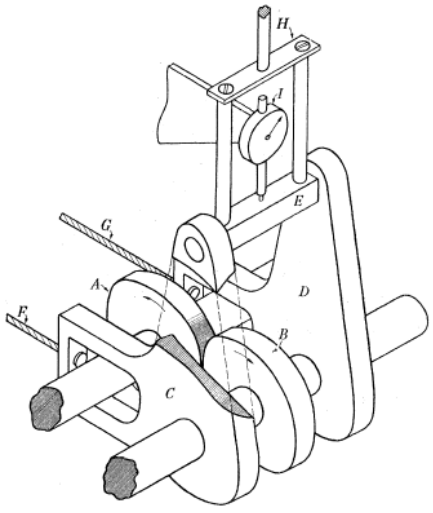

Figure I-2: The two disc machine arranged for the measurement of friction from Crook [57]. *A and B discs; C and D swinging arms; E axle; F and G loading cables. H spring beam; I di*

al gauge.

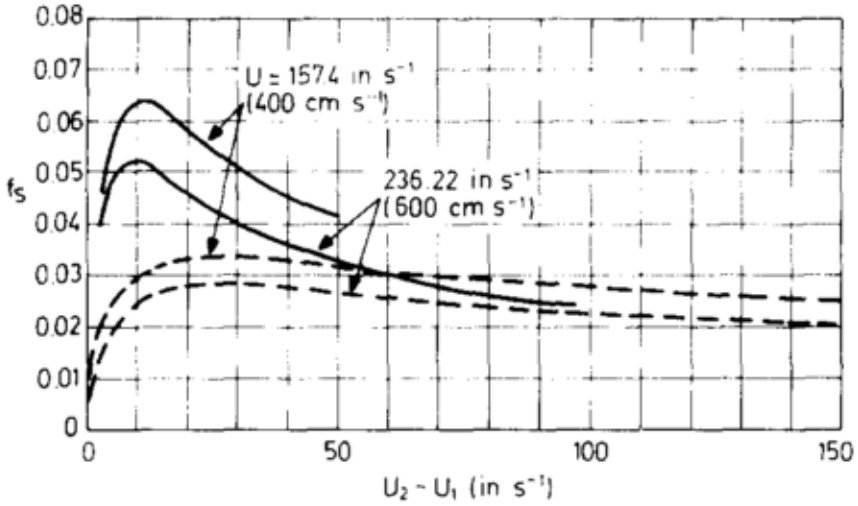

Figure I-3: *Comparison between experimental and theoretical values of friction coefficient: the dashed lines represents Cheng theory* [36] *and the solid lines, Crook experiments* [57].

Despite some divergences between his results and EHL theory, the experimental results of Crook [57] showed that, at least, 3 regions can be identified depending on the value of the sliding velocity, as shown on Figure I-4.

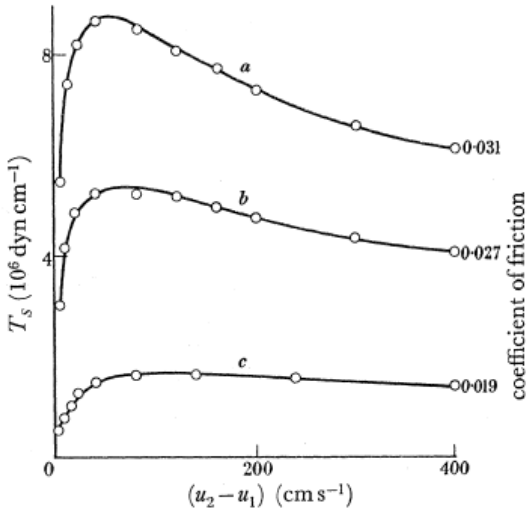

Figure I-4: Friction as function of sliding speed; (rolling speed at 400 cm^{-1}). Load (10^7 dyn cm^{-1}): (a) 20, (b) 15, (c) 7.5 from [57].

- Region I: a linear regime at very low sliding velocity in which friction increases almost linearly with the sliding velocity.
- Region II: a shear thinning regime in which friction increases slowly with the sliding velocity, followed by a plateau, where friction becomes independent of the sliding velocity. The fact that

the friction coefficient exhibits a plateau-like behavior led Smith [60] to propose, for the first time, a limiting shear stress for the lubricant. He suggested that the maximum in friction coefficient occurs because the oil film shears like a plastic solid when a critical shear stress is reached. Later he also suggested that the velocity difference between the sliding surfaces would be accommodated in a thin shear plane of molecular proportions within the lubricant, with layers of solidified lubricant moving with the velocities of the bounding solids on each of the shear plane [61].

- Region III: a decrease of the friction coefficient at medium-high sliding velocity due to the viscous heating of the lubricant submitted to high pressure and high shear rate.

Different explanations of the friction curve in terms of rheological properties of the lubricant have been made by several authors [28, 62]. Dyson [62] supported the argument that the friction curve can be divided into three regions (Figure I-5) as previously described: the isothermal region which corresponds to a linear friction variation, the non-Newtonian region corresponding to a non-linear friction variation and finally the thermal region. In the isothermal region, the slope at the origin defines an effective viscosity. On the other hand, at high shear rates, according to Plint [22], the friction plateau is reached if the lubricant behaves like a plastic solid. This plateau anyway represents an essential lubricant property as it determines the maximum of friction that can be transmitted in an EHD contact. It would thus be the main property to evaluate when synthesizing or selecting a lubricant according to Bair et al. [63].

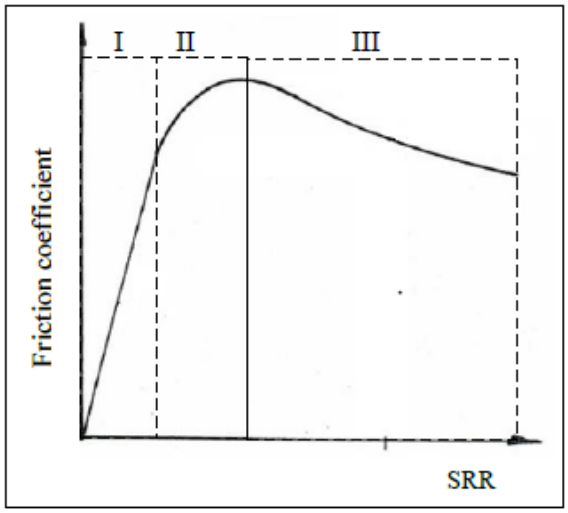

Figure I-5: Friction regimes according to Dyson [62].

Early after the publication of the experimental results by Crook [57], many phenomenological approaches of the LSS have been proposed in the literature in order to describe the lubricant behavior at high pressure and high shear rate.

I.3.2 Phenomenological approach of the limiting shear stress

In recent years, much interest has been expressed in the rheological characteristics of lubricants under the conditions of high pressure and high shear rate encountered in lubricated machine elements operated in the EHD regime. Much attention has been paid to model the lubricant rheology over a wide range of EHD conditions. More accurate rheological equations have been proposed to describe lubricants under fast and large pressure variations, short transit times and high shear rates. Unfortunately, up to now, no rheometric device allows to reach the very severe conditions of pressure, shear stress and shear rate that arise in the Hertzian region of an EHD contact. However, much efforts have been made in developing realistic (but still empirical) relationships between shear stress and shear rate. According to the literature, two main experimental devices enable to access the properties of lubricants at high pressure: the twin-disc machine, which has been widely used over the years, and high-pressure devices as those developed by Bair [63].

I.3.2.1 Disc machine

Disc machine was used to investigate the so-called visco-elastic properties of lubricants [57] [60]. The lubricant is sheared between two rollers whose velocities can be controlled independently of each other. Then the rheological parameters of the lubricant are deduced from the friction force and the estimation of the film thickness. The shear rate is estimated by assuming a linear velocity profile across the lubricant film, which is a rather strong assumption. The relation between shear stress and shear rate for EHD oil film has been investigated by Hirst and Moore [64], using a two-disc machine. They found that at low SRR values the shear rate is directly proportional to the shear stress, but at higher values the shear stress increases more rapidly than the rate. Their results showed that the limit of the linear region is determined by the value of the shear stress, not the shear rate and the critical shear stress depends on both the molecules size and the applied pressure. According to Johnson and Tevaarwek results [28], the lubricant behaves as a viscoelastic material and follows a Maxwell-Ree-Eyring non-linear viscoelastic rheological law (I-10). This equation covers a large range of isothermal behaviors: linear and nonlinear viscous, linear and nonlinear viscoelastic and elastic/plastic behavior. At given temperature and pressure, three lubricant properties need to be adjusted on experimental results: the zero shear-rate- viscosity, μ_0, the elastic shear modulus, G, and a reference shear stress, τ_0, which corresponds to the critical shear stress at which the fluid becomes nonlinear. Johnson et al. [28] found that the variations of these parameters with pressure and temperature derived from their experiments showed a good agreement with the Eyring theory of fluid flow.

$$\dot{\gamma} = \frac{\dot{\tau}}{G} + \frac{\tau_0}{\mu_0} sinh\left(\frac{\tau}{\tau_0}\right) \qquad \text{(I-10)}$$

Evidence is provided that the apparent sinh law behavior of EHD friction is really a consequence of the distribution of the limiting stress boundary in the contact region [65]. Hirst and Moore [64] and Johnson and Tevaarwerk [28] both proposed models based upon the Eyring theory of viscosity to represent the friction behavior of lubricants in EHD contacts. For Evans and Johnson [19], the lubricant behaviour changes from sinh-law to LSS at high pressure or high shear rate. The Eyring model has been widely used in literature to describe the rheological behaviour of lubricants, but it fails to predict the LSS regime. The friction prediction made by Brandao and al.[66], which was based on an elasto-viscoplastic model including analytical thermal effects and the LSS concept showed a good agreement with their experimental results for different lubricants. However, the rheological models arisen from disc machine exhibit significant limitations. Therefore, other models based on more conventional rheological methods, as for instance based on high pressure rheometers are proposed in the literature.

I.3.2.2 High pressure rheometer

Bair and Winer [63] were the first to measure the LSS of liquid lubricants outside an EHD contact by using a high pressure rheometer. Their experimental results are typically restrained to low shear rate. The shear rheological response of a naphthenic mineral oil (N1), a polyphenyl ether (5P4E) and a synthetic cycloaliphatic hydrocarbon (Santotrac 50) has been measured up to 1.2 GPa by Bair et al. [63], using three different pressures cells. Their results highlighted the evidence of LSS for the three lubricants in the viscous, elastic and plastic regions.

According to Bair and Winer results, the rheological properties of lubricants under EHD conditions can be described by a modified Maxwell model. Their model, as shown in equation (I-11) requires three material properties: the LSS, τ_L, the low shear viscosity, μ_0, and the limiting elastic shear modulus G_∞. These parameters depends on pressure and temperature. The low shear rate viscosity can be described by a free volume equation [42]. It has been shown that the lubricant viscosity varies exponentially with pressure until 1.0 GPa. In addition, there is a critical value of pressure above which the lubricant viscosity increases drastically with pressure.

$$\dot{\gamma} = \frac{1}{G_\infty}\frac{d\tau}{dt} - \frac{\tau_L}{\eta_0} ln\left(1 - \frac{\tau}{\tau_L}\right) \qquad \text{(I-11)}$$

The experimental results of Bair and Winer [65] showed that the lubricant exhibits a shear thinning behavior at high shear stress and provided evidence of the LSS. This confirms the analysis made by Evans and Johnson [19]. Nevertheless, the high pressure rheometer has limitations. It does not allow to reach high shear stresses and high shear rates. For pressures higher than 1 GPa, there is no alternative to the twin-disc machine friction test. Jacobson [32]

constructed a new type of rheometer to measure the high pressure rheology of lubricants under transient pressure and shear stress. The main part of the apparatus is a spherical steel ball which can roll along two inclined guides and two parallel flat surfaces. In this device, the steel ball hits a lubricated flat surface with an angle determined by the inclination of the guides. The compression time for the lubricant is of the same order as in EHD contacts, and the pressure can be as high as 5.5 GPa. He demonstrated that measuring the limiting shear stress pressure coefficient, γ ($\gamma = \frac{\partial \tau_L}{\partial p}$) of lubricant makes possible to calculate the coefficient of friction for EHL.

Large progress have been made in EHL numerical modelling by incorporating different rheological models, like Jacobson [67] and Bair [63] models. However, there is still no general model allowing to describe the lubricant behavior over the whole range of operating conditions found in the in EHL regime.

Significant progress have also been made in experimental research in EHD contacts, but some important questions have still not been resolved. One of the most contentious issues is how to explain the physical origin of the LSS and how LSS is influenced by pressure and temperature.

I.4 Scenarios of LSS

This section reports the physical mechanisms which may be responsible for the LSS, pointed out through a literature survey.

I.4.1 Wall slip

In fluid mechanics, the no-slip boundary condition is applied to all liquid-solid interfaces. The no-slip boundary condition has been largely used for the design of hydrodynamic bearings, gears etc. Recently the validity of this assumption has becoming questionable. Indeed, under certain operating conditions, evidence of boundary slip has been demonstrated experimentally [12, 13] and validated by molecular dynamic simulations [14]. Schnell experimentally showed that wall slip occurs for water flowing over a hydrophobic surface [15]. Wall slip has been observed for simple fluids (such as hexadecane) and also for complex fluids (such as polymers) [16]. Hervet et al. [16] showed that noticeable slip at the wall can occur in the case of a smooth surface even in total wetting conditions. Recent experimental results showed that wall slip can be observed on both hydrophobic or hydrophilic surfaces [68]. Boundary slip may happen at the interface, if the critical shear stress of the liquid/solid interface is smaller than the LSS of the lubricant [17]. Wall slip may occur either within the lubricant film or at the solid/liquid interface [69].

Others authors used different experimental techniques to describe the boundary slip as the fluorescence recovery after photobleaching [18], the surface force apparatus [70], and the atomic force microscopy [12]. According to Li et al. [17], the slip length varies non-linearly with

the shear rate, and increases exponentially with pressure. Wong et al. [71] carried out experiments with an optical EHL test-rig. By varying either the ball or the disk velocity, they realized a series of interferograms on impact dimples captured in real time by a CCD detector during the first 4s of each test. A series of interferograms of the impact dimples obtained with a polybutene oil (PB1300) under several conditions is shown in Figure I-6. The black and red arrows on the right illustrate the direction and relative magnitude of the velocity of the specimen. The results, based on the motion of the dimples, showed that apparently the displacement of the dimple depends only on the motion of the SiO_2-coated glass disc surface, not on the ball motion. In addition, varying the ball velocity for a constant disc velocity (Figure I-7), they found that the velocity of the dimple was constant and roughly equal to the disk velocity for ball speeds up to 75 µm/s. Beyond this value, the dimple velocity increases with the ball velocity. Wong et al [71] concluded that there was some boundary slippage at the lubricant/steel interface and also at the lubricant/disk interface. Furthermore the tests carried out on 5P4E under a maximum pressure of 1.33 GPa at room temperature showed that there was no displacement of the dimple. According to Wong et al, this result is not surprising, very likely because the lubricant is in glassy state, referring to [72, 73].

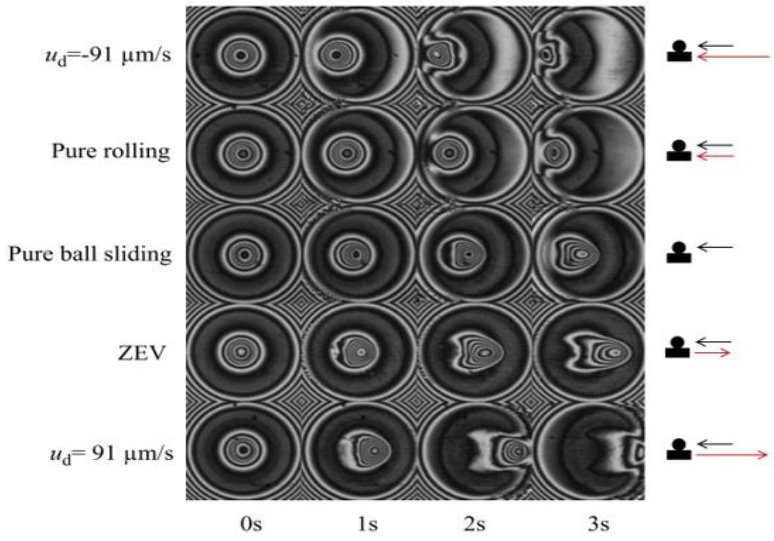

Figure I-6: Motion of dimples at different times and under various disc velocities for a constant ball velocity from Wong et al.[71].

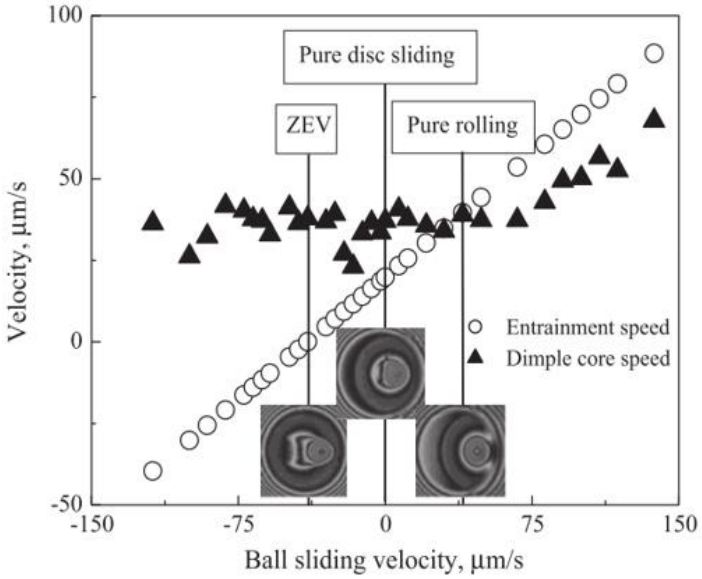

Figure I-7: Dimple velocity under various ball velocities for a constant disc velocity (PB1300 steel/SiO_2, ud=+39.6µm/s, 20N) from Wong et al.[71].

By measuring directly the lubricant film thickness in EHD contacts under several operating conditions, Kaneta et al [74] found that the lubricant film exhibits a solid-like behavior in the pure rolling case. If the lubricant film is very thin, the fluid slips at or near the contacting surfaces. The slip velocity is approximately one-half of the surface velocity. The slip length is expected to be of the same order of magnitude as the molecular size [16]. This observation is also supported by the molecular dynamic simulations made by Thompson et al. [14]. Hervet and Léger [16] showed that for simple fluids, noticeable slip at the wall can occur in the case of a smooth surface even in total wetting conditions.

By using total internal reflection-fluorescence recovery after photobleaching (TIR-FRAP) technique, Pit [18] directly showed the evidence of wall slip for hexadecane. The fluid was sheared between two parallel sapphire discs, as shown in Figure I-8. Fluorescent probes, with similar size to the hexadecane molecules, were used as flow tracers and illuminated by an intense laser beam. Based on the fluorescence intensity of the tracers, Pit demonstrated that wall slip occurs at the hexadecane/disc interface. He showed that the boundary condition depends on the interfacial energy and the solid surface roughness. He finally concluded that wall slip is responsible for the limiting shear stress. However, slippage has never been observed directly in representative EHD contacts because of the very short transit time, the very thin thickness of the lubricant film and the motion of the two surfaces.

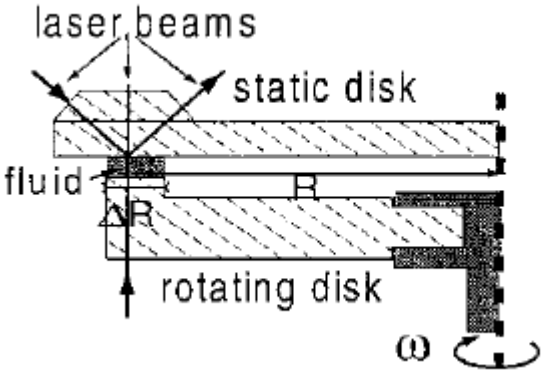

Figure I-8: Schematic of half of the flow cell used by Pit et al. [18].

I.4.2 Shear localization

To explain the evolution of the friction coefficient observed in highly loaded contact, Evans and Johnson [19] proposed a mechanism by which the nonlinear transition is attributed to the thermal activation model of Eyring and the plateau-like behavior is explained by shear bands, similar to the one that occurs in the deformation of solid polymers. The shear stress may be non-uniformly distributed (because of the heat generation within thin lubricant layer) and thus localized within the lubricant film. Indeed, most lubricants are poor thermal conductors, which can lead to thermal gradients inside the lubricant film. Because of the strong dependence between temperature and lubricant viscosity, an inhomogeneous shear can take place across the lubricant film. Recent experimental results showed that two kinds of localized shear response can take place in the bulk lubricant [20]: isothermal or thermal shear localization.

For isothermal shear localization, shear bands occur when the lubricant is pressurized around its glass transition, subjected to high shear stress and low shear rate in order to keep constant the temperature. For thermal shear localization, shear bands have been observed under simple shear by Bair et al.[75], the occurrence of shear bands being due to shear heating. They also theoretically predicted this localization process. According to Plint [22], the LSS is reached when the shear deformation becomes localized. The localized shear deformation is characterised by the formation of thermally softened regions in the middle of the lubricant film. Using a high-pressure flow visualization cell, Bair et al [23] observed the appearance of multiple shear bands under certain conditions of pressure, temperature and shear rate for 5P4E, MCS 1218 and LVI 260 lubricants. They found that the inclination is 19 to 20 degree for 5P4E, about 23 degree for MCS 1218 and 16 to 19 degree for LVI 260. The angle of inclination, θ seems to be a material property and can be related to the pressure-limiting stress coefficient (γ). Bair et al. [75] showed that the first shear band occurs as soon as the lubricant behavior becomes non-linear, and then the number of shear bands increases with an increase of shear

rate until to fill the entire shearing region. The results suggest that the limiting shear stress of the lubricant is the aggregate effect of these mechanical shear bands. According to Bair results, two types of shear bands can be identified (Figure I-9): in the first one, the shear bands are aligned with the flow direction and in the second one, the shear bands are aligned with the cross-film direction. Bair et al [75] concluded that the shear bands develop in the bulk lubricant when it is subjected to high shear stresses and to pressures close to its glass transition pressure. Using the Mohr–Coulomb slip model, the formation of shear bands was predicted by Bair and McCabe [23] However shear bands has never been observed in a living EHD contact.

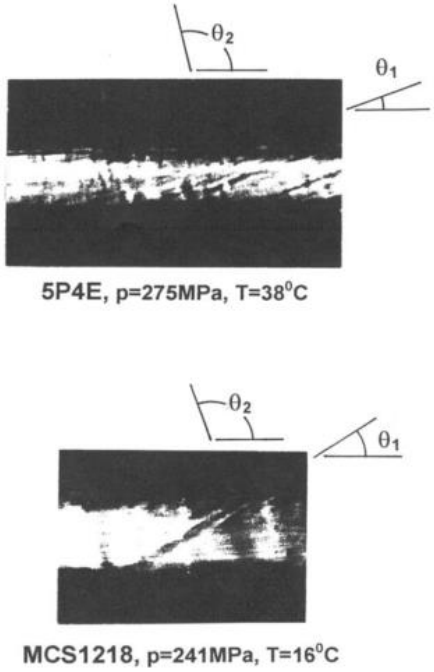

Figure I-9: Micrographs of mechanical shear bands observed at given state conditions [23].

I.4.3 Plug flow

Until now the full understanding of the lubricant flow in EHD contacts is still open to debate. Jacobson [24] was among the first to propose that the lubricant does not behave as a fluid in an EHD contact. In term of flow distribution, he suggested that a very thin zone near the solid surfaces is sheared while a large portion of the lubricant film behaves as a core of solid or a plug (Figure I-10). The core consists of highly viscous lubricant at a liquid or a glassy state. Since then, significant progress have been achieved in particle tracking velocimetry (PTV) technique. Sperka et al. [25] used a mixture of mineral oil with graphite nano-particles in the form of flakes in order to determine the velocity profiles in an EHD contact under sliding conditions. These particles did not influence the lubricant flow, thanks to their small thickness. The motion of graphite nano-particles was optically tracked to obtain their velocity during their passage through the contact zone. Sperka et al. showed that the particles enter the contact at

different velocities, but after certain time their velocity remains uniform and approximately equal to the mean lubricant velocity. The type of flow observed under these conditions has been attributed to a plug-flow mechanism, where a large portion of fluid at the center flows at the mean lubricant velocity and velocity gradients occur near the contacting surfaces (Figure I-11). The plug-flow mechanism could explain the physical origin of the LSS. Ponjavic et al. [76] used a photo bleached-fluorescence imaging velocimetry technique to visualize the flow of polybutene, confined and sheared between a sphere and a flat surface while normal pressure was applied. Their results suggested that there is a critical pressure below which the through-thickness velocity profile is close to linear. At higher pressures, the lubricant film may behave as a plug flow, and the critical pressure for the flow profile transition varies with the molecular weight.

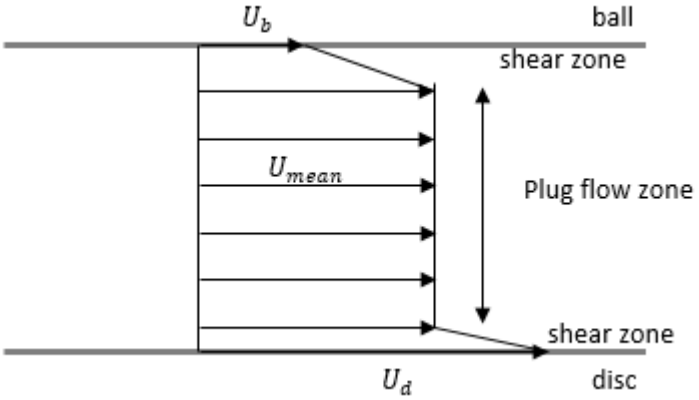

Figure I-10: Schematic representation of plug flow mechanism from Šperka et al. [25].

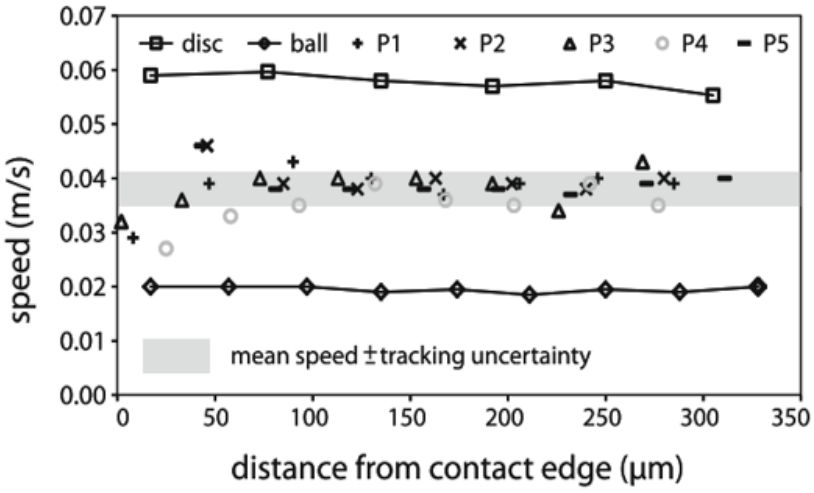

Figure I-11: The motion of particles optically tracked to obtain its speed during the passage are compared with the speed of disc and ball. The gray area depicts the mean lubricant speed including tracking speed uncertainty from Šperka et al. [25].

This scenario is very interesting as it can make the link between each of the different scenarios explaining LSS. Indeed, the core of the flow is mostly assumed to be in a glassy state. Then,

this scenario can be considered as a particular case of shear localization, with the shear localized in a very thin zone near the solid surfaces. Finally, in the asymptotic case of the thickness of these sheared zone would reach a molecular size, this scenario could also be considered as wall slip.

I.4.4 Lubricant phase change

The structure state of the lubricant under very high pressure (>1 GPa) remains not clear. Several experimental and numerical studies have been made in order to understand the lubricant behavior in highly loaded-contact. According to many authors, among them Alsaad et al. [26], many lubricants are near the glassy state in EHD contacts. However, glass transition is very difficult to define as it depends on both thermodynamic and kinetic aspects. The glass transition temperature could be defined as the point from which the molecular structure of a liquid begins to behave like a solid, because of the freezing of the micro Brownian motion. Thus, this particular state must be taken into account since mechanical and thermal properties of a lubricant in a glassy state depend on both the transition thermodynamic parameters (temperature and pressure), and the transition kinetics (how the lubricant transits to the glassy state). Moreover, it could even be expected that the lubricant behavior in the liquid state is already influenced by its glass transition temperature (or pressure), as it is suggested by the widely used WLF viscosity model [42]. As in the model, the lower the investigated pressure, the lower its influence on glass transition. That is why, in most rheological studies, this influence can be neglected, but it probably cannot be the case in EHD contacts.
Furthermore, glass transition of a lubricant may also influence the film thickness, depending on the location of the transition in the contact. It could, therefore, call into question the film thickness prediction in the most loaded contacts.

Since we deal with a “solid-like” state of a fluid, it is important to remind that the lubricant microstructure in EHD contacts is, at best, amorphous. Indeed, literature can be confusing, specifically the Molecular Dynamics literature, where many papers report crystallization of fluids under high pressure in static conditions. But crystallization is promoted by a low fluid complexity, a high degree of molecular ordering at the walls and an initially crystallized fluid [77–80]. In EHD contacts, the complexity of lubricant molecules and the very short times of pressurization / high dynamic conditions lead to amorphous microstructures [67]. That is why, to avoid any confusion, the word “solidification” is not mentioned in this work.

Glass transition has been highlighted by several authors. Recently, direct measurements of velocity profiles in an EHD contact have been performed under pure sliding conditions [27] by using Image-based fluorescence recovery after photobleaching (FRAP) analysis. The velocity

profiles deviate from the linear one predicted by the Reynolds equation and suggest the possible existence of a lubricant phase change at high pressure.

Some authors have associated this « solid-like » behavior to the contact dynamics. Thus, the results of Johnson et al [43, 81] suggest that the lubricant behaves as an elastic solid under the conditions of pressure, temperature and shear rate of their experiments. They [43] measured the friction in a rolling contact with low sliding speed and near isothermal conditions. From the friction results, the apparent viscosity of the oil (Turbo 33) was deduced and plotted as a function of pressure and temperature, as shown on *Figure I-12*.

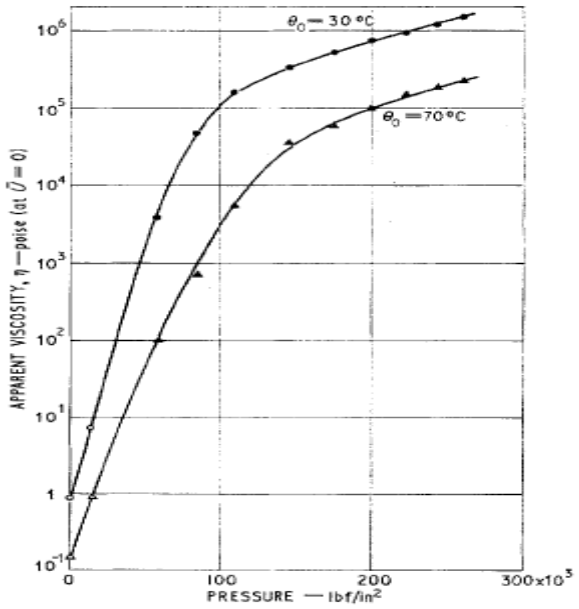

○, Δ from static viscometer measurements

●, ▲ from disc machine measurements

Figure I-12: Variation of apparent viscosity with pressure and temperature from Johnson et al. [43].

The variation of the apparent viscosity with pressure shows a marked change above 10^3 Pas. According to Johnson et al. [43], this change indicates a change in physical properties of the oil at high pressure. Pressures of about 0.57 and 0.88 GPa were obtained at 30 and 70°C respectively by extrapolating the linear sections. Their results showed a good agreement with the glass transition pressures obtained from dilatometry measurements [26].

Such behavior was confirmed by Johnson & Tevaarwerk [28] as well as other authors with others fluids. With increasing the pressure, the lubricant behavior transits from a viscous regime to a viscoelastic one and finally to an elastoplastic regime [82].

With the same idea, using high frequency oscillating shear, Barlow et al. [83] proved that viscous fluids exhibit a viscoelastic behaviour at varying pressures and temperatures. They showed a transition from a predominantly viscous to a predominantly elastic behavior when the oscillation period was progressively decreased to a value less than the Maxwell relaxation time. Finally, this solid-like state of a lubricant in an EHD contact might be a necessary

condition for LSS to occur, but is not sufficient to initiate the observed asymptotic behavior, as shearing seems to play a major role. Back to 1974, Briscoe and Tabor [84] already tryied to provide a full scenario of highly loaded and highly sheared contacts. They suggested that a lubricant in glassy state and submitted to high shear rate could experience fracturation, which would lead to slip at the lubricant/solid interface. Unfortunately, up to now, no experimental evidence has confirmed this scenario.

All the scenarios described above are based on experiments carried out without simultaneous measurement of friction which does not make it possible to better understand the physical origin of the LSS. However, some interesting works have been made in order to evaluate the relationship between pressure, temperature and LSS.

I.5 Experimental approach

As mentioned in the previous section, LSS may stem from various mechanisms. Therefore, LSS is likely to depend on a large number of factors. Among these, pressure and temperature are the most studied in literature, even if their influence is still not well clarified. But other parameters could be considered, as the fluid itself, the loading history or the contacting surfaces.

One of the pioneering experimental works on the different parameters affecting the LSS has been done by Johnson and Tevaarwerk [28]. They performed friction measurements by using a disc machine. They first demonstrated that the drop in friction at high sliding velocity is predominantly a thermal effect, as shown in *Figure I-13*.

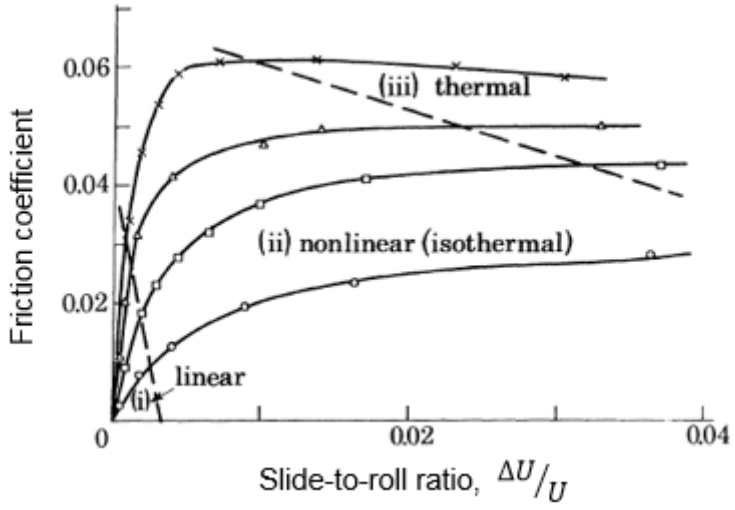

Figure I-13: Friction coefficient as function of slide-to-roll ratio at varying mean contact pressures, $\bar{p}$: 0.40, 0.51, 0.68, 1.3 GPa from Johnson and Tevaarwerk [28].

They also investigated the LSS dependence with pressure. Mean shear stress was calculated as the ratio of the friction force F_X divided by the Hertzian contact area. From these experiments, Johnson and Tevaarwerk [28] established a linear variation of the LSS with pressure.

$$\tau_L = \tau_0 + \gamma \bar{P} \quad \text{(I-12)}$$

τ_0 is the limiting shear stress extrapolated at zero pressure, but has no physical meaning since there is no valid reason why a LSS could occur under this condition. Values of τ_0 have been measured by Jacobson [32] and are of the order 1 - 5 MPa. γ is the LSS-pressure coefficient. It is a constant that must be known to calculate the limiting shear stress at different pressures. According to Bair and Winer experiments, its typical value ranges from 0.05 to 0.1 for mineral and synthetic oils. Bair and Winer results were based on experimental measurements carried out between -27°C and 40°C with pressure up to 1.2 GPa.

Höglund and Jacobson [29] built an experimental apparatus, allowing to reach high pressure (2.2 GPa) and high temperature (200°C), to evaluate the dependence of the LSS with pressure and temperature. They tested several types of lubricants: mineral, synthetic and grease. The LSS variation with pressure for a polyglycol-type oil is shown on *Figure I-14*. Their results led to three main conclusions.

-First, they stated that for each lubricant, depending on the applied temperature, there is a critical pressure above which the LSS increases suddenly. The pressure at which the LSS starts to increase corresponds to what they call the “solidification pressure” of the lubricant, interpreted here as the glass transition.

-Then, beyond this critical pressure, the LSS increases linearly with pressure, as described by equation (I-12) in which $\bar{P}$ is the mean pressure. The γ parameter calculated for each applied condition is the slope of the LSS-pressure dependence, belonging to a range which could be extended to 0.02-0.15. The data are gathered in *Table I-1*. The experimental results showed that the LSS-pressure coefficient, γ, decreases with temperature, and the glass transition pressure increases with temperature.

Lubricant No.	Figure No.	Slope $\frac{\partial \tau_L}{\partial p}$/"solidification"-pressure (GPa)			
		40°C	55°C	70°C	100°C
1	5	0.034/0.82	-	0.028/1.19	0.026/1.66
2	6	0.036/0.65	-	0.032/1.03	0.028/1.48
3	7	0.030/0.82	-	0.027/1.24	0.028/1.77
4	8	0.055/1.41	0.041/1.66	-	-
5	9	0.076/1.21	-	0.069/1.73	-
6	10	0.040/1.46	0.033/1.82	-	-
7	11	0.029/1.74	-	-	-
8	12	0.030/1.44	0.026/1.74	-	-
9	13	0.14/0.61	-	0.091/0.82	0.059/1.07
10	14	0.044/1.54	0.036/1.91	-	-
11	15	0.044/0.63	-	0.037/0.96	0.033/1.37

Table I-1: LSS-pressure coefficients for different lubricants at different temperatures from Höglund and Jacobson [29].

Finally, they concluded that all the mineral oils tested behave in a similar way whereas the pressure dependence of the LSS of synthetic oils strongly depends on the chemical nature of the lubricants.

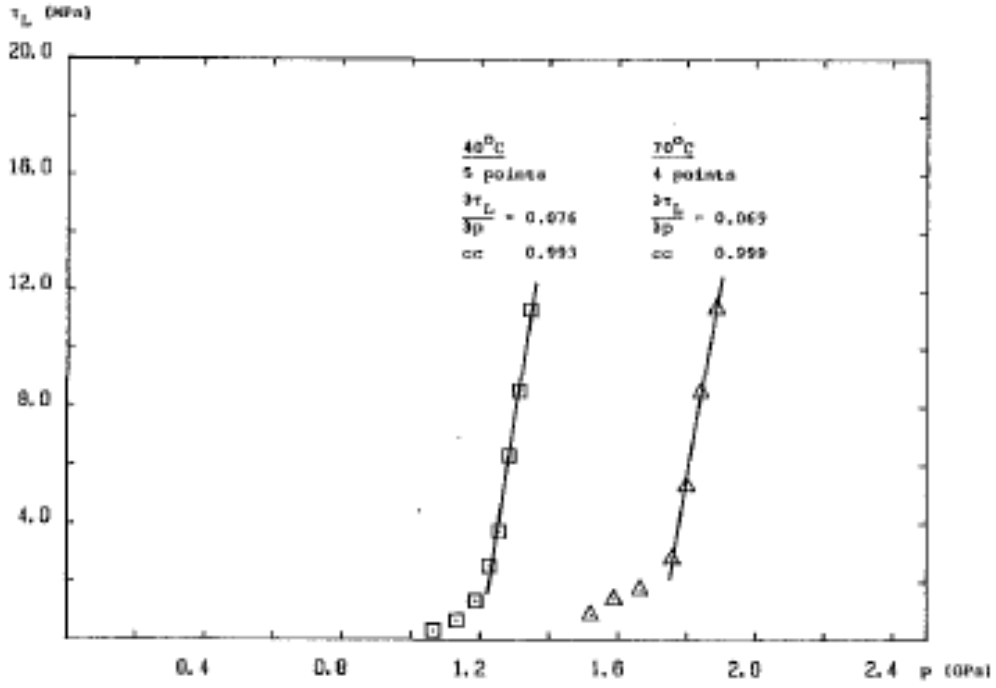

Figure I-14: LSS for a polyglycol-type oil, as function of pressure and temperature from Höglund and Jacobson [29].

Höglund [85] proposed a new method for the experimental evaluation of the shear stress of lubricants at high pressures. The experiments were performed on a jumping ball apparatus at room temperature and a nominal pressure of 5.0 GPa. The main parts of the apparatus are a lubricated sintered-carbide surface and an impacting steel ball. A picture-processing system was used to examine the ball trajectory after impact and to calculate the limiting shear stress pressure coefficient of the lubricant. Different type of lubricants were tested at least 7 times in order to obtain a representative mean value of γ. Here again, Höglund found that the chemical structure of the base oil is of major importance in determining the limiting shear stress pressure coefficient and that additives have only a slight influence on the γ value.

It must be noted that some authors [65] found a γ parameter varying with pressure, signifying that equation (I-12) would not be applicable under all the operating conditions. Thus, in the 1990s, Bair and Winer [65] used a high shear stress rheometer to characterize the pressure and temperature dependence of the LSS for two kinds of lubricants: a mineral oil (LVI260) and a synthetic oil (5P4E, polyphenyl ether). Their experimental results (*Table I-2*) showed that, at a given temperature, the LSS increases with pressure. $\tau_L P$ (P, the mean pressure) is the LSS-pressure coefficient which is not constant, contrarily to the trends reported from other works. It can however be supposed that, due to the low pressures reached in this study, the fluids did not experience glass transition. This could explain the coefficient $\tau_L P$ sensitivity with pressure. Besides, it can be noticed that this sensitivity decreases with increasing pressure, with a fluid closer to a glassy state. It reminds the results of Höglund and Jacobson [29] who measured (Figure I-14) a non-linear variation of the LSS with pressure at very low pressures, up to a critical pressure beyond which equation (I-12) could be adjusted.

Material	T/°C	p/MPa	τ_LMPa	τ_Lp
5P4E	20	124	11.0	0.089
	20	110	10.1	0.092
	20	97	8.5	0.088
	5	51.7	9.5	0.184
	5	41.4	8.0	0.193
	5	31.0	6.6	0.213
	5	20.7	5.6	0.271
	5	1.73	1.8	1.04
LVI260	20	207	8.3	0.040
	20	172	5.5	0.032
	10	166	6.2	0.037
	10	110	3.4	0.031
	5	124	5.0	0.040
	5	97	3.5	0.036
	5	69	2.5	0.036

Table I-2 : Pressure and temperature dependence of limiting shear stress, τ_L from Bair and Winer[65].

Hirst and Moore [30] used a similar method of friction measurement to that described by Crook [57] to measure the friction of two different mineral oils, a paraffinic oil L63/1266 and a naphthenic oil L63/1271. Their experiments covered a large range of pressure (1 to 3 GPa). Steel and tungsten carbide discs were used. Hirst et al. [30] showed that the maximum shear

stress, (or LSS) increases linearly with the mean contact pressure, $\bar{P}$($\bar{P} = \frac{2}{3} * P_{Hertz}$) for the two mineral oils, as shown in *Figure I-15*. They also demonstrated that the LSS value is independent of the nature of the contacting surfaces.

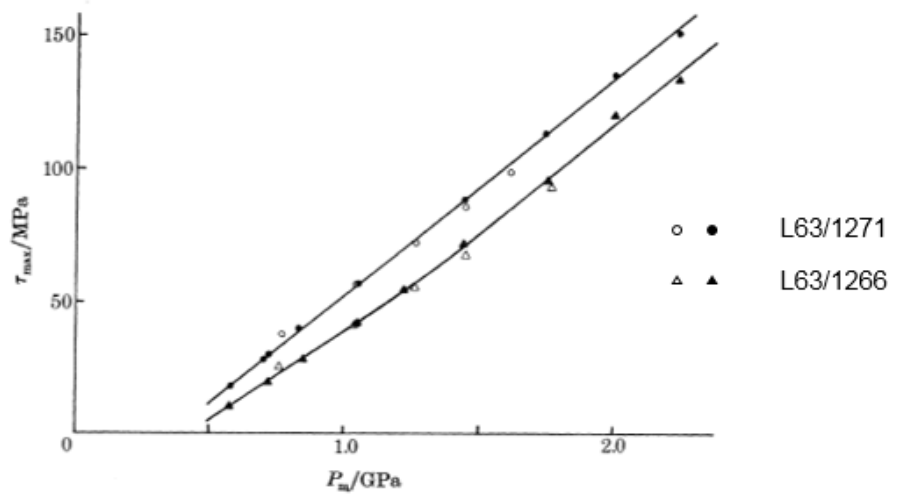

Figure I-15: Maximum shear stress as a function of mean pressure, from Hirst et al. [30].

In a previous paper Bair and Winer [86] showed that the LSS value depends on the lubricant loading history, due to the influence of the transition kinetics from liquid to glassy state. The isothermal compression history results in a lower LSS, which agrees with the friction peak measurement in EHD contacts.

In view of all these results of LSS from various authors, a natural pending question is the comparison between them, to validate their independence from the experimental setups.

The LSS pressure dependence of 5P4E was studied by Ramesh and Clifton [87] by using a new pressure-shear plate impact experiment based on the Hopkinson bar principle. Their experiments covered a larger range of pressure (1-5 GPa). The lubricant was confined between two hard metallic plates which were subjected to impact by a parallel plate. The advantage of this device was that the pressure was much uniform over the contact than in twin disc machine. The results of Ramesh and Clifton for 5P4E at 40°C showed an acceptable agreement with the ones of Bair and Winer [63] and Evans and Johnson [19], obtained with different devices, as shown on Figure I-16. It must be noted that the investigated temperature was slightly lower in the Bair and Winer study, 38°C instead of 40°C.

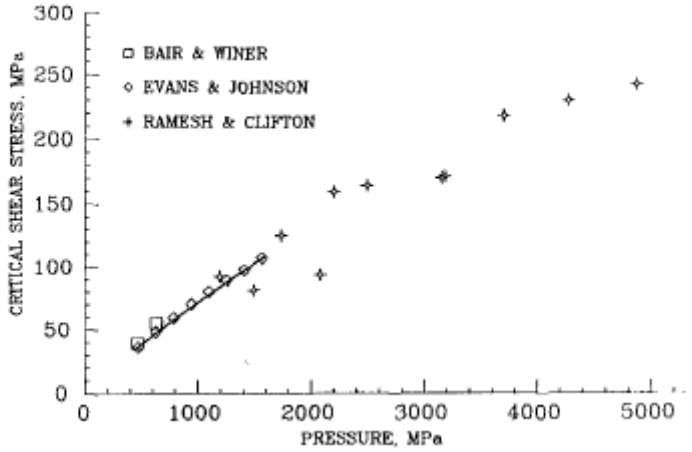

Figure I-16: Comparison of Bair [63]*, Evans* [19] *and Ramesh* [87] *results on 5P4E, at temperatures close to 40°C.*

For three lubricants (5P4E, LVI 260 and Vitrea 79) Bair and Winer [86] compared their LSS measurements obtained from a high pressure cell and those obtained by Johnson and Tevaarwerk [28], from disc machine tests. Their experiments were performed at the same average pressure and essentially same temperature. Results are summarized in *Table I-3*. They found a good agreement between these two different methods. Bair and Winer concluded that the limiting shear stress is the material property governing the friction under the operating conditions investigated.

Fluid	Limiting shear stress, τ_L, at $P = 0.67$ GPa	Average shear stress based on traction measurement at a slide-roll ratio of 10^{-1}, average pressure of 0.67 GPa
5P4E	58 MPa (38°C)	55 MPa (35°C)
Vitrea 79	31 MPa (26°C)	33 MPa (30°C)
LVI 260	49 MPa (35°C)	51 MPa (35°C)

Table I-3: Comparison of limiting shear stresses of ref [86] *and ref* [28]

Finally, as seen in the results of Höglund and Jacobson [29], who showed that the LSS-pressure coefficient, γ, decreases with temperature, some authors investigated the influence of temperature on the LSS.

On one hand, Evans and Johnson [19] investigated the pressure dependence of LSS for two lubricants, using disc machine test: a synthetic polyphenyl ether 5P4E and a traction fluid Santotrac 50. Their experiments covered a wide range of pressures, up to 1.6 GPa and temperatures, up to 100°C. Their results showed also a linear variation of the LSS with pressure. But they found that the LSS for 5P4E was independent of temperature over the range 25-100°C and, for Santotrac, a slight decrease in LSS with temperature was observed. These results were also supported by the preliminary experiments of Jacobson [32] using the oblique

impact apparatus. He finds that the rate of increase of LSS, with mean pressure to be 0.082 for a traction fluid and about 0.05 for two mineral oils.

On the other hand, Bair and Winer built a new high pressure cell [41] in order to extend the applied pressure range. They characterized the rheological properties of 5P4E (polyphenyl ether) at three temperatures (20, 40, 80°C) and by varying the pressure above and below the glass transition pressure. The results are shown on *Figure I-17*.

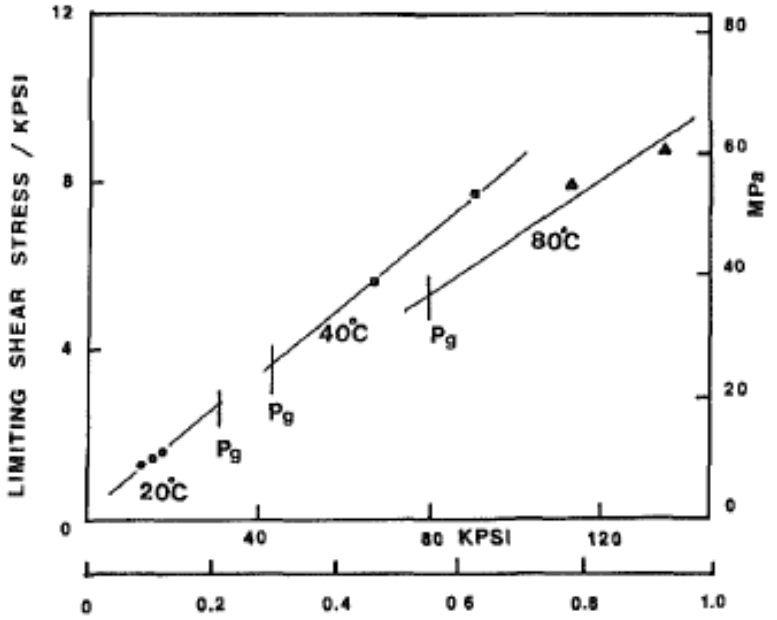

Figure I-17: LSS of 5P4E as function of pressure from Bair and Winer [41].

This large panel of pressure and temperature experimental conditions enabled them to provide a model of LSS depending on both parameters. They showed that the LSS of 5P4E increases linearly with pressure, and can be described by the following equation:

$$\tau_L = \lambda(T)p \qquad \text{(I-13)}$$

$$\lambda = 0.095 - 0.0035T$$

In this equation the pressure and temperature are coupled.

Like Evans and Johnson [19], Houpert et al. [31] established a LSS model for a synthetic diester oil by using a two disc machine test. Their experiments were carried out in the temperature range from 24 to 105 °C and for pressures from 0.57 to 1.14 GPa. For a given mean pressure and temperature, a first approximation of the LSS was obtained by taking the maximum value of the friction coefficient. Then an adequate value of LSS was found by numerically fitting the friction curve. They found that in the range of these conditions, the temperature and pressure dependence of LSS was described by the following equation:

$$\tau_L = (0.015p - 1.88.10^6)exp\left(585\left(\frac{1}{T+273} - \frac{1}{313}\right)\right) \qquad \text{(I-14)}$$

Based on numerical analysis of thermal EHD contacts, Hsiao and Hamrock [88] found a new LSS expression (eq.(I-15)) which is different from the other models detailed before.

$$\tau_L = \tau_0 \left(1 + \frac{\gamma p}{\tau_0}\right) exp\left[\beta \left\{\left(\frac{1}{T - T_R}\right) - \left(\frac{1}{T_0 - T_R}\right)\right\}\right] \quad \text{(I-15)}$$

In isothermal conditions ($T = T_0$) this LSS expression is reduced to Johnson and Tevaarwerk model (I-12).

Finally, it can be concluded from this review that the value of LSS is influenced by the lubricant itself, the contact pressure and temperature, and by the loading history but not the nature of the contacting surfaces. Some authors provide models of LSS only depending on pressure and temperature, both parameters being coupled in all of them.

Acceptable agreements between results provided by several authors have been obtained, but some discrepancies still exist, which may be due to inaccuracy in the control of some influencing parameters.

I.6 Conclusion

Until now the physical origin of the LSS remains unclear. Indeed, the extreme conditions of pressure and film thickness make the measurement of this asymptotic behaviour very delicate. Furthermore, a very accurate control of all the operating conditions is required to apprehend their influence on the LSS.

Literature provides several scenarios in order to explain the mechanisms which could trigger LSS. Unfortunately, LSS has never been simultaneously measured in EHD contact to validate any of them. Besides all of them have limitations because they were based on measurements performed outside the EHD contact.

Some research efforts have been made in literature to take into account the LSS variations in rheological models. Several empirical models of LSS have been provided to describe its dependence with pressure and temperature. These models arose from measurements performed by using different experimental test-rigs, like disc machines, high pressure cells or impacting devices.

In the next chapter of this work a new simple bilinear model to describe the temperature-pressure dependence of LSS under nominal isothermal condition is presented. Our model is deduced from a large set of friction measurements performed on a pure diester fluid (benzyl benzoate), and validated on a well-known lubricating oil (T9, Shell). Experimental conditions were designed to limit the lubricant thermal effects on the friction response.

II Pressure and temperature dependence of the limiting shear stress

II.1 Introduction

As mentioned in the previous chapter, several LSS models have been proposed in literature in order to evaluate the relationship between LSS, pressure and temperature. A number of researchers found a linear dependence of LSS with pressure, using different lubricants as mineral and synthetic oils. However, in these models, a coupling term between pressure and temperature makes impossible to separate the mechanical and thermal contribution on the LSS. Furthermore, these models include a limiting shear pressure coefficient which is sometimes different from one author to another. Up to now there is no general model to predict pressure and temperature dependence of LSS.

The present chapter presents a phenomenological approach to describe the dependence of LSS with pressure and temperature. A model is derived from experiments carried out under nominal isothermal conditions by using a ball-on-disc tribometer called Jerotrib. In a first part experimental conditions have been set to reduce as much as possible shear heating of the lubricant in order to uncouple the pressure and temperature of the LSS. Then, in a second part the dependence of the LSS with pressure and temperature is derived from friction curves for two types of lubricants, a pure fluid (benzyl benzoate) and a turbine mineral oil (T9).

II.2 Lubricant properties

Two lubricants were used in this experimental work. The first one is benzyl benzoate (supplied by abcr GmbH, purity 99%, CAS 120-51-4), an organic compound of formula $C_6H_5CO_2CH_2C_6H_5$, which is the ester of benzyl alcohol and benzoic acid. Its rheological characterization has been performed following the approach described into details in [33]. Its rheological properties are summarized over a wide range of temperatures and pressures in Appendix A. The choice of this lubricant was motivated by its very intense response in Raman and Brillouin spectroscopy. Its spectroscopic characterization will be described in the third chapter.

The second fluid is an industrial lubricant of different nature, a commercial turbine mineral oil (Shell T9). It has been already studied in the literature and the rheological properties of the specific batch used in this work are described in Wheeler et al [34]. More details on its rheological properties may be found in Appendix B.

II.3 Definition of the operating conditions

The first step is devoted to set the experimental conditions to avoid shear heating of the lubricant. Indeed, thermal dissipation on friction measurements tends to decrease the friction coefficient above a critical value of SRR. This section aims to find out the optimal operating

conditions to avoid as much as possible thermal effects influence on the friction measurements. These operating conditions will be used to evaluate pressure and temperature dependence of LSS. For that purpose, a series of experiments has been done on both lubricants, benzyl benzoate and T9 to highlight the dependence of the lubricant shear heating on its LSS within the range of operating conditions.

II.3.1 Experimental setup

Friction measurements were performed with a ball-on-disc tribometer called Jerotrib (Figure II-1). The two specimen (a ball and a disc) are driven independently with two motors equipped with optical encoders of 2.10^4 steps per revolution combined with a 8-bit discretization to apply any desired SRR with high accuracy. The relative sliding of the two specimens or SRR can be expressed as follows:

$$SRR = \frac{\Delta U}{U_e} = 2\frac{U_{ball} - U_{disc}}{U_{ball} + U_{disc}} \quad \text{(II-16)}$$

$$U_e = \frac{U_{ball} + U_{disc}}{2} \quad \text{(II-17)}$$

with U_e, the mean entrainment velocity, U_{ball}, the ball velocity and U_{disc}, the disc velocity. The SRR is equal to zero in the pure the rolling condition and different from zero in rolling-sliding conditions.Three material configurations were used: a 100C6 steel ball against either a 100C6 steel disc or a sapphire disc, and a tungsten carbide (WC) ball against a WC disc. Their material properties are given in Table II-1. The measured surface roughness of the specimen is for the steel ball $\sigma^{RMS}_{steel\ ball} \sim$ 5 nm, the steel disc $\sigma^{RMS}_{steel\ disc} \sim$ 10 nm and the sapphire disc $\sigma^{RMS}_{sapph.\ disc} \sim$ 8 nm. In the case of WC specimen, the roughness is the same for the disc and the ball: $\sigma^{RMS}_{WC} \sim$ 20 nm.

The diameter of the ball specimen is 25.4mm. The contact radius on the disc may range between 30 mm and 36 mm, and is systematically controlled. For an entrainment velocity (U_e) of 3 m/s and SRR= 1%, the relative uncertainty on SRR is lower than 6% and this value drops significantly when the SRR increases.

Materials	E (GPa)	ν (-)	ρ (kg/m^3)	k (W/mK)	C_p (J/kgK)
Bearing steel (AISI 52100)	210	0.30	7850	46	470
Sapphire	360	0.34	4000	40	750
Tungsten carbide	610	0.258	14850	29.3	194.7

Table II-1: Properties of the specimen materials

Jerotrib allows to measure both friction and film thickness. The maximum applied normal load can reach 400N. Normal and friction (tangential) forces (F_Z and F_X in the following, respectively) are simultaneously measured through a multi-axis gauge sensor with a maximum uncertainty of 0.82% for the former and 0.35% for the latter. The friction coefficient, calculated as the ratio between the tangential force measured on the disc and the normal load applied on the ball, has therefore a relative uncertainty $\Delta CF_X/CF_X$ of 1.17%. The forces along the three directions are continuously recorded at a sampling frequency of 100Hz. The friction forces obtained at equal absolute values of the SRR (but opposite signs) have been systematically averaged. Furthermore, some tests have been repeated, leading to a mean relative standard deviation (considering values obtained at SRR>0 and SRR<0) of 2.8% with a rather low dispersion.

The bottom of the ball dips into the reservoir containing the lubricant, ensuring fully flooded conditions. The specimen in contact and the lubricant are thermally isolated and maintained at constant temperature by a unique circulating fluid loop. The central part of the tribometer was designed in such a way to limit any heat transfer from and towards the contact zone, allowing nominal isothermal conditions when using appropriate operating parameters.

In addition, to minimize thermal effects, the duration of friction measurements at each applied SRR is limited to 10s, except when SRR=0 where a 30 s duration was imposed to allow stabilization of the operating conditions. The measured friction force, F_X, is averaged over 7s duration, ignoring the first and the last two seconds to eliminate the latency of the motors. Inlet temperature, $T_{in,}$ was monitored and recorded within ± 0.1°C by a platinum probe located just underneath the ball specimen.

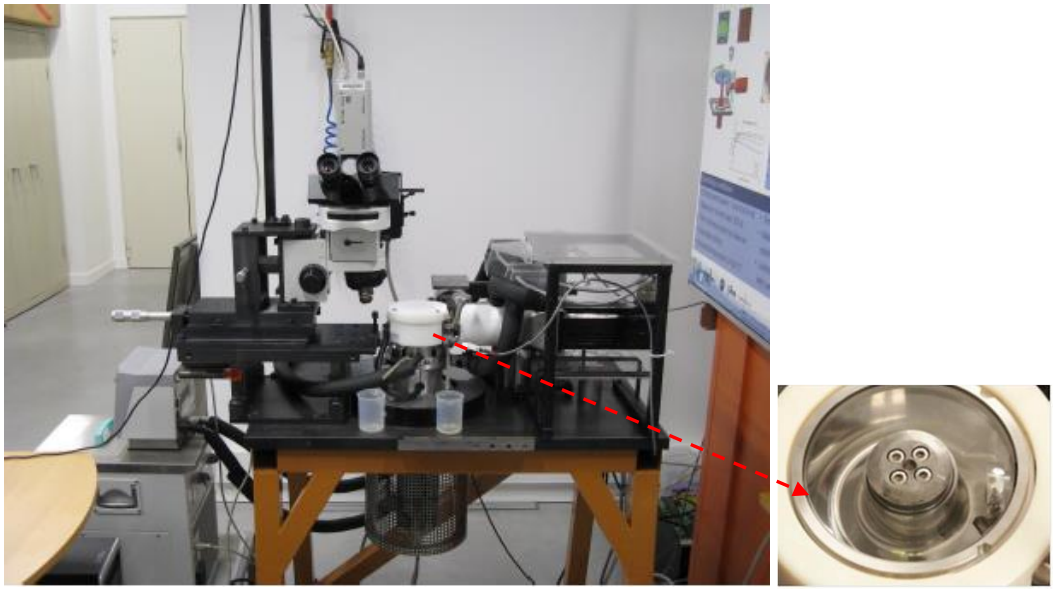

Figure II-1: Jerotrib test-rig.

II.3.2 Limiting shear stress criterion

As shown in the first chapter, at intermediate SRR, friction may present a plateau known as the limiting shear stress (LSS). In this work, the LSS value is reached experimentally when the relative variation of the friction coefficient between two successive SRR does not exceed the friction coefficient measurement relative uncertainties ($\Delta CF_X/CF_X = 1.17\%$). This defines a LSS criterion which was applied to all the experimental conditions.

The mean limiting shear stress value, $\overline{\tau_L}$, was calculated based on the assumption that a friction plateau corresponds to a LSS which occurs all over the contact area. Therefore, the $\overline{\tau_L}$ was defined as the maximum shear stress that can be supported by the lubricant. It was calculated as the maximum tangential force $max(F_X)$, corresponding to the friction plateau, divided by the surface of the Hertzian contact S.

$$\overline{\tau_L} = \frac{max(F_X)}{S} \tag{II-18}$$

where $S = \pi a^2$ and a is the Hertzian pressure contact radius

The relative error on the mean LSS for each applied conditions is lower than 1.2%. It was obtained from the error propagation formula:

$$\frac{\Delta\overline{\tau_L}}{\overline{\tau_L}} = \frac{\Delta F_X}{F_X} + \frac{2}{3} * \frac{\Delta F_Z}{F_Z} \tag{II-19}$$

II.3.3 Possible influence of lubricant heating on the LSS

In EHD, the temperature within the lubricant film highly depends on operating conditions. Indeed, thermal effects significantly increase with the entrainment velocity, the sliding velocity and the normal load submitted to the lubricant. Thermal dissipations arise from two major heat sources: the shear heating of the lubricant and the compressive heating due to pressure variations in the contact area. This latter effect remains small compared to the former. The energy generated by shearing heats up the lubricant and consequently reduces its viscosity. The pioneering work on thermal effects in EHL has been done by Cheng [35]. His numerical results, taking into account both the heat transfer from the lubricant to the solid surfaces and the convection, showed that friction was affected by this temperature rise in the lubricant film [36]. Recently, Habchi et al. [37] demonstrated numerically that the LSS can be significantly influenced by an increase of the temperature through the lubricant film. Indeed, neglecting the heat dissipated in both the inlet and the central area of the contact leads to overestimate the film thickness and the friction coefficient respectively. When thermal heating predominates lubricant rheological response, the friction coefficient starts to decrease.

To highlight the influence of thermal effects on LSS, a set of friction experiments has been performed first on benzyl benzoate by varying U_e from 0.5 m/s to 6.5 m/s at fixed temperature and contact pressure. The increase in entrainment velocity has antagonist effects. On one hand, it tends to increase the film thickness according to the Hamrock and Dowson prediction [38]. On the other hand, it tends to decrease the film thickness due to shear heating. Indeed, for a fixed SRR value, an increase of U_e leads to a higher shear rate, which tends to increase the lubricant temperature and thus to decrease its viscosity. Considering the heat source term $Q_{shear} \sim \eta(P,T) \times \dot{\gamma}^2$ [89] in the energy equation, it comes that there is a non-trivial coupling between the lubricant temperature and viscous dissipation.

The first set of experiments was carried out with the steel ball and the sapphire disc. For each test, the applied pressure was maintained at P_{Hertz} = 1.68 GPa and the temperature at T = 40°C. The operating conditions and resulting LSS values are indicated in Table II-2 along with h_c, the central film thickness calculated with Hamrock and Dowson [38] expression and h_m, the minimum film thickness predicted from the extended Chevalier table [90]. Moreover, to avoid thermal heating at the contact inlet, the film thickness thermal reduction coefficient, ϕ_T, proposed by Cheng [36], was calculated prior to any experiment. It is representative of the occurrence of significant thermal effects at the contact inlet: a $\phi_T \ll 1$ implies significant heating which may influence friction response, whereas a ϕ_T close to 1 stands for an isothermal regime at the contact inlet. Only tests for ϕ_T values above 0.96 were considered. Indeed, in such conditions the lubricant flow can be considered as isothermal, in agreement with past works performed on the same test-rig [37]. The film thickness thermal reduction coefficient ϕ_T is also given in Table II-2. Experimental results are shown on Figure II-2, the inset shows these different trends more clearly. Whatever the applied U_e, all friction curves well overlap in the low SRR domain. For the lowest entrainment velocities (0.5 and 0.8 m/s), CF_X continuously increases (even beyond a SRR of 20%) whilst for the highest values (5 and 6.5 m/s) it reaches a maximum very rapidly at low SRR and then decreases due to shear heating.

For each friction curve, we consider that the LSS is reached if our stability criterion defined in section II.3.2 is satisfied. Hence, the SRR was extended up to 20% for some operating conditions. All the friction curves led to different values of LSS which are reported in Table II-2, together with the lubrication parameter h_m/Σ defined as the ratio between the minimum film thickness, and the solid bodies surface combined roughness ($\Sigma = \sqrt{\sigma_{ball}^{RMS^2} + \sigma_{disc}^{RMS^2}}$). This ratio is representative of the regime of lubrication in the contact. A ratio of 3 is usually considered in literature as the limit between the full separation and the mixed lubrication regimes [40]. The two experiments at low U_e can be considered in the mixed lubrication regime. $\mathrm{SRR_{LSS}}$ is the

SRR at which the maximum friction coefficient is reached, representative of the LSS, before the influence of thermal dissipations.

U_e (m/s)	0.5	0.8	1.5	1.5	2	2	2.5	3.5	5	6.5
φ_T (-)	1.0	0.99	0.99	0.99	0.99	0.99	0.98	0.97	0.96	0.95
h_c (nm)	31	43	65	65	79	79	92	115	146	174
h_m (nm)	< 10	13	20	20	25	25	31	43	60	76
h_m/Σ (−)	1	1.4	2.1	2.1	2.7	2.7	3.3	4.5	6.3	8
SRR_{LSS} (%)	17.5	17.5	10	12.5	10	10	7.5	5	5	4
$\overline{\tau_L}$ (MPa)	73.0	72.0	70.9	70.0	69.9	69.6	69.3	68.9	67.9	67.3

Table II-2: Operating conditions for friction measurements with different entrainment velocities: benzyl benzoate at 40°C and 1.68 GPa (182 N) in steel/sapphire contacts.

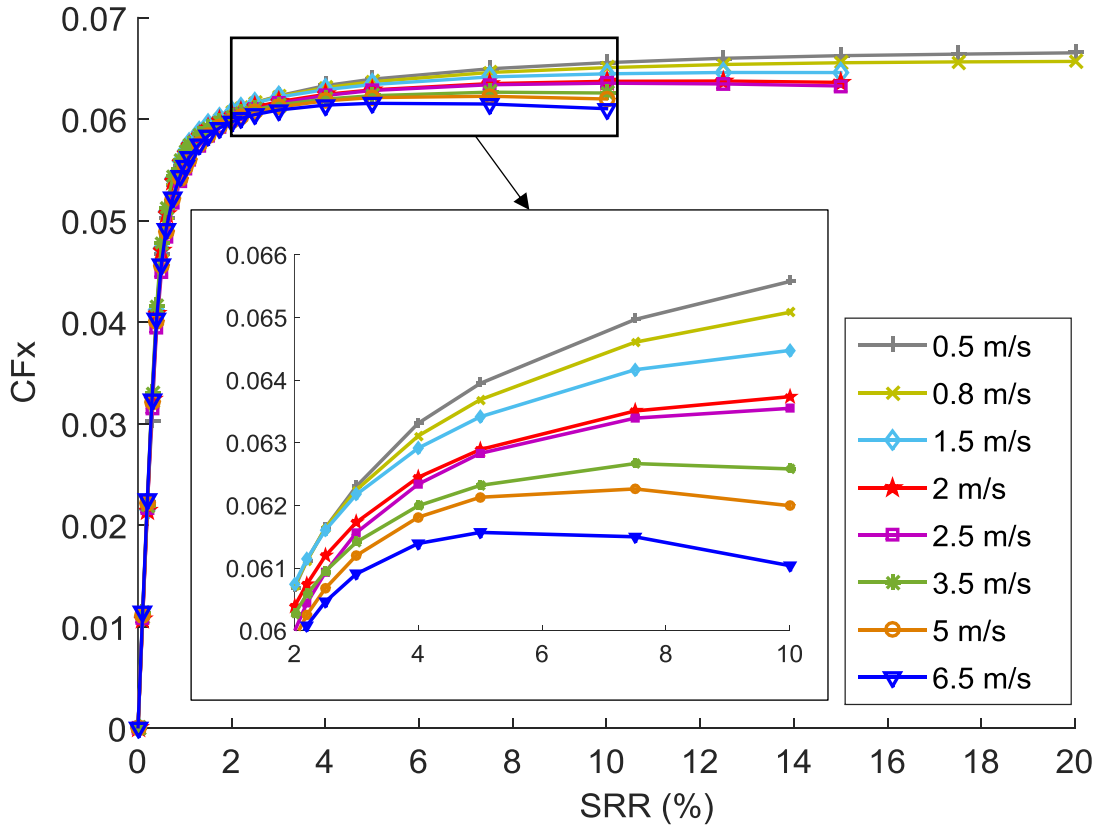

Figure II-2: Friction curves of benzyl benzoate with variable entrainment velocities at P_{Hertz} = 1.68 GPa and T=40°C. A zoom at intermediate SRR is presented in the inset.

LSS values derived from the friction curves relatively to U_e are plotted on Figure II-3, with indications of the full lubrication and the mixed regime. The prediction of the lubrication regime is based on the h_{min}/Σ ratio, if it equal to or greater than 3, we are in the mixed regime, if not we are in the full lubrication regime. The results clearly show a very good agreement between

the prediction of the lubrication regime by the h_{min}/Σ ratio and the measurement of the LSS. The results follow actually two different slopes, depending on which regime take place. Furthermore, in the full film regime, there is a dependence between the LSS value and the entrainment velocity. It can thus be confirmed that the more the lubricant is sheared, the lower the value of LSS is.

As the lubricant self-heating induces a decrease of LSS, measuring a true mechanically-induced LSS would require to minimize this heating, thus tending ideally towards a zero entrainment velocity operating condition. However, the drop in U_e results in a film thickness reduction, until reaching a mixed lubrication regime (left part of Figure II-3). In this regime, several complex phenomena come into play (collisions and dry friction between peaks of roughness, wear and pollution of the lubricant) and speaking about LSS would no longer make sense. On the right side of Figure II-3, therefore for the highest U_e, the LSS continuously decreases under the influence of shear heating. The drop in LSS in the EHD regime is less important than that in the mixed regime. Consequently, to compare meaningful values requires to run experiments in comparable experimental conditions, chosen to minimize the thermal dissipation while ensuring to still work in the full film lubrication regime. According to Figure II-3, an entrainment velocity of about 2.5m/s appears to be an adequate choice to be able to measure “intrinsic mechanically-driven LSS” values obtained in nominal isothermal conditions.

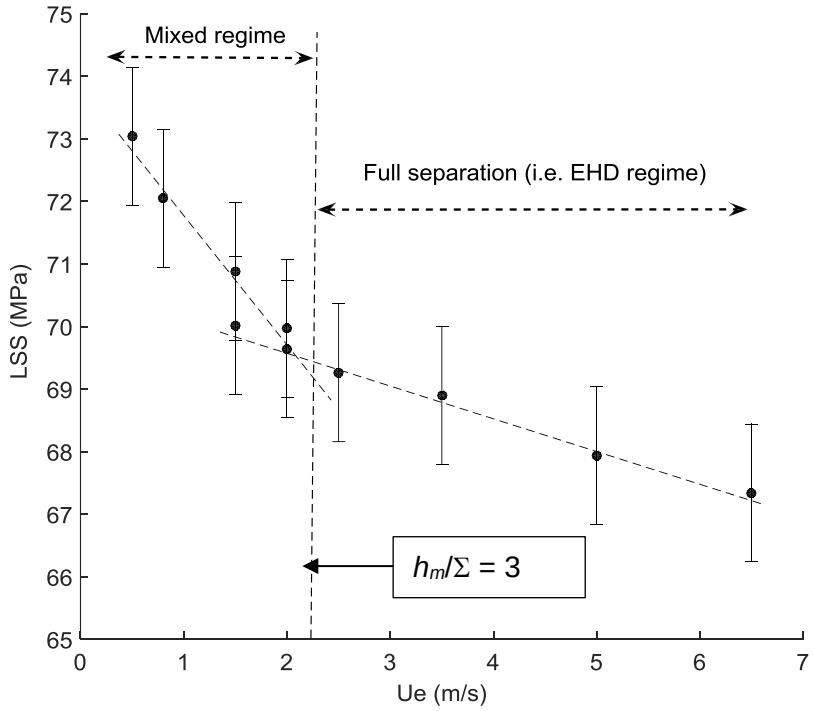

Figure II-3: LSS of the benzyl benzoate as function of the entrainment velocity at constant Hertzian pressure, 1.68 GPa and temperature, 40°C in steel/sapphire contacts.

A way to validate if shear heating occurs during friction experiments is to mesure the inlet temperature during the test.

II.3.3.1 Inlet temperature variation during friction measurements

To verify isothermal conditions, the inlet temperature was recorded all along the friction tests later described in this chapter. For instance, data obtained with benzyl benzoate for the two most severe conditions are gathered in Figure II-4. The measured inlet temperature, T_{in} at 20°C: steel/steel contact at 1.67 GPa and steel/sapphire contact at 2.15 GPa is plotted as a function of the SRR.

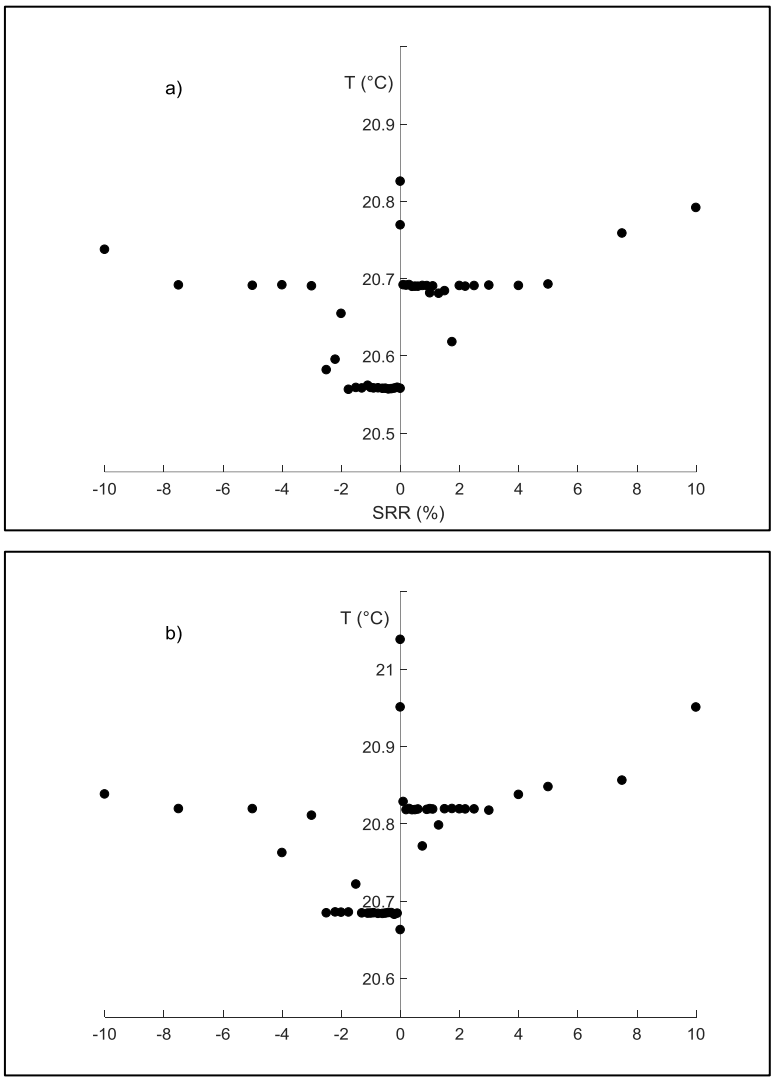

Figure II-4: Inlet temperature variations during friction measurements with benzyl benzoate at T=20°C and U_e=1.3 m/s in:

a) steel/steel contact loaded at 294 N, P= 1.68 GPa,

b) steel/sapphire contact loaded at 384 N, P= 2.15 GPa.

Indeed, tests at low temperature result in high viscosity and high pressure-viscosity coefficient and, therefore, in a higher risk for shear heating. The experiments were run with negative SRR first, from 0 to -10% (duration of 10 s per non-zero step), back to SRR =0 for 30 s, then with increasing SRR from 0 to +10% and finally back again to SRR =0 for 30s. In both cases, the results showed that, at the beginning of the test, the inlet temperature stays almost constant. Temperature starts to increase very slightly at -10% of SRR. The same behaviour is observed for positive SRR. It can be noted that the variation of temperature does not exceed 0.3°C during the whole experiment. Thus, it can be considered that the inlet temperature is kept constant during the whole friction tests. This leads us to conclude that the friction results are not significantly affected by viscous heating at the contact inlet. Therefore, a mechanically-driven LSS of the lubricant is responsible for the friction plateau observed in friction curves of the section III at high or moderate pressure.

Similar experimental protocol as the one developed for characterizing the influence of lubricant heating on LSS with benzyl benzoate were applied in the case of an industrial turbine mineral oil (T9) to validate our conclusions.

II.3.4 Validation with an industrial lubricant

As demonstrated with benzyl benzoate, much attention must be paid to the choice of the operating conditions, especially the entrainment velocity, in order to be in nominal isothermal conditions. To highlight the possible influence of lubricant heating on the T9 LSS, the same experimental protocol than that defined for the benzyl benzoate is applied. Due to the higher viscosity of T9, U_e was varied from 0.3 to 6.5 m/s. Experiments were also performed with a steel ball and the sapphire disc at constant Hertzian pressure of 1.70 GPa and a temperature of 40°C. The experimental results are summarized in Figure II-5. It can first be observed that whatever the applied U_e, all friction curves entirely overlap at very low SRR. Thermal heating influence on friction becomes more and more important when increasing the entrainment velocity: the more U_e increases, the higher CF_X drops with SRR. This explains the fact that the critical SRR, from which the LSS is reached, moves towards lower values of SRR when increasing the U_e. Friction curves start to decrease when thermal heating effects begin to dominate the frictional response of the lubricant.

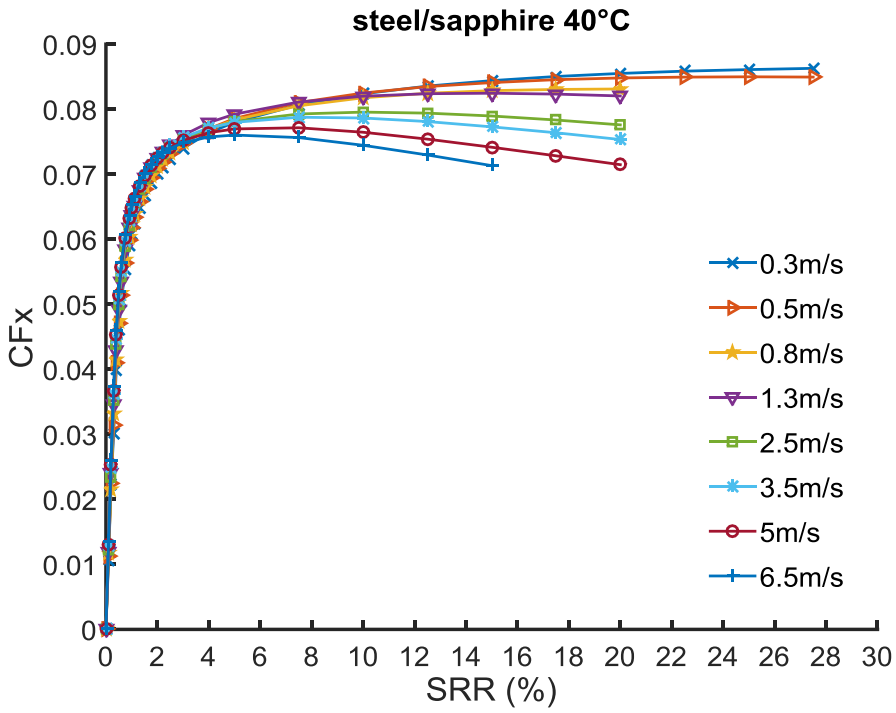

Figure II-5: Friction results of T9 with variable entrainment velocity at P_{Hertz} = 1.70 GPa and T=40°C.

As in the case of benzyl benzoate, there is a dependence between the U_e and the LSS values (see Table II-3). LSS is reached for a calculated shear rate of order of $10^6 s^{-1}$ in the contact center. This value is in accordance with the results found in literature [91]. In Figure II-6, the LSS is plotted as a function of U_e. Again, two linear regions can be observed: below a of U_e 1m/s, the slope of the LSS as a function of U_e is higher than above U_e= 1m/s. Based on the h_{min}/Σ ratio explained in detail in the case of benzyl benzoate, a mixed regime is expected for U_e lower than 1m/s and full film lubrication for U_e greater than or equal to 1m/s. It can be noted that the drop in LSS in the EHD regime for the turbine mineral oil T9 is twice higher than that for benzyl benzoate (1.34 MPa.s/m for the T9 and 0.57 MPa.s/m for the benzyl benzoate). This is due to the fact that the LSS is an intrinsic property to each fluid.

U_e (m/s)	0.3	0.5	0.8	1.3	1.3	2.5	3.5	5	6.5
φ_T (-)	1.00	0.99	0.98	0.99	0.99	0.97	0.96	0.94	0.92
h_c (nm)	38	54.	74	102	102	159	199	253	301
h_m (nm)	12	17	24	36	36	67	91	126	158
h_m/Σ $(-)$	1.3	1.8	2.5	3.8	3.8	7.1	9.7	13.3	16.6
SRR_{LSS} (%)	25	22.5	17.5	12	12	7.5	5	5	4
$\overline{\tau_L}$ (MPa)	98.3	96.9	94.8	93.8	94.3	90.8	90.0	87.9	87.7

Table II-3: Operating conditions for friction measurements with different entrainment velocities: turbine mineral oil T9 at 40°C and 1.70 GPa (190 N) in steel/sapphire contacts.

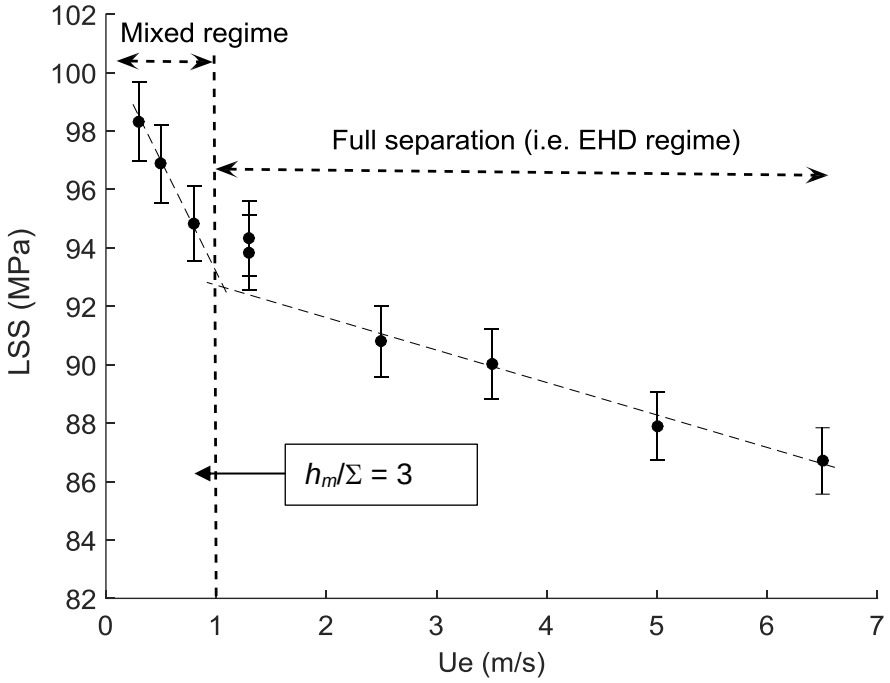

Figure II-6: LSS as function of the entrainment velocity at constant Hertzian pressure, 1.70 GPa and temperature, 40°C in steel/sapphire contacts.

To summarize, a similar tendency of the LSS variation with U_e has been obtained for both lubricants, with a decay depending on the lubricant properties. It suggests that the influence of thermal effects on friction measurement depends on several factors, such as the lubricant thermal properties and the operating conditions. Most of lubricants are poor thermal conductors, which can lead to thermal gradient inside the lubricant film. These preliminary results led us to define the optimal operating conditions for the following part of this work, devoted to evaluate the limiting shear stress dependence on pressure and temperature.

Section II.3.3 and II.3.3.1 showed that it is possible to carry out friction measurements under isothermal or, more realistically, nominal isothermal conditions. The last expression means that even if thermal effects must occur in any friction measurement, it is possible to minimize them and to make the results almost insensitive to a weak energy dissipation within the experimental volume of interest.

Both lubricants described above (benzyl benzoate and T9) are used in the following to investigate the temperature and pressure dependence of LSS. First the experimental results obtained for benzyl benzoate are presented, then those obtained with the industrial lubricant T9, applying the same experimental protocols.

II.4 Friction measurements

II.4.1 Operating conditions

Operating conditions are selected in order to work under nominal isothermal conditions. For this reason, the applied SRR for benzyl benzoate fluid is limited to ±10%. For all tested conditions, the thermal reduction coefficient, φ_T, was maintained higher than 0.96. U_e was adapted for each applied temperature to keep almost constant the lubricant film thickness. Lubricant central film thickness (h_c) was determined with the Hamrock and Dowson model [38]. According to the preliminary results showed in the previous section, the lubricant central film thickness was adjusted between 90 to 130 nm, in order to avoid any damage between the contacting surfaces as well as to limit shear heating.

In order to vary the contact pressure range, the three ball-on-disc configurations were tested: steel/steel, steel/sapphire and WC/WC, with a maximum applied load of 400N. The maximum pressure in the contact P_{Hertz} is given by the Hertz theory:

$$P_{Hertz} = \frac{3F_Z}{2\pi a^2} \quad \text{(II-20)}$$

Steel/steel, steel/sapphire and WC/WC led to Hertzian pressures from 0.68 to 1.68 GPa, 1.00 to 2.19 GPa and 1.68 to 3.0 GPa, respectively. For all the tested conditions, the contact radius lay between 10^{-4} and $2.9.10^{-4}$ m.

The applied temperatures were 20, 40, 60 and 80°C. Experimental conditions are given in Appendix C. At high temperature, a higher pressure needs to be applied to reach the friction plateau-like behavior because the lubricant becomes more fluid. That's why for the highest temperature of 80°C, the friction measurements have been performed with only steel/sapphire and WC/WC contacts. For temperatures of 20 and 40°C, friction measurements have been carried out with steel/steel, steel/sapphire and WC/WC contacts, for temperature of 60°C, steel/steel and steel/sapphire contacts. The applied U_e varied from 1.3 m/s at 20°C to 6.5 m/s at 80°C in order to maintain an almost constant film thickness at the contact center. Depending on the combination of temperature, pressure and U_e, the LSS was reached or not. The main experimental results for the different operating conditions tabulated in Appendix C are successively presented and discussed in the following section. Friction curves are drawn in Figure II-7 to Figure II-16 for each couple of temperature and contacting materials in the following order: steel/steel, steel/sapphire and WC/WC results.

II.4.2 Friction results with benzyl benzoate

In our experimental results (Figure II-7 to Figure II-16), all the friction curves exhibit a similar tendency. Three regimes can be distinguished, relatively to the SRR value:

- a linear region at very low SRR, where the friction coefficient increases linearly with SRR (viscous-like or linear response)
- a shear thinning-region at low-intermediate SRR, where the friction coefficient increases slowly with the SRR (elastic or shear thinning response)
- a plateau-like behaviour or (LSS regime) for some friction curves at higher SRR.

In all cases, no significant decrease of the friction coefficient, which characterizes the predominance of thermal effects, is observed. It is reminded that the tests were voluntarily limited to SRR= ±10% in order to limit shear heating. In the range of our operating conditions, benzyl benzoate exhibits friction coefficients lower than 0.08. Based on the LSS criterion defined in section II.3.2, the plateau-like behavior was found to appear in benzyl benzoate at Hertzian contact pressures equal or larger than 1.0, 1.1, 1.2 and 1.6 GPa at T=20, 40, 60 and 80°C respectively. In *Figure II-7* we showed that the LSS criterion was satisfied at 20°C when the Hertzian pressure reached 1.GPa.

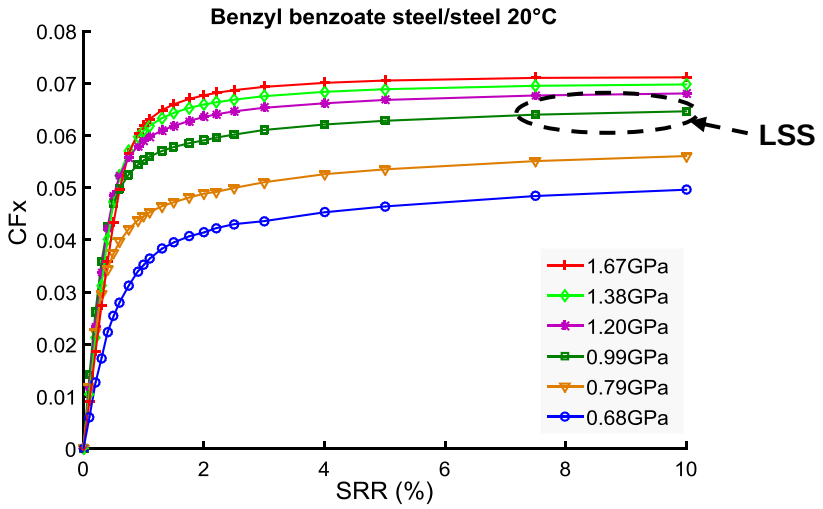

Figure II-7: Friction coefficient versus SRR, U_e=1.3m/s.

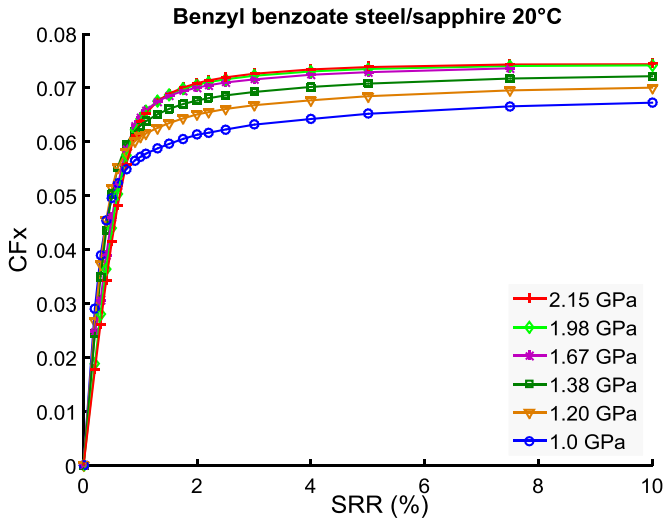

Figure II-8: Friction coefficient versus SRR, U_e=1.3m/s.

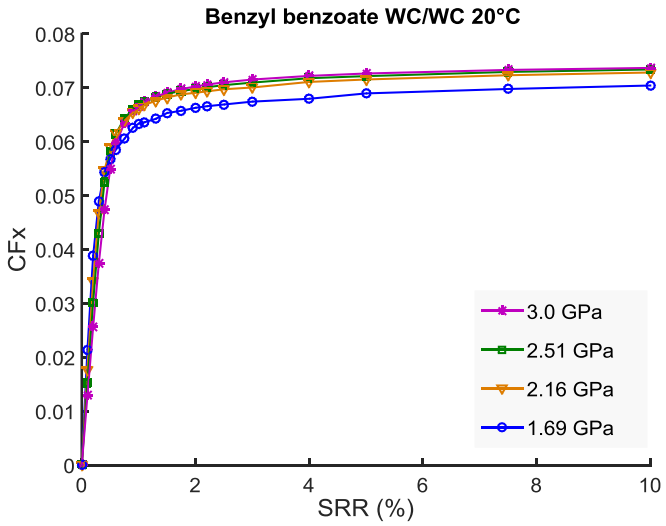

Figure II-9: Friction coefficient versus SRR, U_e=1.3m/s.

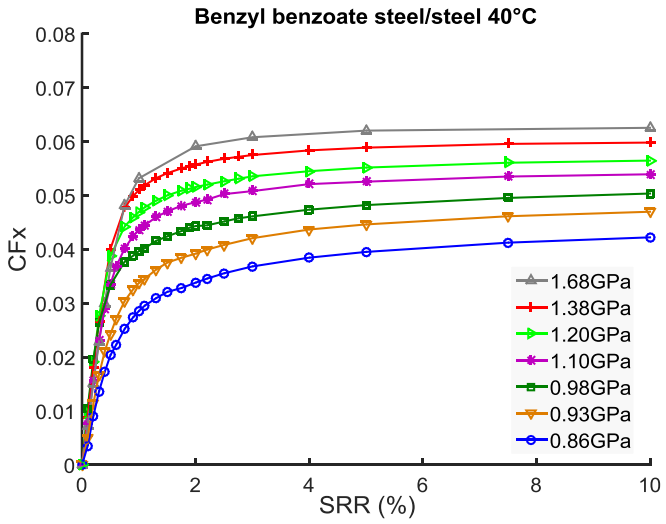

Figure II-10: Friction coefficient versus SRR, U_e=2.5m/s.

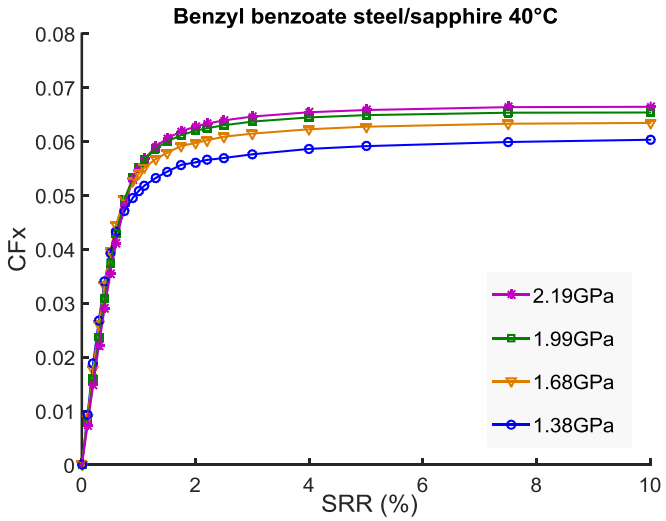

Figure II-11: Friction coefficient versus SRR, U_e=2.5m/s.

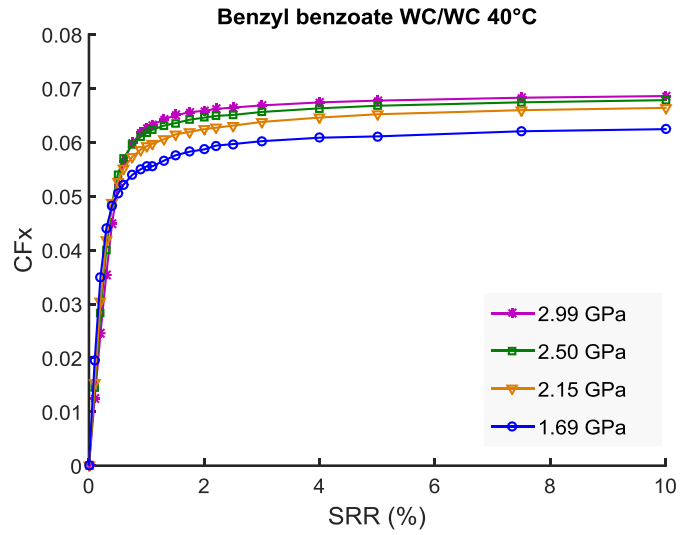

Figure II-12: Friction coefficient versus SRR, U_e=2.5m/s.

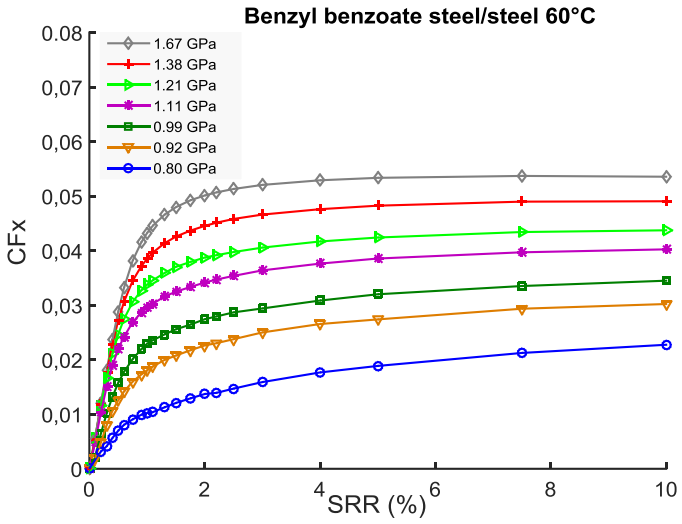

Figure II-13: Friction coefficient versus SRR, U_e=5m/s.

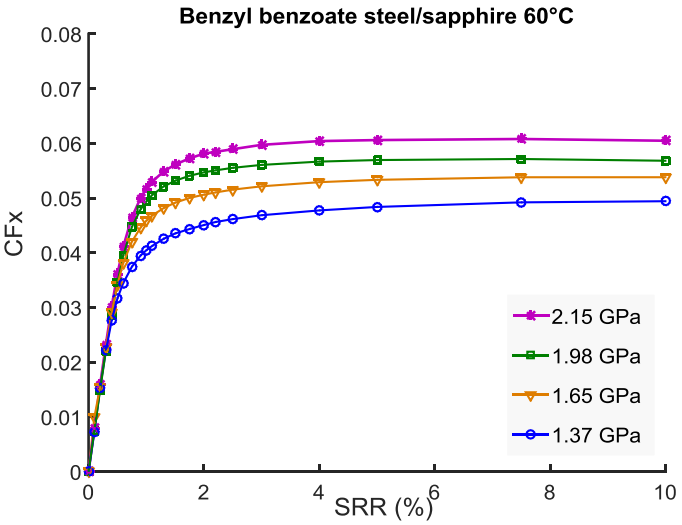

Figure II-14: Friction coefficient versus SRR, U_e=5m/s.

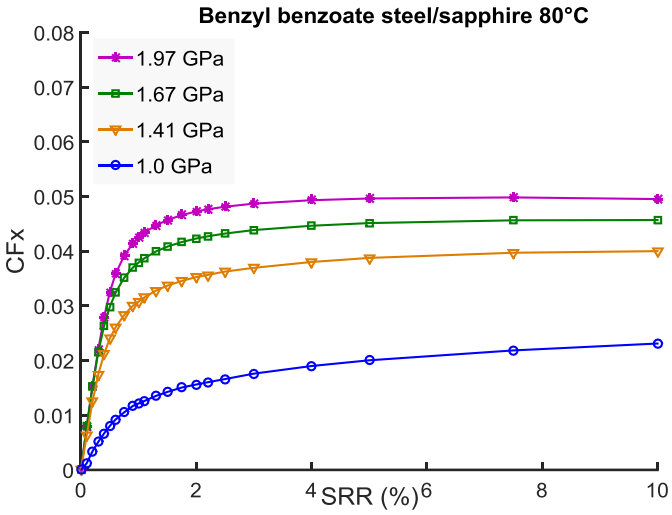

Figure II-15: Friction coefficient versus SRR, U_e=6.5m/s.

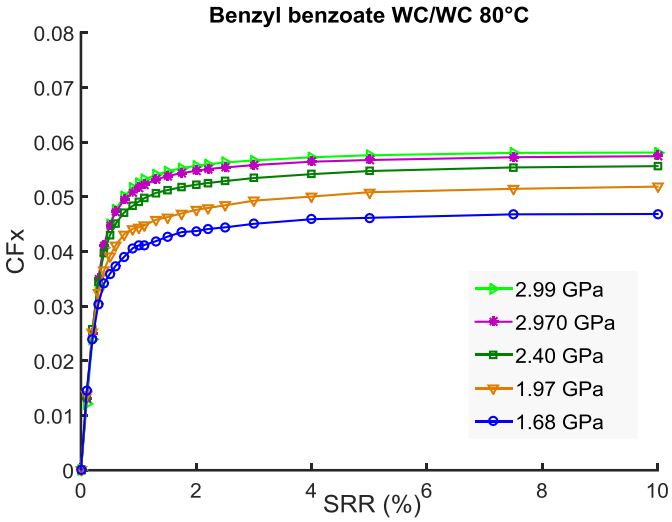

Figure II-16: Friction coefficient versus SRR, U_e=6.5m/s.

II.4.3 Limiting shear stress modelling variations with pressure and temperature

Once it has been shown that no thermal effect is observed in the friction measurements, the temperature and pressure dependence of LSS can be investigated. LSS values for benzyl benzoate have been derived from friction curves potted in Figure II-7 to Figure II-16, according to the stability criterion defined in section II.3.2. All the LSS data were calculated by using equation (I-11).

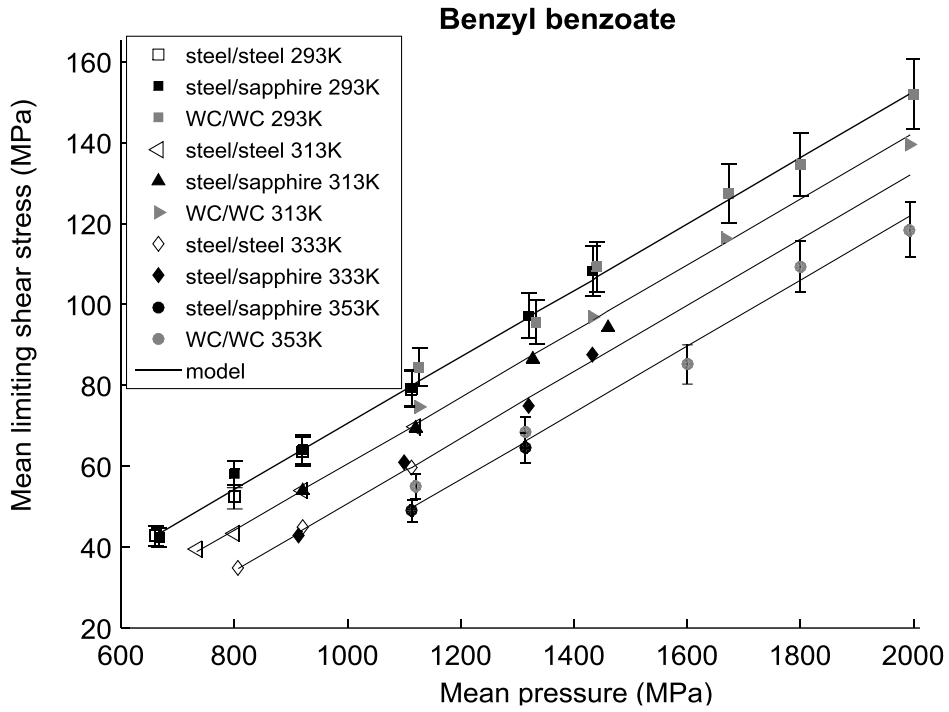

Figure II-17: Pressure and temperature dependence of the mean limiting shear stress of benzyl benzoate.

These data are gathered on Figure II-17 where the mean LSS variation is plotted as a function of the mean contact pressure ($\bar{P} = 2/3P_{Hertz}$) and temperature are plotted. For the clarity of the curve, the 95% confidence intervals of ± 5.6% (i.e. equal to two times the relative standard deviation indicated in section 2.2) are only plotted for the temperatures of 20 and 80°C.

First of all, an overlap between LSS values obtained from different contacting materials (steel, sapphire and tungsten carbide) is observed, which means that there is no at least significant influence of the nature of the contacting materials on the LSS, on the range of experimental conditions investigated here. LSS is found to be linearly dependent on both pressure and temperature: it increases with increasing pressure and decreases with increasing temperature. A search for an optimal regression led to the following relationships:

$$\overline{\tau_L} = \gamma\bar{P} - \beta T \qquad \text{(II-21)}$$

where temperatures are in degrees Celsius and

$$\overline{\tau_L} = \gamma\bar{P} - \beta T + \tau_{L0} \qquad \text{(II-22)}$$

where temperatures are in Kelvin, with $\tau_{L0} = \beta \times 273.15$.

γ , and β are the pressure and temperature LSS coefficients, respectively.

The model parameters are given in Table II-4 with a coefficient of correlation $R^2 = 0.995$.

γ	β (MPa/°C)
0.081	0.5025

Table II-4: Model parameters derived from experiments up to 3GPa.

These coefficients are constant whatever the contacting surfaces (steel/steel, steel/sapphire or WC/WC), the pressure and the temperature chosen. Contrary to the previous models from literature [29], [41], our experimental results show no coupling between pressure and temperature, within the experimental domains studied in this work. As far as we know, it is the first time that such a bilinear model is derived from a large experimental set of data. In general, the LSS models from literature arise from disc machine tests performed at high speed and high SRR [29] with $\phi_T < 0.96$ which might induce a temperature rise in the lubricating film. Based on our experimental results, we believe that the lubricant heating might be responsible for the supplementary coupling term in the LSS models encountered in literature. The advantage of equation (II-22) is that pressure and temperature influences appear uncoupled, thus mechanical and thermal contributions to the LSS are separated. Furthermore, such a model could allow to extrapolate the LSS of a known lubricant on a wide range of pressure and temperature. However, it needs first to be validated on at least another lubricant of different chemical nature.

II.4.4 Validation on T9 lubricating oil

In the following part, the frictional behavior of a turbine mineral oil T9 is characterized in order to validate the experimental method described previously for benzyl benzoate, as well as to confirm the findings on the LSS variations with pressure and temperature.

II.4.4.1 Operating conditions

The operating conditions have been designed to minimize the lubricant heating, by taking into account the results presented in section II.3.3.1. The experiments were carried out at 20, 40, and 80°C, with U_e = 0.5, 1.3, and 6.5 m/s, respectively. Steel/steel, steel/sapphire and WC/WC contacts were studied, except at 80 °C where only steel/sapphire and WC/WC contacts were analysed. The film thickness was comparable to those obtained with benzyl benzoate. The applied SRR was extended to ±20% in order to reach the stability criterion defined in section II.3.2. The experimental conditions are summarized in Appendix D. For all tested conditions the thickness thermal reduction coefficient φ_T was higher than 0.97.

II.4.4.2 Experimental results with T9

The pressure and temperature dependence of LSS of the turbine mineral oil was then investigated, to confirm the bilinear evolution of the LSS obtained with benzyl benzoate. The

friction results are summarized in Figure II-18 to Figure II-26. For each temperature, the results are presented as follows: steel/steel, steel/sapphire and WC/WC contacts. It can be noted that the friction curves exhibit similar trends as those obtained with benzyl benzoate, namely: a linear region at very low SRR, a shear-thinning region followed by a plateau-like behavior for the highest pressures. For friction curves in which there is a decrease of the friction coefficient, the LSS was calculated just before the fall of the latter. Contrary to benzyl benzoate where the LSS occurs at SRR ≈10%, for the turbine mineral oil the LSS is reached for SRR ≈ 15%. However, it produces significantly higher friction coefficients (by 40% typically) compared to the benzyl benzoate. Moreover, the friction coefficient of T9 increases more gradually with SRR than that of benzyl benzoate. The LSS was found to appear in T9 at Hertzian contact pressures equal or larger than 0.95, 1.0 and 1.41 GPa at T=20, 40 and 80°C, respectively.

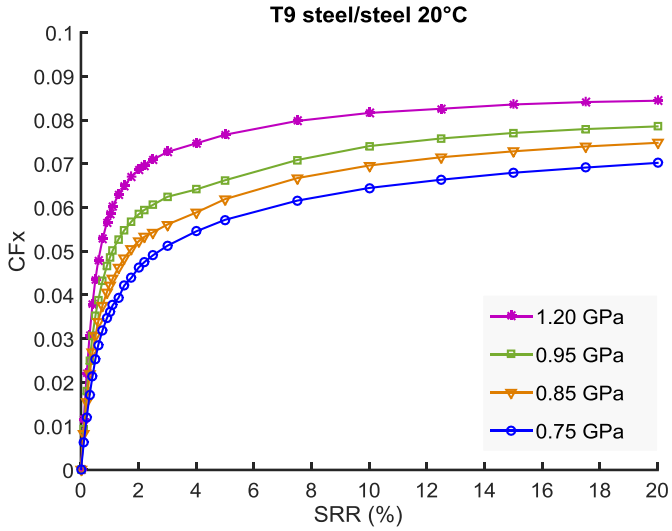

Figure II-18: Friction coefficient versus SRR, U_e=0.5m/s.

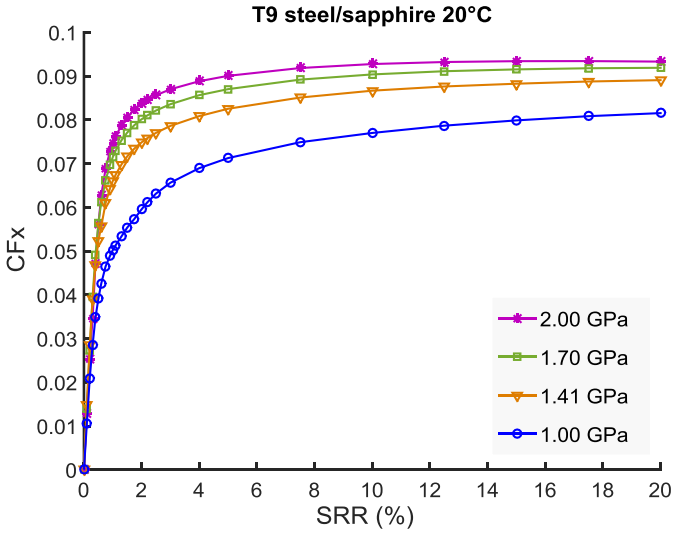

Figure II-19: Friction coefficient versus SRR, U_e=0.5m/s.

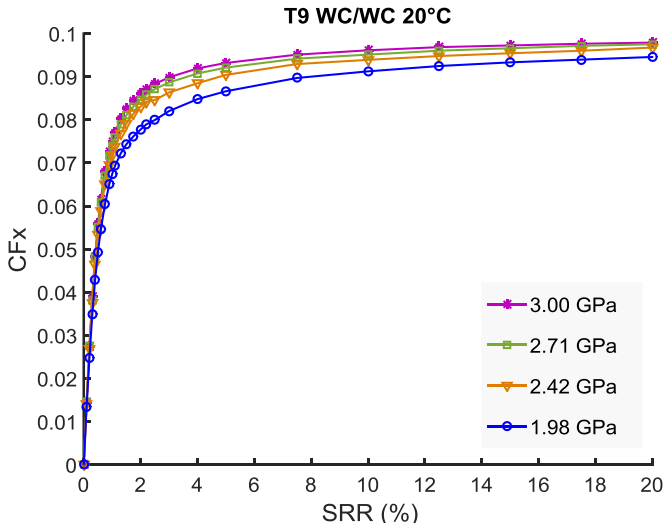

Figure II-20: Friction coefficient versus SRR, U_e=0.5m/s.

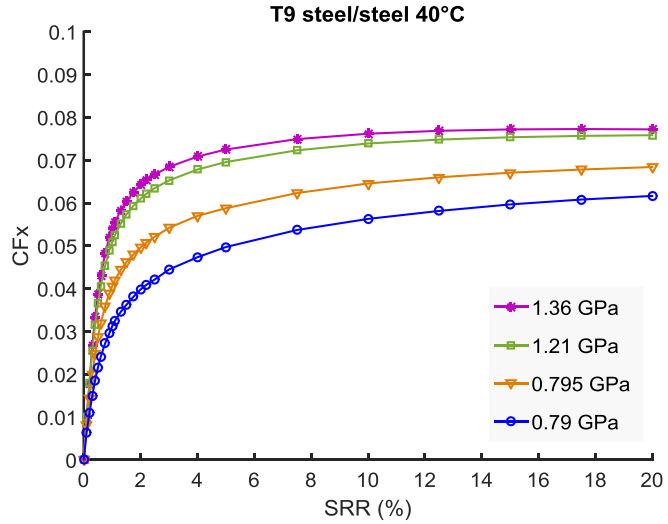

Figure II-21: Friction coefficient versus SRR, U_e=1.3m/s.

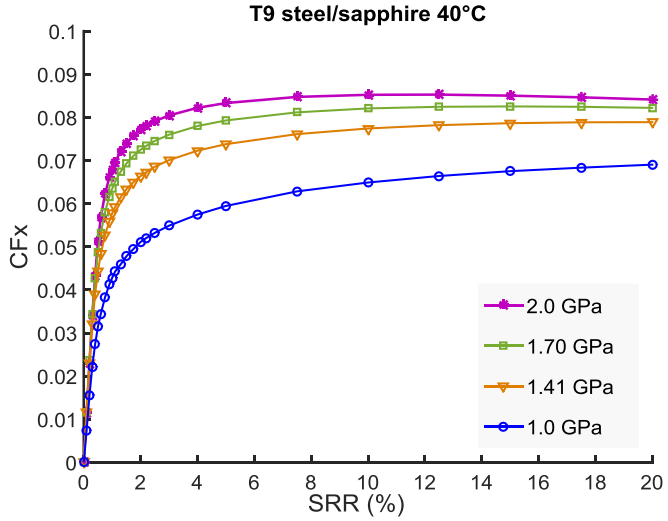

Figure II-22: Friction coefficient versus SRR, U_e=1.3m/s.

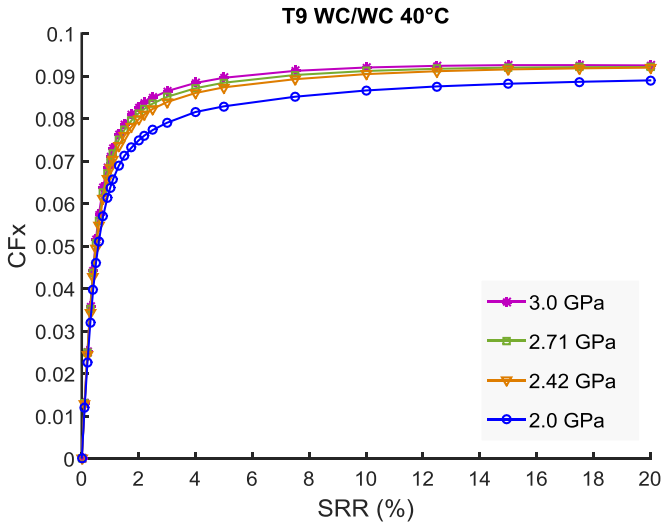

Figure II-23: Friction coefficient versus SRR, U_e=1.3m/s.

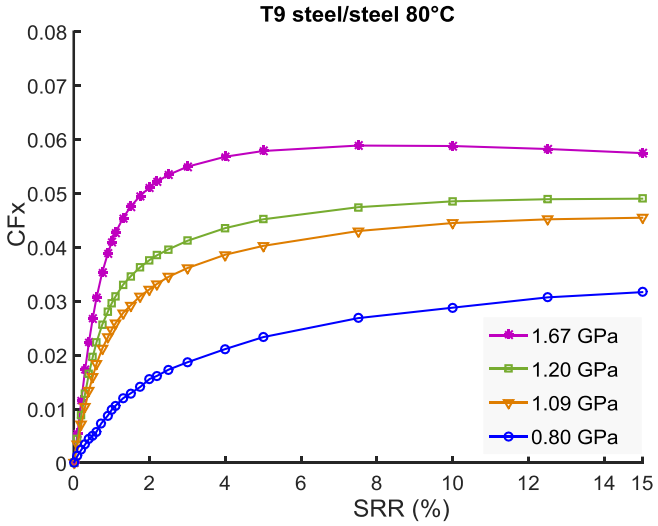

Figure II-24: Friction coefficient versus SRR, U_e=6.5m/s.

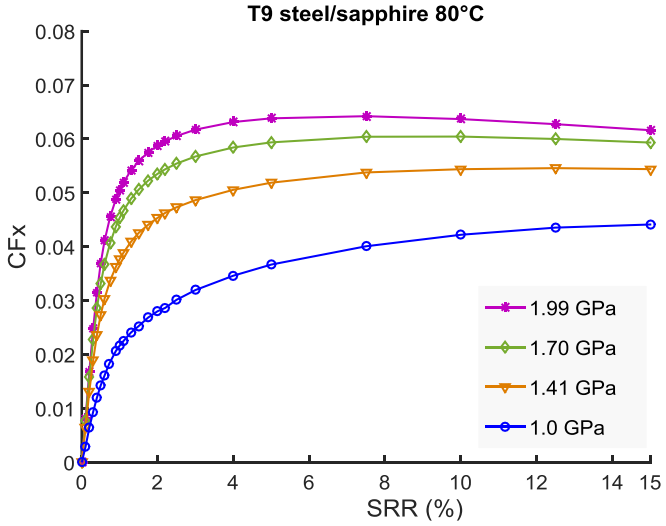

Figure II-25: Friction coefficient versus SRR, U_e=6.5m/s.

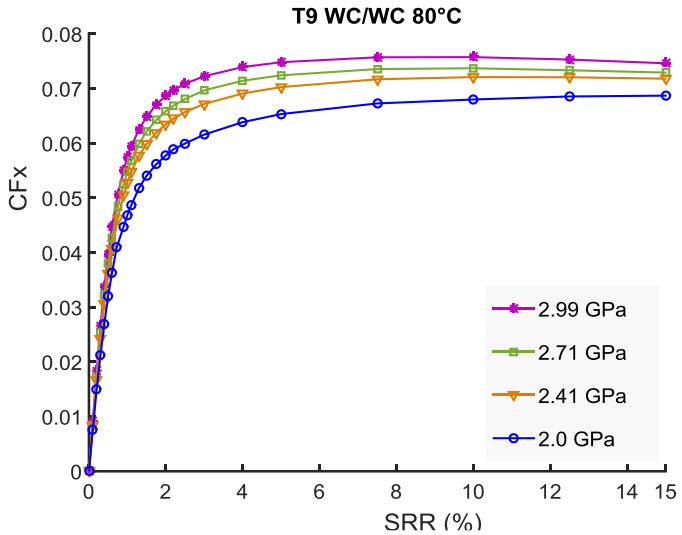

Figure II-26: Friction coefficient versus SRR, U_e=6.5m/s.

II.4.4.2.1 Temperature and pressure dependence of LSS

LSS for the turbine mineral oil has been determined from each friction curves as for benzyl benzoate when the LSS criterion previously defined was satisfied. The experiments covered a wide range of pressure, up to 3GPa. It was found that the LSS of the turbine mineral oil is reached at SRR higher than those found for benzyl benzoate (the SRR was extended up to ±20%). Then, the relationship between LSS, temperature and pressure was investigated. The results are summarized in Figure II-27. The mean LSS is plotted as function of the mean pressure for each applied temperature. For the clarity of the curve, the 95% confidence intervals of ± 5.6% are only plotted for the temperature of 80°C. A similar trend than the one obtained with benzyl benzoate is observed for the T9 mineral oil, with an overlap of the mean LSS measured on different materials, and an uncoupled evolution of the mean LSS relatively to pressure and temperature. The LSS varies linearly with pressure and temperature following eq. (II-22): a linear regression with a correlation of coefficient R^2 = 0.989 led to γ and β values given in Table II-5. It can be noted that these coefficients are higher than those obtained for benzyl benzoate.

γ	β (MPa/°C)
0.103	0.5956

Table II-5: Model parameters derived from experiments up to 3GPa.

This result obtained in a pressure range up to 3GPa confirms, for another lubricant of different molecular nature than benzyl benzoate, the suitability of equation II-21 and the absence of coupled effect between pressure and temperature. The independence of the nature of the contacting materials is validated as well. The pressure factor, γ, is in the same range of values that the one mentioned in the introduction. Indeed, LSS-pressure coefficient of mineral and synthetic oils ranges from 0.05 to 0.1 [92].

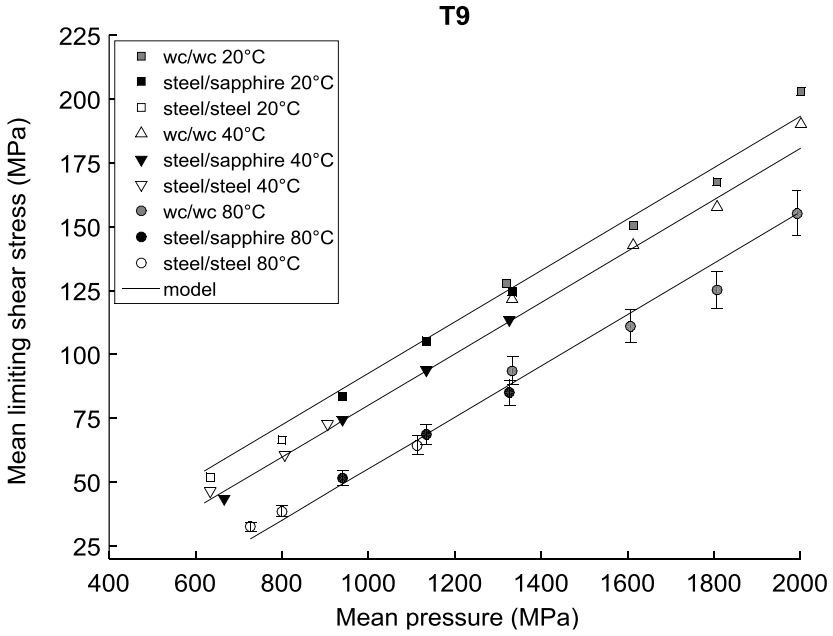

Figure II-27: Pressure and temperature dependence of LSS for T9

II.5 Summary

In summary, the frictional behavior of an organic compound, benzyl benzoate and a turbine mineral oil, was characterized in a wide range of pressure (0.68-3 GPa) and temperature (20-80°C) with a ball-on-disc tribometer.

First of all, a series of experiments has been performed on both lubricants in order to highlight the influence of shear heating on friction measurements. These experimental results allowed us to optimize the operating conditions of the friction measurements relatively to the lubricant shear heating with the aim to characterize the limiting shear stress whenever the LSS criterion was satisfied.

Then, the pressure and temperature dependence of LSS for both lubricants was studied. Surprisingly, a simple bilinear dependence of the LSS with pressure and temperature was found in both cases. This means that pressure and temperature appear uncoupled unlikely to models encountered in literature: it was suggested that the coupling term between pressure and temperature might be due to the thermal heating effects. We also demonstrated that there

was no influence of the contacting materials on the limiting shear stress and that the limiting shear stress-pressure and the limiting shear stress-temperature coefficient are intrinsic specific to each fluid.

In the third chapter we focus on one of the scenarios from literature: the lubricant glass transition, and we investigate the influence of high pressure on the lubricant state. This chapter is divided into two sections. The first one focuses on the linear friction regime restrained at very low SRR (≈ 0.3%). The effective viscosity dependence with pressure is studied and compared to the glass transition pressure of the lubricant derived from the modified WLF model [42].

In the second section, we investigate experimentally the glass transition pressure by using Raman and Brillouin spectroscopy in order to validate the different conclusions made in the first section.

III Towards a characterisation of the lubricant state

III.1 Introduction

In the previous chapter we proposed a new model to establish the temperature and pressure dependence of the limiting shear stress of lubricants under highly loaded conditions. This model was derived from a series of friction measurements (up to 3GPa) performed on a pure diester fluid (benzyl benzoate), and validated on a commercial turbine mineral oil (Shell T9). This chapter now aims to improve the understanding of the behavior of lubricants under such extreme shear and pressure conditions. This will lead to a better understanding of the physical origin of the limiting shear stress.

The explanation of friction curves in term of the shear properties of the lubricating fluids has been the subject of many studies. Harrison & Trachman [93] suggested that under high pressure and high rolling speed the oil remains a newtonian liquid in its response to small shear rates. For higher shear rates, Crook [57] and Dyson [62] explain the non-linear regime in terms of viscoelastic behavior of the lubricant. Finally, for the highest shear rates, some authors suggest that the lubricant behaves like an elastic solid. However, the behavior of the lubricant under extreme shear and pressure conditions is not well understood. But, it is generally accepted that when the sliding velocity is small enough to avoid viscous heating and shear thinning, a mean effective viscosity can be derived from the slope of the linear friction regime [30, 43]. It is based on the assumption that the friction is developed uniformly over the whole Hertzian area.

On the other hand, the past 60 years have witnessed a growing research effort in developing spectroscopy techniques adapted to the EHD contact problem. Raman and Brillouin scattering could provide information about the physico-chemical characteristic of the lubricant: they are essential to better understand the processes which are controlling the macroscopic properties such as viscosity. In the previous chapter, we established the temperature and pressure dependence of the LSS of lubricants under highly loaded conditions. However, the answer to the physical origin of the LSS involve an understanding of the lubricant behavior at molecular-scale.

This chapter is divided into two sections: the first one deals with macroscopic behavior of the lubricant in a highly loaded contact. The transition from a solid-like to a viscous-like behavior of the lubricant is estimated from the modified WLF viscosity model and compared to its effective behavior derived from friction measurements. The second section investigates the lubricant behavior at microscale through measurements such as Raman and Brillouin spectroscopy. Results obtained at both scales are compared to relate the physical behavior of the lubricant and its macroscopic consequences on friction.

III.2 Characterisation of the lubricant “solid-like” behavior at macroscopic scale

According to Johnson and Cameron [43] a mean effective viscosity can be deduced in the linear region of the friction curve, given by the following expression:

$$\bar{\eta} = \frac{\bar{\tau}}{\dot{\gamma}} = \frac{F_X}{S}\frac{h_c}{\Delta U} \qquad \text{(III-23)}$$

where $\bar{\tau}$ is the mean shear stress, S the contact area and ΔU the sliding velocity. It must be noted that this expression (III-23) was derived from friction measurements performed on rolling-contact disc machine in which the elastic compliance of the contacting disc was neglected. However, when the film is thin and stiff the compliance of the contacting materials may not be negligible. At high pressure, the linear region of the friction may be influenced by the elastic deformation of the contacting solids. Using a two disc machine, Hirst [30] and al. demonstrated that the elastic compliance of the discs may be comparable or exceed that in lubricant film and must be taken into account in the calculation of shear modulus of the lubricants. Previous studies [56] showed that the elastic deformations of the solids may play a significant role at very low shear rate. On the other hand, the influence of elastic deformations becomes less important in the non-linear regime and can be neglected. Thus, to derive an effective viscosity from friction measurements according to expression III-23, the elastic compliance of the surfaces must first be verified to be negligible relatively to the lubricant shear deformation.

The effective viscosity variations (shell Turbo 33) with contact pressure and rolling speed have already been investigated by Johnson and Cameron [43] in EHD contact by using a disc machine. They found that, at moderate pressures (contact pressure up to 1.8 GPa), the effective viscosity increases approximately exponentially with pressure up to a critical pressure. The effective viscosity values they measured were consistent with low-pressure measurements made with a falling-plunger viscometer. However, beyond a critical pressure of order of 0.7 GPa, a change of the viscosity evolution with pressure occurs and the effective viscosity becomes almost constant. According to them, this effective viscosity evolution could be attributed to a possible sudden change in the properties of the fluid at high pressure. This matches with a major assumption quoted in literature, and mentioned in the first chapter, which explains the onset of the LSS by the glassy state of the lubricant [26]. It must here be noted here that, as stated earlier, the effective viscosity derived from the linear friction regime was based on a Newtonian behavior of the lubricant. However, a linear elastic solid film would also result in a linear friction curve at small sliding speed [81] and would also enable to derive an

effective viscosity. The intermediate case of the transition between liquid-like and solid-like behavior is more complex as both phases should coexist within the contact area.

Our analysis of the experimental results can be summarized in two steps: first of all we ensure that the influence of the contacting materials on the effective properties of the lubricant can be neglected in our friction measurements. Then we focus on the linear friction regime characteristic of the lubricant behavior in a contact. Indeed, the slope of the linear friction regime may provide information on the lubricant state in the contact as "solid-like" behavior. This latter is believed to be responsible of the limiting shear stress.

III.2.1 Lubricant glass transition pressure from the modified WLF Yasutomi model

To predict the lubricant viscosity in extended domains of pressure and temperature comparable to the operating conditions tested, WLF model was used [42]. This model is presented in Appendix A and Appendix B for both benzyl benzoate ant T9. In the WLF model, the glass transition temperature of the fluid T_g is considered as the reference temperature. The fluid viscosity is written as follows:

$$\mu\,(P,T) = \mu_g . 10^{\frac{-C_1.\left(T-T_g(P)\right).F\,(P)}{C_2+\left(T-T_g(P)\right).F\,(P)}}$$

With : (III-24)

$$T_g(P) = T_g(0) + A_1 \ln(1 + A_2 P)$$

$$F(P) = 1 - B_1 \ln(1 + B_2 P)$$

The function $T_g(P)$ represents the variation of the glass transition temperature with pressure based on experimental data and $F\,(P)$ represents the variation of the thermal expansion coefficient with pressure. This model led to a good adjustment of the experimental data. Physically, the WLF model can be justified by means of the free volume concept, which is the volume available within the fluid allowing the transfer of molecules accompanying the flow. When the free volume tends to zero, the mobility of the molecules decreases and the fluid viscosity tends to infinity. It is commonly assumed in literature that the glass transition of a fluid occurs when its viscosity reaches a value of 10^{12}Pa.s. The experimental domains of pressure and temperature are limited to 0-700 MPa and 20-130°C. However the good agreement obtained between experimental data and WLF predictions gave credit to extend the model validity to higher pressures. But the WLF prediction remains limited because it is based on the assumption that the lubricant viscosity in the glassy state reaches a value of 10^{12}Pa.s.

Thus this model was used to derive glass transition pressures of both benzyl benzoate and T9 mineral oil. Data are gathered on Table III-1 and Table III-2, for the temperatures

experimentally investigated. They should provide an order of magnitude of the pressure and temperature conditions from which the lubricant experiences a transition towards a solid-like behavior.

In the following section the pressure dependence the effective viscosity is presented.

T(°C)	P_g (GPa)
20	0.80
40	0.98
60	1.17

Table III-1: Glass transition pressure of benzyl benzoate derived from the modified WLF for the three temperature tested.

T(°C)	P_g (GPa)
20	1.12
40	1.46
80	2.24

Table III-2: Glass transition pressure of T9 derived from the modified WLF model for the three temperature tested.

III.2.2 Elastic deformation of the contacting surfaces

In the following, the approach of Bair and Kotzalas [56] is chosen to estimate the elastic contribution of the solid bodies and to correct, if needed, the friction coefficient in the linear regime. The slope of the linear friction regime may allow us to have information on the lubricant state in the contact as a “solid-like” behavior. This latter is believed to be responsible of the limiting shear stress. The idea followed by Bair and Kotzalas [56] lies in comparing the linear traction gradient of both solid bodies and lubricant, to estimate whether the elastic deformation of the solid bodies themselves is likely to influence the friction coefficient evolution at low SRR.

In a dry contact, the theoretical linear traction gradient due to solid bodies compliance (equivalent of the slope of the traction curve due to the solid bodies elasticity in the absence of fluid) is given by:

$$r_s = 1.78\, {}^{G}/_{P_{Hertz}} \tag{III-25}$$

where G is the shear modulus of the solid bodies. It is derived from their elastic modulus and their Poisson coefficient.

$$G = \frac{E}{2(1+\nu)} \tag{III-26}$$

In case of steel/sapphire contacts, equivalent shear modulus G_{eq} and Poisson ratio are calculated from Kalker [94].

$$G_{eq} = {}^{2}\Big/\left(\frac{1}{G_1} + \frac{1}{G_2}\right) \quad \text{(III-27)}$$

$$\nu_{eq} = \frac{G}{2}\left(\frac{\nu_1}{G_1} + \frac{\nu_2}{G_2}\right) \quad \text{(III-28)}$$

For a lubricated contact, the fluid Newtonian traction gradient is:

$$r_f = {}^{\eta U_e}\Big/_{h_c \bar{P}} \quad \text{(III-29)}$$

with η the viscosity calculated from the linear region of the friction curve

Then the compliance of the solids and the fluid is derived as the inverse of their traction gradients. It is representative of the ability of a material to be deformed. A low solid to fluid compliance ratio ${}^{r_s}/_{r_f}$ means that deformations concentrate in the fluid and that the contribution of the contacting surfaces in the linear region of the friction curve can be neglected. This ratio has been calculated for all operating conditions described in the previous chapter. It ranges from 0.8 to 10.7% for benzyl benzoate and from 0.7 to13.3% for the mineral oil T9. Conditions leading to the highest ratio ${}^{r_s}/_{r_f}$ in the case of steel/steel contacts are given in Table III-3 and *Table III-4*.

Steel/steel			
Temperature (°C)	20	40	60
Pressure (GPa)	*1.67*	*1.68*	*1.67*
Viscosity (Pa.s)	782.43	306.70	85.95
h_c *(m)*	9.92E-08	9.06E-08	8.97E-08
U_e *(m/s)*	1.3	2.5	5
$\bar{P}$ *(Pa)*	1.12E+09	1.12E+09	1.12E+09
Fluid compliance	0.109	0.132	0.168
Solid compliance	0.012	0.012	0.012
${}^{r_s}/_{r_f}$*(%)*	10.7	8.8	6.9

Table III-3: Benzyl benzoate operating conditions leading to the highest ratio ${}^{r_s}/_{r_f}$.

Steel/steel			
Temperature (°C)	20	40	80
Pressure (GPa)	*1.20*	*1.36*	*1.67*
Viscosity (Pa.s)	1882.14	659.51	122.80
h_c *(m)*	1.11E-07	1.06E-07	1.26E-07
U_e *(m/s)*	0.5	1.3	6.5
$\bar{P}$ *(Pa)*	8.02E+08	9.06E+08	1.11E+09
Fluid compliance	0.094	0.112	0.175
Solid compliance	0.008	0.009	0.012
${}^{r_s}/_{r_f}$*(%)*	8.9	8.5	6.6

Table III-4: T9 operating conditions leading to the highest ratio ${}^{r_s}/_{r_f}$.

It can be noticed on Table III-3 and Table III-4 that the highest ratios $^{r_s}/_{r_f}$ for all the experimental conditions is still well below 1. So that the contribution of the elastic deformation in the first linear regime of the friction curve relatively to SRR can be neglected. This linear regime can be attributed to the lubricant response. This allows to deduce an effective viscosity from the slope of the friction curve at the origin which will be detailed in the following section.

III.2.3 Effective viscosity pressure dependence

The first linear regime of each measured friction curve exhibits a constant slope which is representative of the lubricant behavior, as verified in the previous section. By estimating the lubricant film thickness thanks to an empirical film thickness expression and by converting the friction data in terms of shear stress versus shear rate, the constant slope becomes homogeneous to an effective viscosity.

Even if no absolute information can be extrated from this macroscopic parameter, its evolution can be characteristic of the different regimes experienced by the lubricant in the whole contact. To convert friction data into $(\tau, \dot{\gamma})$ charts, the following approached is applied. A simple Couette flow is assumed in whole the contact, with a constant film thickness.
In our experiments a circular contact is formed between a ball and flat disc, so the tangential force F_X can be calculated by integrating the shear stress τ over the circular contact area:

$$F_X = \int_{r=0}^{r=a_{Hertz}} \tau(r) 2\pi r dr \qquad \text{(III-30)}$$

where a_{Hertz} is the Hertzian contact radius.

The shear stress in a Couette flow is given by:

$$\tau = \frac{\eta_{eff} \Delta U}{h_c} \qquad \text{(III-31)}$$

with U_S the shearing velocity, and h_c the central film thickness and η_{eff}, the effective viscosity.

$$\Delta U = U_{ball} - U_{disc} = U_e . SRR \qquad \text{(III-32)}$$

Substituting equation (III-31) into equation (III-30) leads to:

$$F_X = \pi \, a_{Hertz}^2 \, \eta_{eff} \, \frac{\Delta U}{h_c} \qquad \text{(III-33)}$$

The friction coefficient is given by:

$$CF_X = \frac{F_X}{F_Z} = \pi a_{Hertz}^2 \eta_{eff} \frac{U_e SRR}{h_c F_Z} \qquad \text{(III-34)}$$

$$\text{or : } CF_X = C.\eta_{eff}.SRR \tag{III-35}$$

with $C.\eta_{eff}$ the slope of the friction curve at the origin and C a prefactor which writes:

$$C = \pi.2^{(-a+\frac{2}{3})} U_e^{1/3} \eta_0^{-a} \alpha^{*-c} R_{eq}^{(a+2b-\frac{1}{3})} K_{HD}^{-1} \Big/ E_{eq}^{(c+\frac{2}{3}-a-b)} \tag{III-36}$$

with $a = 0.067$, $b = -0.067$ and $c = 0.53$.

η_0 is the viscosity at ambient pressure and given temperature, α^* the piezo-viscosity coefficient. C depends on the lubricant nature and temperature, the contacting materials, the normal force and the entrainment velocity. So, for a given set of operating conditions C is a constant. It can also be noted that, by varying only the normal force, the friction coefficient can be written as:

$$CF_X = C'.{F_Z}^{-(b+\frac{1}{3})}.\eta_{eff}.SRR \tag{III-37}$$

with C' a constant.

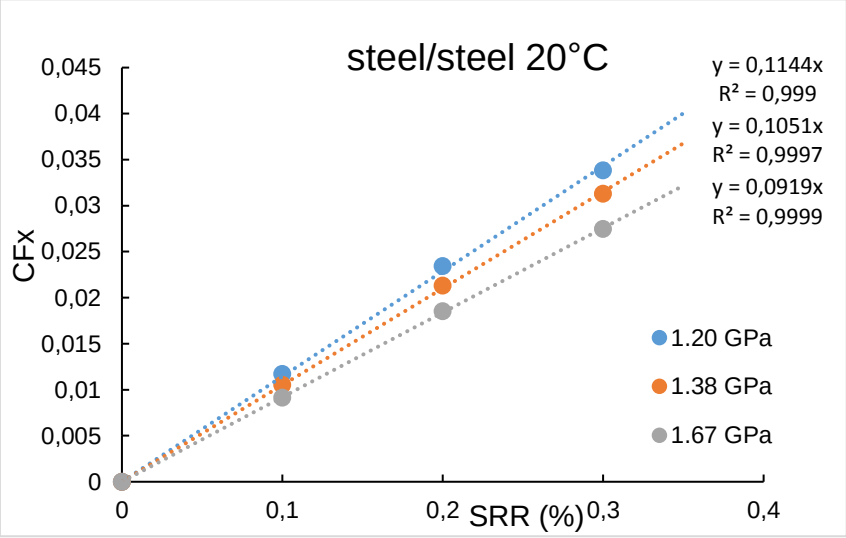

Figure III-1: Linear friction domain where the slope at the origin of the friction coefficient is determined for benzyl benzoate.

The slope at the origin is determined for each friction curve by fitting the linear region, limited to SRR 0.03%, as shown in *Figure III-1*. For all experimental results, the effective viscosity of the lubricant is presented in the following part.

- **Benzyl benzoate**

In Figure III-2 we plot in log scale the effective viscosity of benzyl benzoate, versus the Hertzian pressure for the three different temperatures. For each applied temperature, we have reported

the glass transition pressure estimated by the modified WLF-Yasutomi model. The blue vertical dashed line indicates the glass transition pressure extrapolated from the WLF model at 20°C, the green at 40°C and the red at 60°C. These values must be considered as an order of magnitude, that's why in the next section spectroscopic measurements were performed to determine more precisely the glass transition pressure of the lubricant.

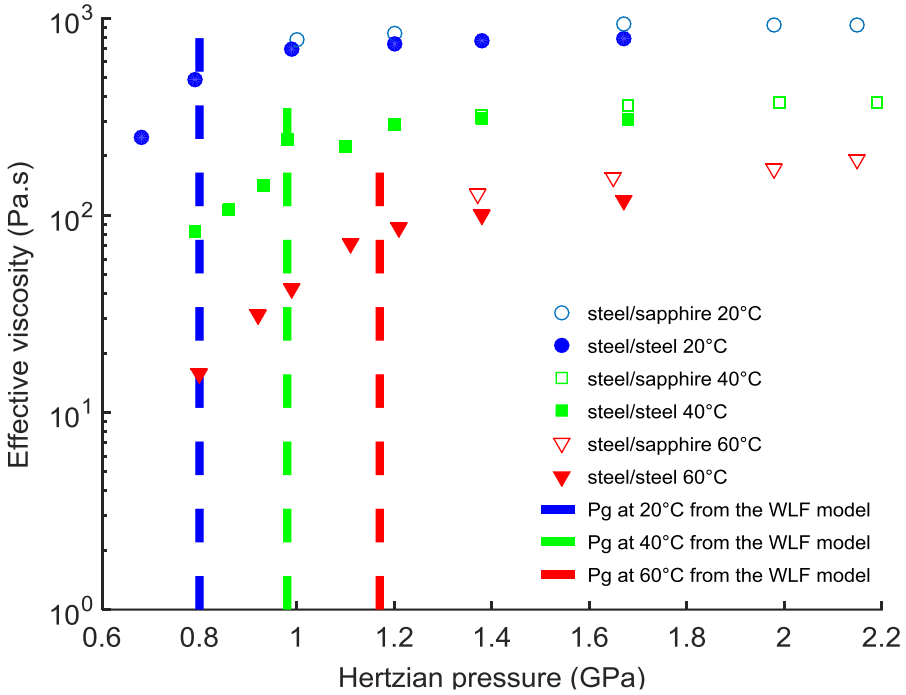

Figure III-2: Benzyl benzoate effective viscosity as a function of the Hertzian pressures at 3 temperatures.

We observe that for each temperature, two regions can be distinguished: an exponential variation of the effective viscosity (corresponding to the linear part of the curve) until a critical value of pressure, from which the effective viscosity becomes almost independent of the Hertzian pressure. It can be noted from Figure III-2 that the critical pressure roughly corresponds to the glass transition pressure given by WLF model. This suggests a transition from a liquid-like to a solid-like behavior might be responsible for the two distinct tendencies followed by the effective viscosity. The effective viscosity of the lubricant increases exponentially with pressure for P lower than P_g,which may be associated with a viscous-like behavior of the lubricant. Then for P higher than P_g , the lubricant effective viscosity remains almost constant, which can be associated with an elastic or solid-like behavior of the lubricant. This is in accordance with the experimental results obtained by Johnson and Cameron [43].

To investigate the influence of the lubricant temperature, we rescale the effective viscosity and the Hertzian pressure for the three temperatures. Pressure is rescaled with the glass transition

pressure at a given temperature, and effective viscosity is normalized by the viscosity plateau value for each temperature. Results are plotted on *Figure III-3*. The vertical dashed line stands for the Hertzian pressure reaching the predicted glass transition pressure ($P_{Hertz} = P_g$).

The horizontal line delimits effective viscosities derived from friction curves satisfying or not the LSS stability criterion defined in the previous chapter.

First, *Figure III-3* clearly highlights the three regimes (the two asymptotic regimes and the transition regime) experienced by the lubricant. Low pressures correspond to the asymptotic regime of a Newtonian liquid-like lubricant in the whole contact area, with an effective viscosity exponentially increasing with pressure. High pressures correspond to the asymptotic regime of a solid-like lubricant in the whole contact area, with an effective viscosity independent of pressure.

Then, the three effective viscosity curves corresponding to the three different temperatures investigated perfectly overlap. It suggests that the transition between a liquid-like and a solid-like regime is only governed by the thermodynamic state of the material, ie by the combination of the pressure and temperature parameters.

Furthermore, it appears that the first asymptotic regime only concerns friction curves which do not satisfy the LSS stability criterion defined in chapter II. On the other hand, the second asymptotic regime only concerns friction curves satisfying this LSS stability criterion. This remark directly relates the glass transition of the lubricant and the macroscopic onset of LSS in a contact.

Figure III-3 enables to locate the onset of the lubricant effective viscosity transition. Indeed, this transition seems to trigger as soon as the maximum Hertzian pressure P_{Hertz} reaches the glass transition pressure P_g, and develops over a certain range of pressures before reaching the last asymptotic regime. It can be deduced that as soon as a (small) volume of the lubricating fluid in the contact is glassy, the macroscopic behavior of the lubricant diverges from a simple exponential pressure-viscosity law. Then, for higher pressures, this effective viscosity tends to reach a stable value as the volume of glassy fluid increases in the contact.

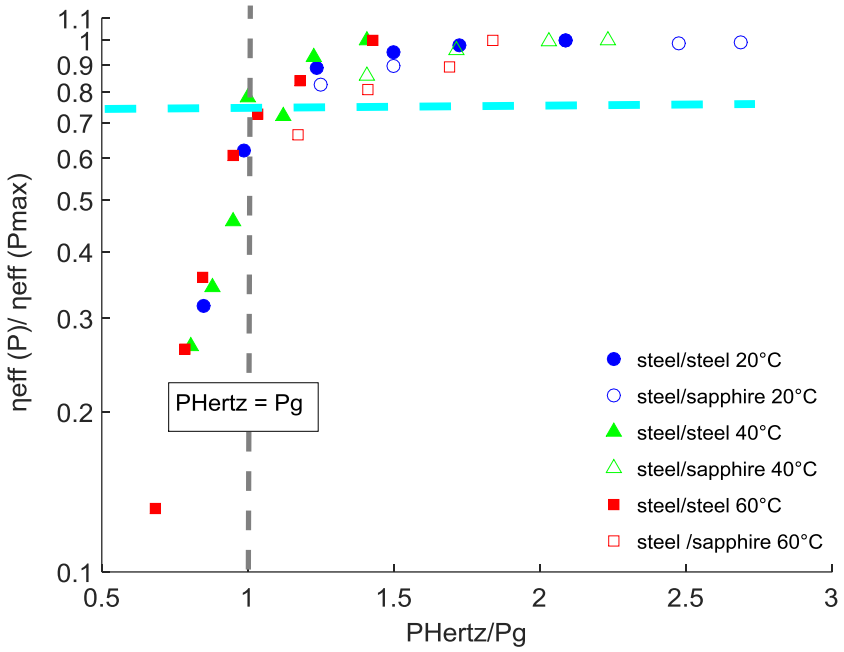

Figure III-3: The rescaled effective viscosity of benzyl benzoate as a function of the rescaled Hertzian pressure at 3 temperatures.

To investigate the range of pressures over which the transition develops, on *Figure III-4* results from *Figure III-3* have been plotted and two vertical lines have been added. The first one corresponds to a transition value of $\bar{P}/P_g = 1$ (or $P_{Hertz}/P_g = 3/2$), meaning that the mean pressure in the contact has reached the predicted glass transition pressure. The second one stands for a Hertzian pressure in the contact of twice the transition pressure: $P_{Hertz} = 2P_g$.

The first condition ($\bar{P} = P_g$) occurs slightly before the effective viscosity plateau. This corresponds, according to the Hertz theory of pressure distribution in a contact, to 56% of the contact submitted to a pressure above the transition pressure.

The second condition ($P_{Hertz} = 2P_g$) rises at the beginning of the effective velocity plateau, or at the very end of the effective viscosity transition. According to the distribution of pressure in a contact from the Hertz theory, this condition corresponds to 75% of the contact area above P_g. It is thus stated from Figure *Figure III-4* that the effective viscosity transition develops in a contact for maximum Hertzian pressures P_{Hertz} in the range of $[P_{Hertz} - 2P_g]$. In this range of pressures, the volume of lubricating fluid in glassy state extends from a very small volume (for $P_{Hertz} \sim P_g$) up to 75% of the contact area (for $P_{Hertz} \sim 2P_g$). Beyond, the effective viscosity, representative of the lubricating fluid state, is independent of the contact pressure.

Finally, the horizontal line on *Figure III-4* (which distinguishes friction tests satisfying or not the LSS stability criterion) indicates that during the friction tests performed in this work, a limiting shear stress was measured (almost) as soon as the Hertzian pressure exceeded the transition

pressure, so at the very beginning of the effective viscosity transition. Thus, it can be concluded that only a (very) small volume of lubricant in the glassy state is necessary to trigger LSS.

These conclusions are in line with the conclusions of Bair et al.[75], as reported in chapter I. Indeed, they showed that 1) shear bands develop when the lubricant is subjected to a pressure of order of its transition pressure, 2) the onset of the first shear band triggers the non-linear behavior of the lubricant.

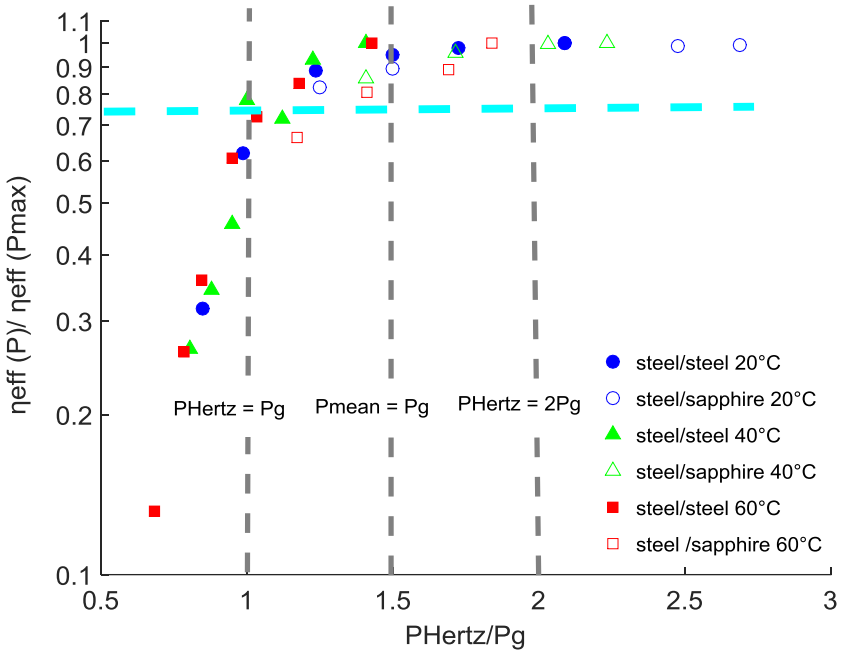

Figure III-4: The rescaled effective viscosityof benzyl benzoate as a function of the rescaled Hertzian pressure at 3 temperatures and the different pressures range.

- **Mineral oil, T9**

As mentioned above, the same experimental protocols as those developed for characterizing the benzyl benzoate are applied to the industrial mineral oil T9, in order to support and validate the different results obtained with the former. As in the case of the benzyl benzoate, first of all we investigated the contribution of the elastic deformations on the linear friction regime based on the Bair and Kotzalas [56]. This led to conclusion that the contribution of the elastic deformations can be neglected in the friction measurements with T9. In other words, the influence of the elastic deformation of solids in the linear friction regime can be neglected.

Then, the effective viscosity of the mineral oil T9 was derived from the linear regime of each experimental friction curve following the equation III-37. Data are gathered in Figure III-5, where effective viscosity is plotted as a function of Hertzian pressure. It shows here also an overlap between the different results from steel/steel, steel/sapphire and WC/WC measurement, meaning that the contacting materials have no influence on the effective viscosity evolution. The T9 effective viscosity variations with pressure exhibit similar trends as

those observed for benzyl benzoate. It increases exponentially below the glass transition pressure estimated by using WLF model and seems to be constant above the glass transition pressure. This confirms the dependence between the frictional response at low SRR and the LSS the lubricant.

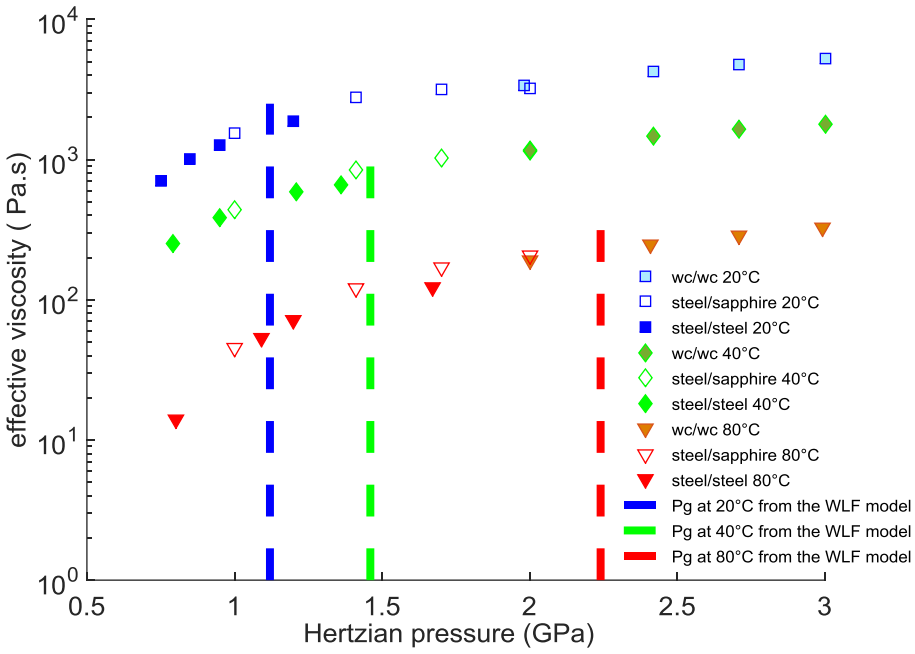

Figure III-5: T9 effective viscosity as a function of the Hertzian pressures at 3 temperatures.

The following section investigates the lubricant state at microscale with spectroscopic measurements such as Raman and Brillouin techniques.

III.3 Characterization of the lubricant behavior at the microstructure scale

The different scenarios proposed in literature to explain the occurrence of the LSS involve very small scales of the lubricant flow in a contact. Among them, the effective viscosities extrapolated from friction curves seem to highlight the influence of the glassy state of the lubricant. Unfortunately, major experimental limitations appear when probing fluid thicknesses lower than one micron and in situ measurements constitute a considerable technical and scientific challenge. Furthermore, an accurate control of the main parameters, P, T and $\dot{\gamma}$, governing the lubricant physical properties is necessary to analyse their influence on the LSS, which also requires a fine and fragile instrumentation.

In this context, vibrational spectroscopic approaches are of major interest as they are based on light/matter interaction. They are needed to improve our understanding of the processes which control the macroscopic properties of lubricants such as viscosity or density.

Several vibrational techniques are available, which refer to different interactions of electromagnetic radiations with matter. There are thus many forms of spectroscopy, each of them providing useful information to identify species composition and to determine various characteristics of their structure. Among them, we can quote infrared, Brillouin or Raman spectroscopy, based on slightly different physical principles. Infrared spectroscopy (IR) deals with the interaction of infrared radiation with matter, the spectrum is obtained by measuring the absorption of IR radiation, although infrared emission and reflection are also used. On the other hand, Brillouin and Raman techniques both investigate the inelastic light scattering interaction of light with molecular/atomic vibrations (phonons) to obtain information at respectively molecular and atomic scales. Brillouin light scattering (BLS) is commonly attributed to the generation of acoustic phonons by the sample at frequencies of several GHz, whereas Raman light scattering (RLS) is attributed to vibrational oscillations of optical phonons generated in the sample at frequencies of several THz.

RLS was discovered in 1928, and was already successfully used in a contact several decades ago [95–97] to obtain direct pressure measurements from an entrapped fluid at equilibrium after an impact and from dynamic EHD contacts, respectively.

On the other hand, the glass transition in lubricants under pressure has already been studied in literature by Brillouin light scattering. The frequency shift in scattered light from elastic waves is used to measure the sound velocity [26]. The glass transition is determined from the change in the pressure or temperature coefficient of the sound velocity. This velocity of sound in the lubricant is derived from the measured frequency shift of the light scattered by elastic waves. Using the BLS technique, Kobayashi and Fujita [98] showed that the limiting shear stress occurs in the viscous, viscoelastic, and glassy states of a lubricant. The high pressure and high temperature BLS has also been used to examine the sound velocity and elastic properties of water [99].

This section demonstrates how Raman and Brillouin spectroscopy can be used to probe the molecular interactions of a fluid, by the analysis of the vibrational frequencies, band intensities and band shapes. However, due to the scattering process, fluids which can be probed, i.e. which provide a response high enough to be collected and analysed, are rather rare. Benzyl benzoate satisfies the diverse requirements of Raman and Brillouin techniques. The molecule contains saturated and aromatic components and an ester group, as well as a branch point. Thus, only the evolution of the benzyl benzoate response to the excitation of an incident light relatively to P and T will be discussed in the following section. The T9 mineral oil does not provide enough signal in both techniques, which makes impossible the interpretation of the spectra. Three temperatures have been chosen to perform RLS and BLS measurements.

III.3.1Raman spectroscopy

III.3.1.1 Raman scattering

This optical technique is commonly used to characterize the rotational and vibrational properties of molecules. It has successfully led in the past to the analysis of material microstructures, including chemical structure [100, 101], molecular spatial distribution [102] and orientation [103, 104].

The principle is to irradiate a sample with a monochromatic light, usually from a laser source in the visible, near infrared, or near ultraviolet range. Unlike infrared spectroscopy where the sample is irradiated with a polychromatic light, monochromatic light (of v_0 frequency) does not match any absorption bands of the material. Therefore, nearly all the light is reflected or transmitted by the sample whereas a very small proportion is scattered in all directions. Scattered light itself can be divided into elastic and inelastic scattering. The major part scatters elastically which means that the energy (i.e. frequency) of the incident light is equal to the emitted light. This phenomenon is referred to as Rayleigh scattering. A minor part (less than one hundred thousandth) scatters inelastically meaning that a small fraction of energy is transferred between molecule and photon. Inelastic scattering can be further distinguished between two different cases (see Figure III-6).

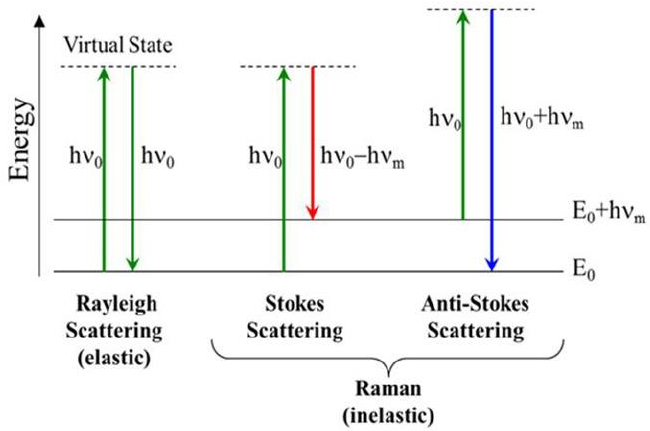

Figure III-6:Jablonski diagram showing transition of energy for Rayleigh and Raman scattering.

In the first case, the molecule is initially in its ground state. After excitation, the molecule falls back to a vibrational energy state above the ground state. As a result, the emitted photon has lost energy and the scattered light will shift to a higher wavelength (Stokes shift $\Delta\nu = \nu_0 - \nu_\nu$). In the second case, the molecule is initially already in a higher vibrational state. After excitation, the photon falls back to the molecule's ground state. The emitted photon has

won energy and the scattered light will shift to a lower wavelength (Anti-Stokes shift $\Delta\nu = \nu_0 + \nu_v$).

In both cases, the frequency difference ν_v to the incident photons represents the vibrational frequency of the molecule. Raman bands are typically reported in wavenumbers (in cm^{-1}):

$$\bar{\nu} = \frac{1}{\lambda}$$

where λ is the the wavelength.

For a non-linear molecule containing N atoms, it can be shown that the molecule possesses 3N-6 normal modes of vibration. But a linear molecule has 3N – 5 vibration modes, because the rotation about its molecular axis cannot be observed. The typical wave numbers (frequencies) of molecular vibrations range from 10 to 4000 cm^{-1}. Each mode has a characteristic vibrational frequency which is a consequence of the masses of the atoms and the force constants involved in the mode of vibration. The Raman spectrum is dispersed over a wider wavelength range when the excitation length is high. In consequence, spectral resolution varies along the Raman spectrum.

An example of a Raman spectrum is given in Figure III-7. The resulting spectrum represents arbitrary intensity of the collected scattered radiation plotted relatively to the Raman band. This spectrum exhibits peaks of intensity corresponding to the different high frequency molecular vibrations.

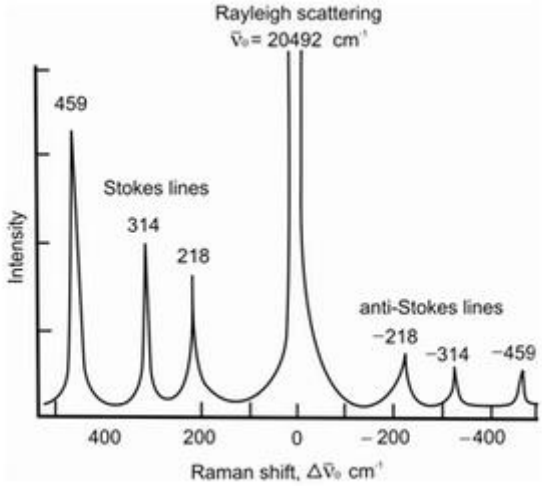

Figure III-7: Example of a Raman spectrum (CCl4, 488 nm excitation)

Each characteristic of a Raman band, frequency, intensity and full width at half maximum (FWHM) contains information on the studied molecule, the nature of the chemical bonds and their neighbouring environment. The frequency (i.e. the Raman band) of the vibrational modes of liquid-phase molecules depends on force constants, atomic masses, bond distances, angles, and electric charges, which are modified by molecular interactions with the surrounding potential. Band profiles and FWHMs depend on dynamic parameters from atomic and molecular motions. Shifting of bands towards lower or higher wavenumber is related to the chemical bond lengths of the molecules. A shorter bond length causes a shift toward a higher wavenumber or vice versa. Therefore, internal or external effects such as pressure, mechanical stress and temperature may cause to shift the wavenumber [97]. The intensity of a band is related to the number of scattering molecules of the probed volume. It is a function of:

- Intrinsic polarization of the radiation
- Polarization conditions of the excitation and signal collection
- Concentration : number of vibrators / volume
- Efficient section of Raman scattering
- Molecular interactions,pressure and temperature.

Pressure plays a significant role in regulating the total energies of highly compressible molecules by changing the inter and intramolecular distances [105]. At elevated pressures, structural and chemical stabilities can be completely altered and thus a wide variety of transformations (gauche or trans in equilibrium) are often induced. Raman spectroscopy can determine whether changes such as phase changes, glass transitions, conformational changes, and chemical changes, occur under pressure.

In EHL, a small volume of lubricant is submitted to very high pressure and the fluid may be subjected to a phase change (glass phase transition) resulting in a decrease of interatomic distances and/or vibrational modes changes. The former trend is significant in the case of fluids and is (much weaker) in the case of solids. Thus, the evolution of the Raman spectra should be sensitive to these effects and should allow characterizing them, as in the works of [103, 104]. Indeed, it has been shown that the bonds become stiffer under pressure. At different pressure regions, the shift rates are different, providing evidence of phase transformations [106]. The frequency shift increases proportionally to the applied pressure from 0 to a few tens of GPa [106–108]. For a given molecule, the proportionality coefficient is characteristic of each vibration mode. It ranges from 1 to 10 cm^{-1}/GPa for internal vibration modes and 3 to 10 cm^{-1}/GPa for deformation modes [97].

Zhi-Xue and Hai-Fei [109] investigated the behavior of 1-Dodecene at 21°C and pressures up to 3 GPa by using a moissanite anvil cell. They found two significant discontinuities in the Raman band versus pressure that they interpreted two phase transitions of the fluid. One is liquid–solid transition at a pressure of about 0.5 GPa, the other is a solid–solid phase transition at a pressure from 1.30 to 1.55 GPa. The latter was attributed to the orientational change of the plane structure of ethylene. Robert et al.[105] studied the behavior of 1,2-dichloroethane (DCE) at high pressures up to 30 GPa and room temperature by Raman spectroscopy. Their results showed that in the low-pressure range of 0-0.5 GPa, DCE exists as a mixture of gauche and trans conformers in the fluid phase. But at 0.6 GPa, DCE undergoes from liquid to solid phase transition in which only trans conformation of DCE was observed. High-pressure Raman scattering studies at ambient temperature were performed on n-heptane by Kavitha and Narayana [100]. They investigated the behavior of the external modes of n-heptane as a function of pressure. They derived from the evolution of their Raman spectra a liquid-to-solid transition around 1.5 GPa. This fluid was also investigated by Qiao et al.[110]: their results showed that at room temperature the vibration modes, assigned to the symmetric and antisymmetric stretching of CH3 and CH2 stretching, shifted quasi linearly to higher frequencies with increasing pressure, and a liquid–solid phase transition occurred near 1.150 GPa. Phase transformations of chlorocyclohexane (CCH) were investigated in a diamond anvil cell by Raman spectroscopy at room temperature and high pressure up to 20 GPa [106]. It has been shown that CCH exhibits liquid-solid transition at pressure above 0.7GPa.

The advantage of Raman spectroscopy lies in the fact that it is a completely non-destructive technique, provided that the excitation power density is not very high. It is also a rather fast technique, requiring just from a few seconds to some minutes for obtaining a good quality spectrum. Thus, it can be a powerful technique for the rapid identification of phases. However, it requires a transparent sample and, at least, one of the specimen confining the sample under investigation must be a transparent material. Moreover, Raman scattering is not intense, the intensity of the scattered light is about one million times lower than that of the incident light. Therefore this technique does not suit all the samples. That is why benzyl benzoate was chosen, because of its molecular structure leading to an intense Raman response. In particular, its two rings cycles produce a relatively high vibration intensity which should allow collecting enough signal to analyze it, even in an EHD contact. Raman spectrum of benzyl benzoate is given in Figure III-8. The assignments of five Raman active modes are gathered in Table III-5. In this work, the three highest peaks intensities have been studied, as a function of pressure: the ring deformation mode, at 1006 cm^{-1}, the ring stretching mode at 1603 cm^{-1} and the carbonyl stretching mode at 1719 cm^{-1}.

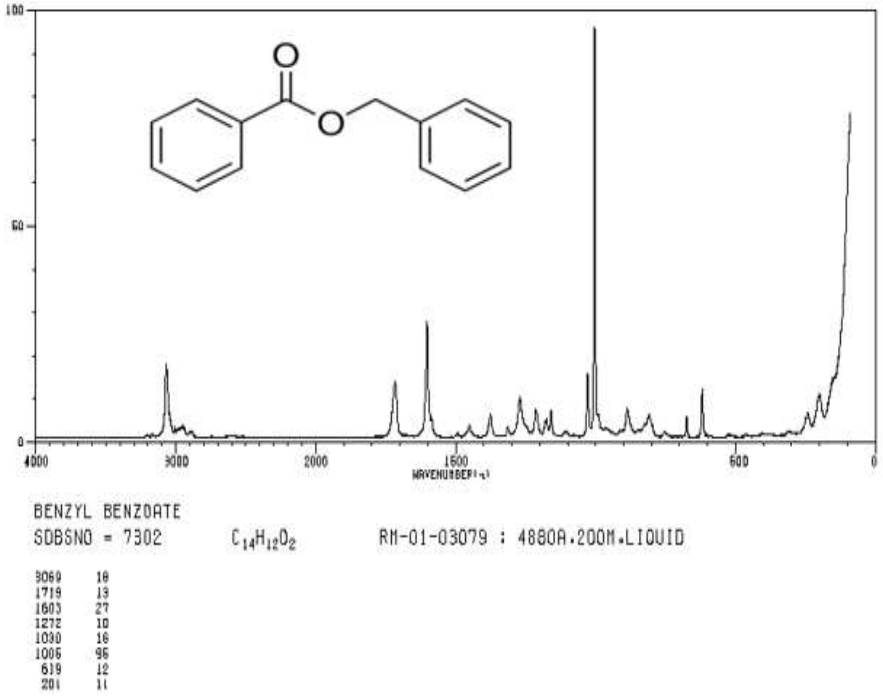

Figure III-8: Schematic structure of the benzyl benzoate molecule, of formula $C_{14}H_{12}O_2$, and its Raman spectrum (SDBS Web: http://sdbs.db.aist.go.jp (National Institute of Advanced Industrial Science and Technology, date of access) (SDBS No.:7302).

Frequency band	Functional group	Symbol	Description
3069	=C-H	$\bar{\nu}$ (=C-H)	aromatic CH stretching
1719	C=0	$\bar{\nu}$ (C=O)	carbonyl C=O stretching
1603	aromatic –C=C	$\bar{\nu}$ (C=C)	i-p C=C ring stretching
1272	-C-O-	$\bar{\nu}$ (C-O)	skeletal C-0 stretching
1006	aromatic –C=C	$\bar{\nu}$ (C=C)	C=C ring deformation

Table III-5: The assignments of five Raman active modes of benzyl benzoate.

III.3.1.2 Experimental protocol

In this work, the benzyl benzoate phase change was investigated in static condition (i.e. out of the EHD contact) by using a Raman micro spectrometer coupled with a high pressure cell working at controlled temperature.

The sample was confined in a diamond anvil cell (DAC) to apply an hydrostatic pressure [44]. DACs have been extensively used in the study of solids and liquids at high pressure [95], [100],

[107, 108]. Experiments were conducted up to 1.2 GPa, in a membrane-type diamond anvil cell designed for low-pressure experiments [111]. This cell is equipped with a 1.4 mm culet diamond anvil and a 400 µm thick diamond window. Pressure is increased in the cell by inflating an internal membrane with helium. Such a system allows a fine control and an excellent stability of the force applied to the anvils (See Appendix E for a detailed description of the pressure cell).

The DAC was cleaned with heptane and then ethanol before being filled with benzyl benzoate. Then, an indicative volume of 100 nl of the sample was placed in the hole (500 µm in diameter) of a nickel gasket (200 µm in thickness), itself compressed between the diamond anvil and the diamond window. The cell was carefully pressurized with small steps. Pressure inside the cell was determined with a precision of 50 MPa, from the calibrated shift of the R1 fluorescence line of ruby microspheres added in the sample chamber [45]. In order to ensure the accuracy of the measurement and the equilibrium state, one/several ruby luminescence shifts were checked before and after each Raman spectrum acquisition. Meanwhile, the sample temperature was adjusted thanks to a heating ring, itself connected to a heating system ensuring a thermal regulation with a precision of ± 0.1 °C. A thermocouple was used to measure the temperature close to the sample.

Each series of experiments was made at constant temperature by varying the pressure. Before the spectra acquisition, a delay of at least 15 min was observed for pressure stabilization in the cell and in the sample. Two different temperatures were investigated: 20°C and 40°C. In reality, the spectroscopic measurements (Raman and Brillouin) were performed at 22° C because the thermal regulation cannot be adjusted to 20°C.

The DAC was mounted on a XYZ micro-positioning stage. X and Y displacements allowed us to accurately locate the laser beam on rubies and the probed area. Z displacement was used to focus on the beam into the lubricant. Focus was adjusted in order to record the maximum of Raman intensity.

The high pressure cell was combined with an optical system comprising a laser source, an optical microscope and a spectrometer, as well as an acquisition system (see Figure III-9).

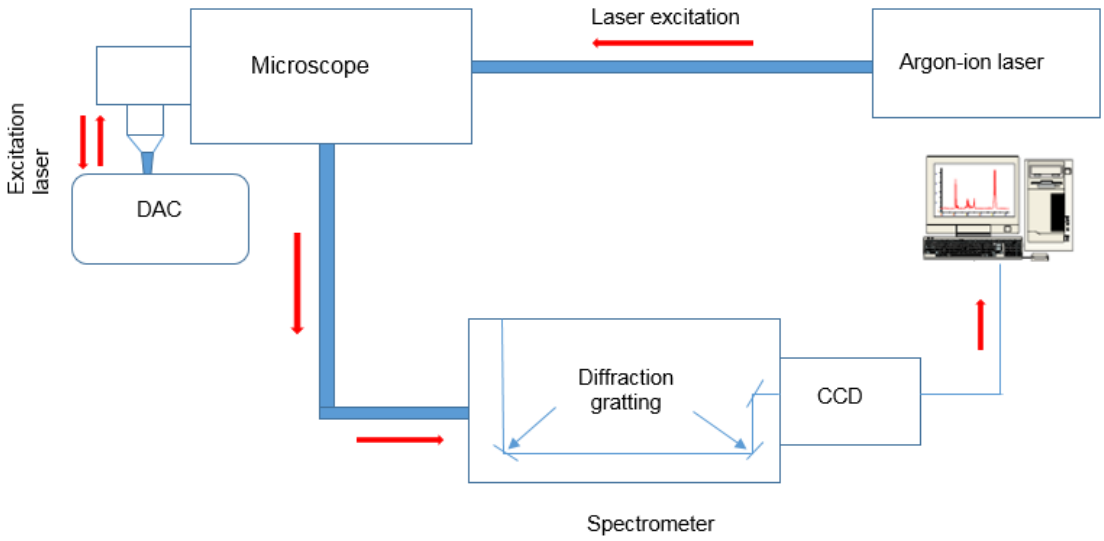

Figure III-9: Coupling between the setup simulating the experimental conditions and the optical and the data acquisition system.

The argon-ion laser 514.532 nm line (Stabilite 2017 - Spectra-Physics) was used at a power on the sample, of approximately 2 mW. The laser is fiber coupled with an optical microscope. Measurements are performed with a X50 long working distance objective. First of all, a series of experiments was performed at ambient pressure by varying the power of the laser beam in order to find the optimal value of power which allows to avoid lubricant heating as much as possible. We investigated the frequency shift of Raman peaks as a function of the power of the laser. It results from the experimental measurements that a power of 2 mw is good enough to have enough Raman signal and to avoid the lubricant heating.

Raman spectra were recorded with a U1000 Jobin-Yvon spectrometer fiber-coupled to the optical microscope. It is mounted with a two-stage monochromator equipped with 300 grooves/mm gratings to disperse the Raman spectrum on a CCD detector, giving a spectral resolution of approximatively 0.8 cm^{-1}/pixel. For each spectrum, the recording time was of 30s, divided into two acquisitions of 15 s. A full description of the experimental setup can be found in [97].

Once a spectrum was recorded, the central frequency (or wavenumber), the FWHM and the intensity of the Raman peak was determined by fitting the data with a Gaussian curve. Due to small room temperature fluctuations, small errors on the ruby peak position could be observed, resulting however in large errors in pressure calculation. To avoid this, a Neon spectral lamp was used as a reference to correct the ruby peak position for each spectrum. In the same way, a Mercury spectral lamp was used to correct the sample peak position. It was found that the

ruby peak wavelength R1 linearly shifts with increasing pressure. Pressure calculation was based on Mao et al results [45], and temperature correction on Datchi et al. [112].

III.3.1.3 Raman experimental results

A typical Raman spectrum of benzyl benzoate obtained in this work is shown on Figure III-10. It exhibits three main peaks, corresponding to three vibration modes of benzyl benzoate highlighted on Figure III-8. The two most intense peaks correspond to the aromatic C=C functional group ring deformation (1003 cm^{-1}) and C=C ring stretching (1601cm^{-1}). The third one, less intense, corresponds to the carbonyl C=O bond stretching, located at 1715 cm^{-1}.

The Raman spectra we measured also displayed two more peaks associated with mercury and diamond vibration modes. The first one, due to the Mercury spectral lamp, was used, as previously quoted, as a reference to correct the parasitic displacement of peak caused by the deformation of the gratings (which is due to thermal fluctuations in the room), whereas the second one, due to the DAC, was not considered.

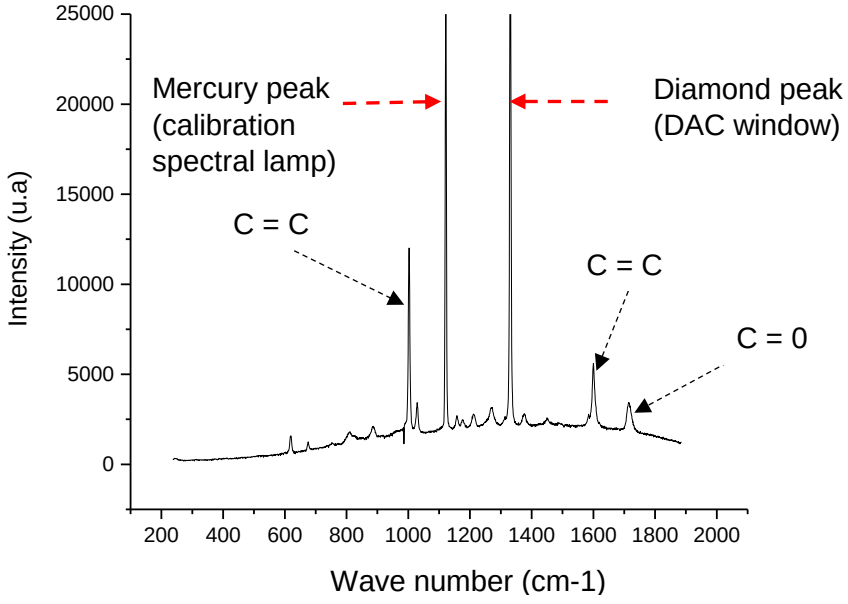

Figure III-10: Raman spectrum of benzyl benzoate at 20°C and P_{atm} (u.a stands for arbitrary units).

A large set of experiments was performed by varying the hydrostatic pressure applied to the sample, in the range of [P_{atm} – 1.3] GPa. Furthermore, two temperatures were investigated: 20°C and 40°C. For each experiment, each of the peaks corresponding to the main bonds C=C ring deformation, C=C ring stretching and C=O was fitted with a Gaussian function, giving

access to the three main parameters: the Raman wavenumber shift, the maximum intensity and the full width at half maximum (FWHM), as shown as an example on Figure III-11 for the C=C ring deformation.

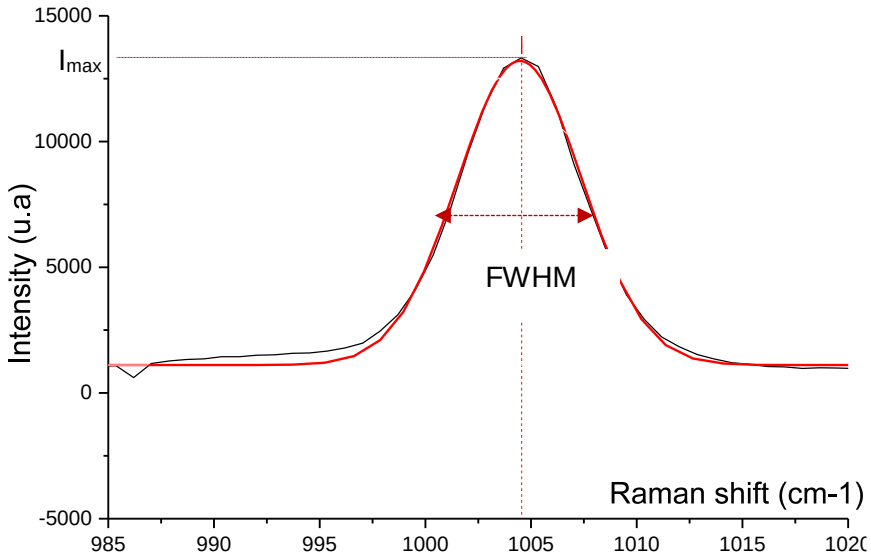

Figure III-11: C=C ring deformation (black curve) and curve fit using a Gaussian distribution (red curve).

The frequency (expressed in wavenumber) evolution as a function of pressure for the previously selected Raman bands is summarized on Figure III-12 (a to c) and Figure III-13 (a to c) at 20 and 40°C, respectively.

At first sight, Raman bands at 1003 cm^{-1} and 1601 cm^{-1} exhibit a monotonous increase versus pressure. Under the effect of an applied hydrostatic pressure, the distance between neighbouring atoms decreases, inducing an increase of their vibration frequencies and therefore a shift of the corresponding Raman bands [97]. The Raman band at 1715 cm^{-1} exhibits a discontinuity versus pressure at about 0.5GPa which indicates a possible phase transition from liquid to solid or glass. The pressure sensitivity of the modes at 1003 cm^{-1} and 1601 cm^{-1} were calculated from the slope of the fitted curves. There are respectively of 3.5±0.1cm^{-1} and 4.1±0.3cm^{-1} cm^{-1}/GPa, for the 1003 cm^{-1} and 1601 cm^{-1} Raman bands respectively. These value are close to the values of 4.2±0.4 cm^{-1}/GPa obtained by Mansot et al. [113] for the Raman band at 1602 cm^{-1} (polystyrene) and 3.3±0.1 cm^{-1}/GPa by Jubault et al. [97] for the Raman band at 1001 cm^{-1} (5P4E).

The second information given by a Raman spectrum is the intensity of the scattered radiation, which is arbitrary as it depends on the intensity of the incident radiation. However, the ratio of the intensities of two vibration modes measured from the same experiment is usually considered in literature as a parameter more sensitive to a modification of the sample

behaviour, as it is representative of the amplitude of a vibration mode relatively to another [102]. For both temperatures, 22 and 40°C, we calculated the intensity ratios between the three peaks, the results are summarized in Figure III-14 and Figure III-15, respectively. At 20°C a sharp change in the slope of the intensity ratio between the C=C ring deformation and the skeletal C=O mode. First, the intensity ratio remains almost constant, up to 0.5-0.6 GPa, due to the same evolution of mobility between the two bonds. Beyond this critical pressure a much higher decrease of the C=C intensity relatively to the C=O leads to a sharp decrease of the intensity ratio. It suggests a loss of mobility of the benzoic aromatic ring relatively to the molecule skeleton, which could denote the appearance of a glass transition in the sample. At 40°C, the result seems to show a change in the slope of the intensity ratio between the C=C ring deformation and the C=C ring stretching mode. The tendency is less pronounced, the intensity ratio is decreasing, meaning an increase of mobility with pressure of the aromatic rings. Furthermore, it shows a slope modification at around 0.9 GPa. Such results have already been interpreted in literature as solidification/glass transition.

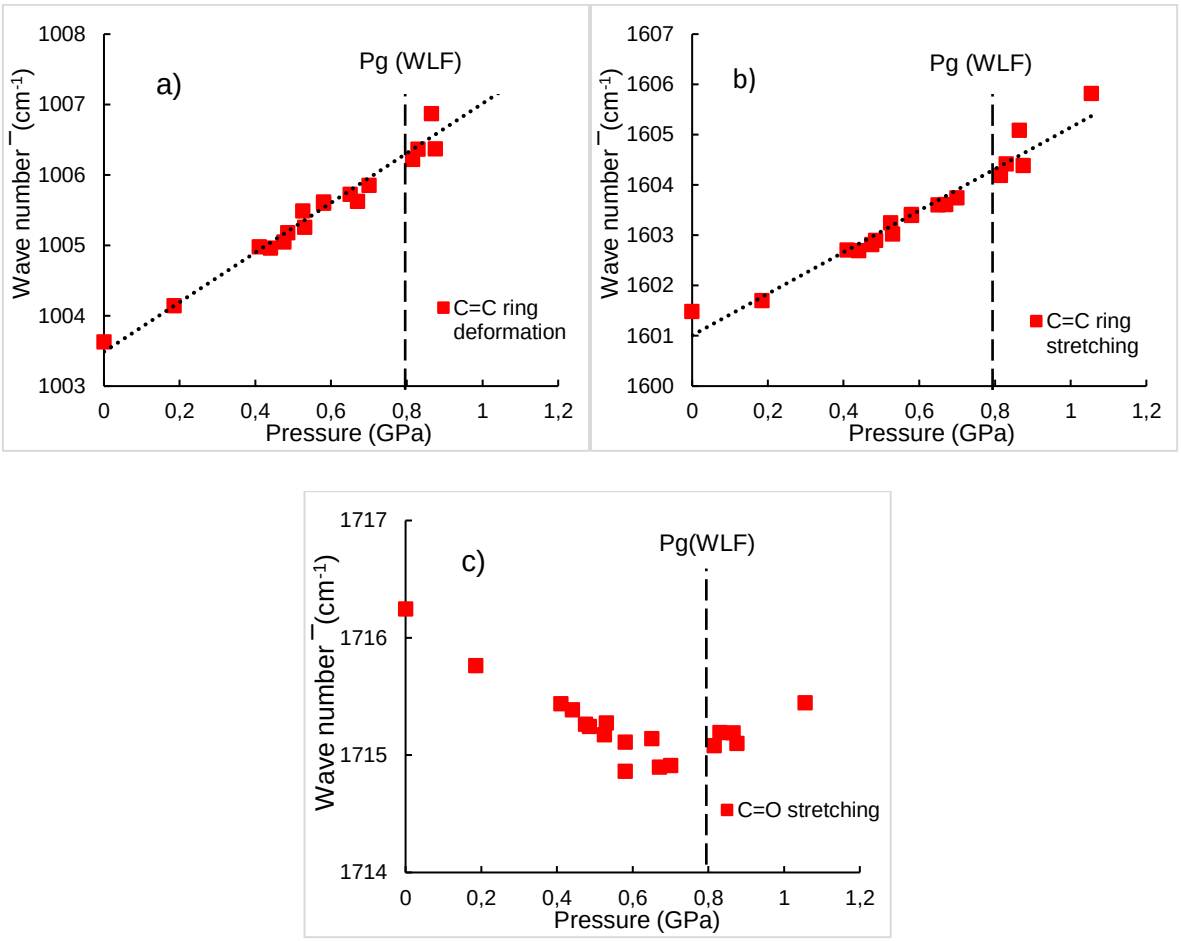

Figure III-12: Wave number variations of the three main vibration modes of benzyl benzoate versus pressure at 20°C.

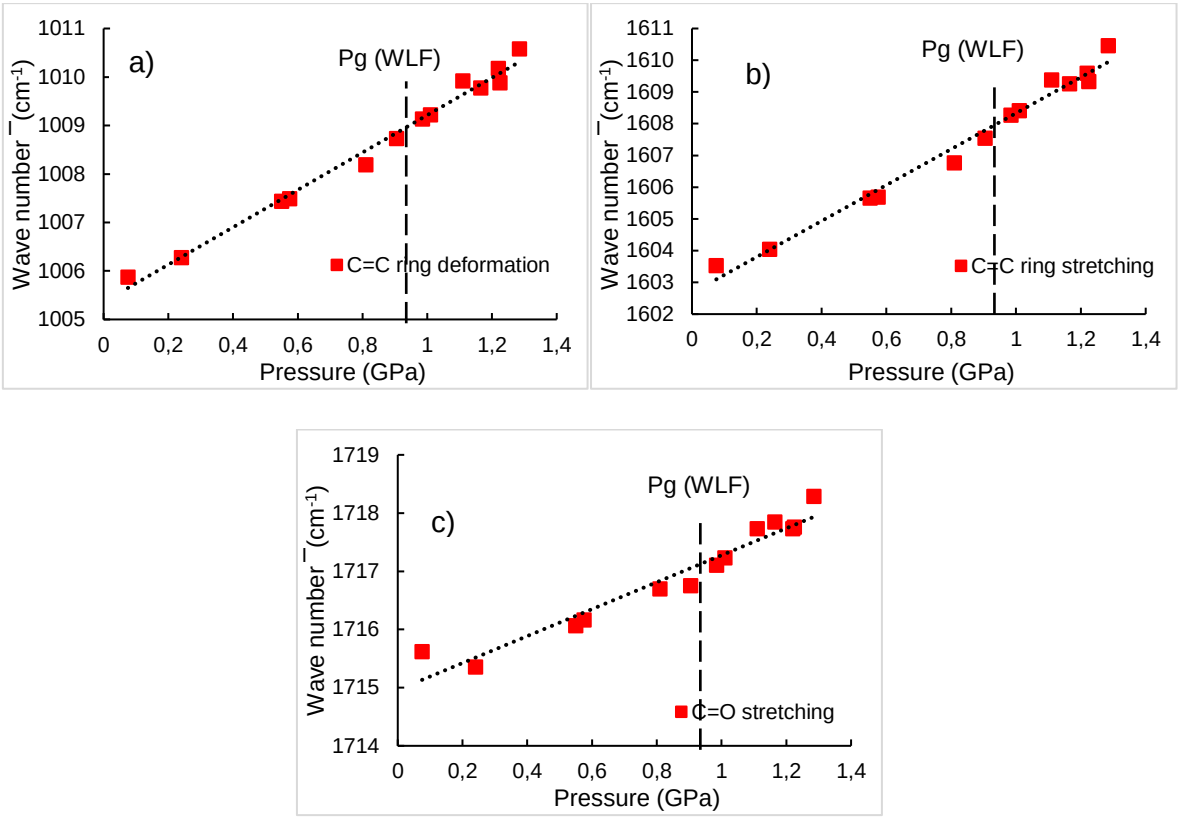

Figure III-13: Wave number variations of the three main vibration modes of benzyl benzoate versus pressure at 40°C.

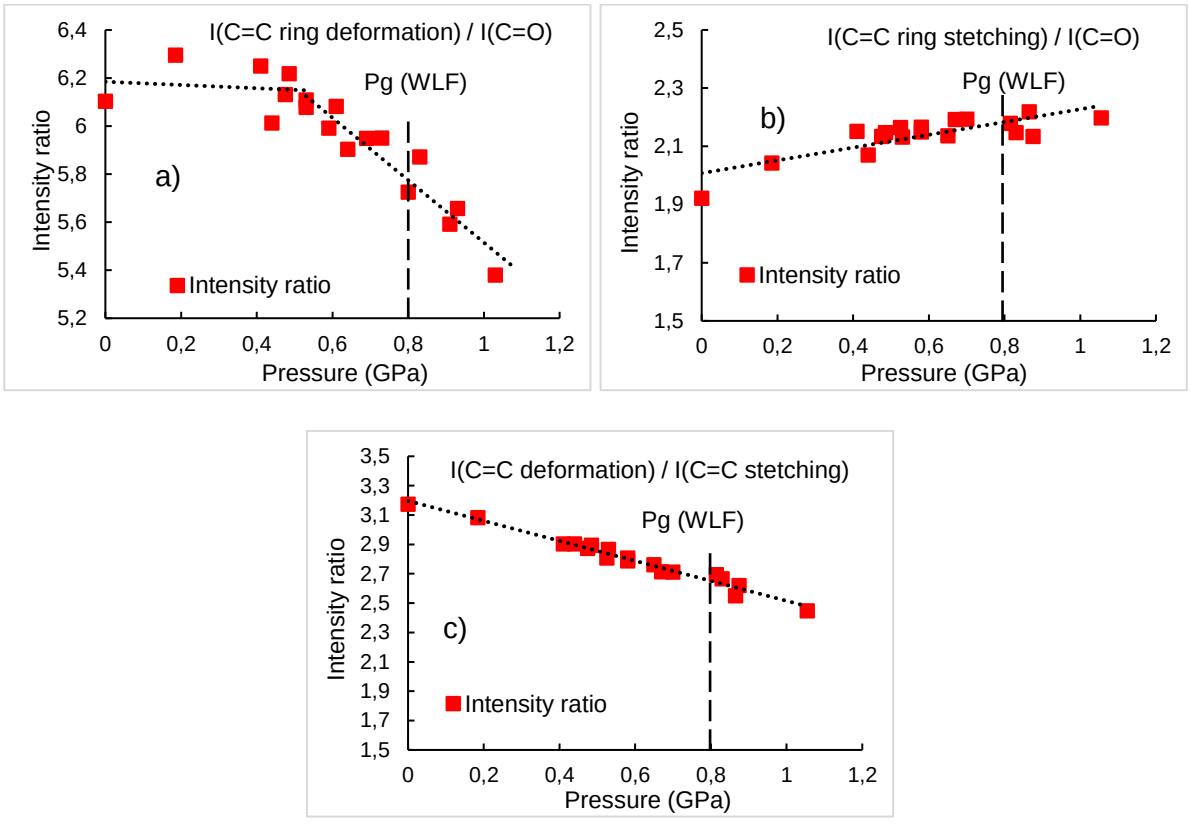

Figure III-14: Intensity ratio variations of benzyl benzoate with pressure at 20°C.

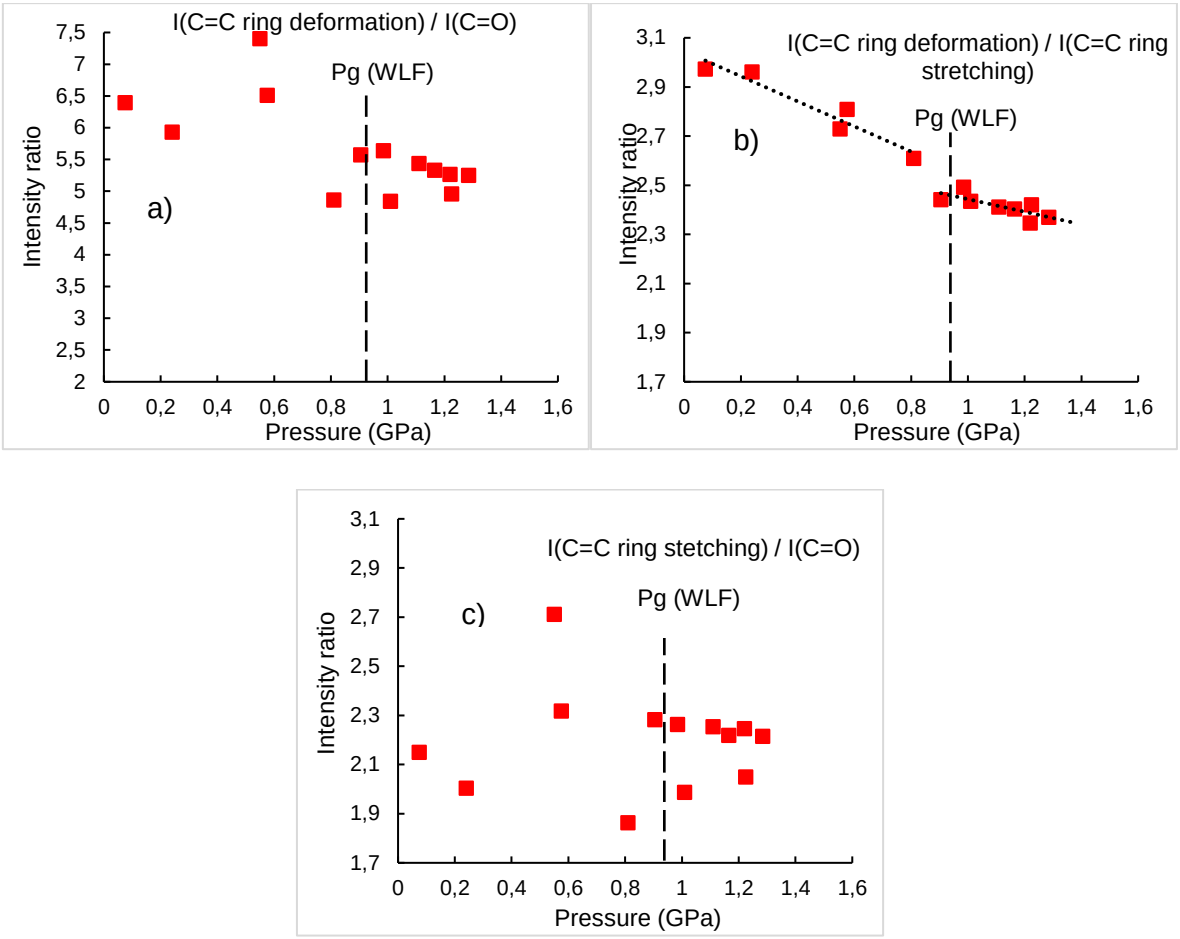

Figure III-15 : Intensity ratio variations of benzyl benzoate with pressure at 40°C.

It is clear that a rather large dispersion is noticeable on the data previously plotted, in particular in Figure III-14 a) and *Figure III-15* (a, c): this dispersions is probably due, at least for a large part, to the construction of the ratio itself. Indeed, a small dispersion on both intensity values can result in a large dispersion on the ratio.

However, these values of 0.5 GPa at 20°C and 0.9 GPa at 40°C are of the same order of magnitude than the glass transition pressures derived from the modified WLF Yasutomi model (respectively 0.8 GPa and 0.98 GPa). The transition pressures obtained by Raman spectroscopy are lower than those derived from the WLF model, which is what was expected. Indeed, Raman spectroscopy gives atomic-scale information about the lubricant phase whereas the WLF Yasutomi model results from macroscopic test.

In order to obtain more conclusive results, the next step of our work has consisted to broaden the domains of investigation of the benzyl benzoate and to implement an alternative technique that could offer more convincing results.

III.3.2 Brillouin spectroscopy

III.3.2.1 Brillouin scattering

Brillouin scattering focuses on the inelastic scattering of light (photons) by thermally generated acoustic vibrations. The incident light produces periodic density variations in the sample which result in local refractive index changes due to waves propagating with the velocity of sound waves. The reflected scattered light experiences a Doppler shift. This latter describes the frequency change of a wave for an observer moving relative to the source of the wave. In brief Brillouin spectroscopy consists in measuring the velocity of sound in a sample [114].

At a quantum scale, the interaction between an electromagnetic wave (photon) and a density wave (low-frequency phonon) involves thermal motions of atoms in the sample that create acoustic vibrations, leading to density variations and the scattering of the incident light [93].
Unlike the atomistic scale probed by Raman spectroscopy, Brillouin scattering involves the scattering of photons by low frequency phonons. Thus, BLS allows to measure macroscopic properties of the sample, as its elastic behavior [115]. Brillouin spectra of fluids reveal only a single peak pair due to longitudinal waves. Spectra of isotropic solids show two peak pairs, one stemming from longitudinal mode and one from the shear mode (two shear modes in isotropic media have equal frequencies). Spectra of anisotropic solids contain three peak pairs due to different acoustic wave velocities measurable in different directions [116]. In liquid our samples, only the longitudinal (compression) mode can be measured, no transverse (shear) mode can be accessible because of the normal incidence of the laser beam in our experimental setup.

BLS spectra usually plot the peak intensity relatively to the wave frequency, which represents the time between two consecutive waves travelling in the sample and thus which depends on the acoustic wave travelling velocity c. The incident light beam is chosen to be at the center of the spectrum, which is named the Rayleigh scattering peak (elastically scattered light). Then the elastic properties of the sample can be determined from each of the Stokes and Anti Stokes peaks. Indeed, the evolution of the sample microstructure is usually derived from the Brillouin peak frequency shift, which is expressed, in normal incidence, as follows:

$$\Delta \upsilon_B = \pm \frac{2n}{\lambda_0} \cdot c \qquad \text{(III-16)}$$

where λ_0 is the excitation wavelength, c the travelling velocity of the waves and n the local refractive index.
Therefore the peak position strongly depends on the acoustic wave velocity and the refraction index of the sample: a local modification of n due to the incident light excitation is thus expected

to shift it. A transition from a liquid phase to a vitreous phase is thus expected to result in a rapid shift of the Brillouin peak frequency, as both the refractive index and the velocity of the acoustic waves are higher in a “solid-like” material than in a “liquid-like” one. It must also be noted that density fluctuations dissipate with time, which results in broadening the peaks due to the attenuation of the acoustic waves. Hence, the FWHM parameter appears to be the adequate parameter to measure the viscous dissipation in a liquid medium [117].

Brillouin spectroscopy has already been used in literature to characterize the glass transition of lubricants [26, 93, 113]. High pressure Brillouin spectroscopy were performed on paraffinic and naphthenic lubricants employing a DAC [115]. The sound velocity in the transverse mode and the shear modulus of 5P4E were measured by Nakamura et al. [115] up to 2.7 GPa. A slope change in the pressure-sound velocity diagram was found at about 0.3 GPa, which may be associated with the crystallization of 5P4E, which was observed through a diamond optical window.

Like Raman spectroscopy, Brillouin spectroscopy is a completely non-destructive technique, suitable for transparent samples submitted to high pressures. However, for the same reasons than that previously quoted in the case of Raman spectroscopy, BLS measurements were not performed on the T9 lubricating oil.

III.3.2.2 Brillouin experimental protocol

BLS was used to identify the phase transition of benzyl benzoate relatively to pressure. Experiments were performed in collaboration with the Institut Lumière Matière-(ILM)-UMR5306, University Claude Bernard Lyon 1. The sample was confined into a DAC at a controlled sample temperature. Three temperatures were investigated: 20°C, 40°C and 60°C. The same DAC was the one previously described in III.1.2 was used for the two lowest temperatures. However, for the 60°C experiments, as transition occurs in the sample a higher pressure, another DAC with two diamond anvils was used. The pressure was generated by trapping the sample between the tiny flat faces on the pointy ends of two diamonds (cutlet faces). A slight force applied to the wide "table" face of the diamond can generate tremendous pressures (up to 20 GPa) on the small "cutlet" face. The same filling and pressure rising protocol than the one previously described in III.1.2 was applied for both DACs.
Brillouin experiments were performed using a Sandercock tandem Fabry Pérot interferometer [46] coupled with a microscope in back scattering geometry with a spatial resolution of 5 µm. Using such system, an ultimate resolution of 10^{-3}cm-1 and a maximum scanning range, free of overlapping orders, of > 50 cm^{-1} can be obtained. More details on the experimental setup may be found in [46]. A 532 nm YAG/ Nd3+ was used as the light source at a power of approximately 5 mW [118]. The ruby luminescence shift in Brillouin experiments was measured

in situ by detecting the luminescence signal with a fiber optic portable monochromator (HR Ocean Optics). The ruby luminescence shift was checked before and after each Brillouin spectrum acquisition. Acquisition time of 30 minutes per spectrum was required to obtain suitable peak shapes. With all these precautions, the pressure uncertainty inside the cell was estimated to be ±0.50 MPa. Brillouin spectra were collected from ambient pressure up to 1.4, 1.5 and 4.75 GPa at 20, 40 and 60°C, respectively. The scattered light was sent through a microscope equipped with a x10 objective for the 20°C and 40°C experiments, and a x20 objective for the 60°C experiments. For each temperature, Brillouin spectra were performed during compression and decompression. It was found that the Brillouin signal was completely reversible and reproducible. As for Raman spectra, Brillouin spectra were fitted with a Gaussian function, giving access to both peak intensity, peak frequency position and FWHM values.

III.3.2.3 Brillouin experimental results

A typical Brillouin spectrum of benzyl benzoate is shown on Figure III-16. The central and most intense peak corresponds to the Rayleigh scattering (elastically scattered light), which is not coupled with the generated acoustic vibrations and only involves the random and incoherent thermal fluctuations. Thus the resulting emitted radiation does not experience any shift neither in energy, nor a fortiori in frequency. In order to focus on the inelastic scattering, this Rayleigh peak is filtered out. Two additional peaks are noticed at respectively lower and higher frequencies than the Rayleigh peak (or incident light) frequency, respectively corresponding to the Stokes and Anti Stokes inelastic scattering. They are due to the longitudinal mode of the acoustic waves propagating in the sample. These peaks are symmetrical and relatively wide, which is typical of liquids. As for the post processing of Raman spectra, each Stoke peak has been fitted with a Gaussian function to extract the three main parameters representative of the microstructure evolution with pressure (cf Figure III-17).

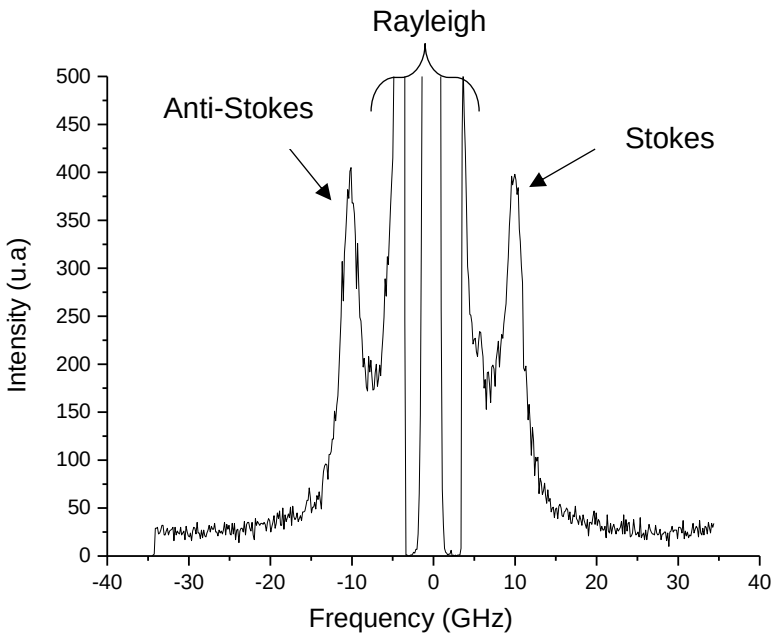

Figure III-16: Brillouin spectrum of benzyl benzoate at 20°C and ambient pressure.

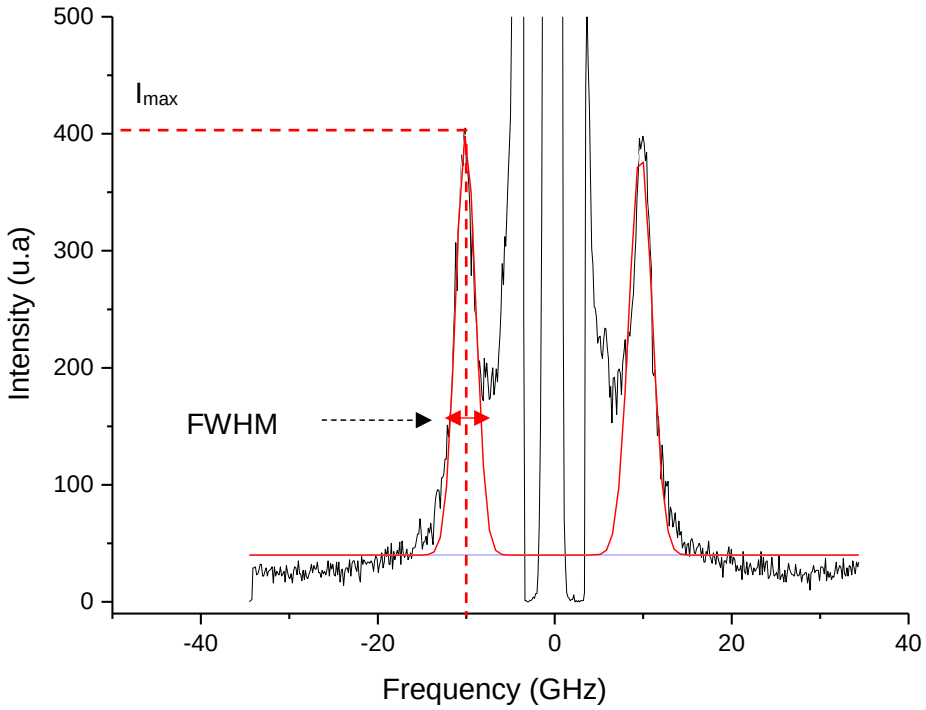

Figure III-17: Brillouin peaks (black curve), fitting using a Gaussian distribution (red curve) and the characteristics of the Gaussian distribution.

First, the Brillouin frequency corresponding to the maximum intensity of each peaks has been plotted versus hydrostatic pressure on Figure III-18 to Figure III-20, for the three investigated temperatures. Data correspond to the triangles (left axis). The three set of results show an

increasing frequency with pressure, probably due to a rearrangement of the benzoic cycles in the sample. Indeed, hydrostatic pressure should decrease the mobility of the cycles, which a priori results in both a higher refraction index and a higher velocity of acoustic waves, and consequently a higher frequency, as shown by equation (III-16). Moreover, this frequency increase with pressure seems to show two distinct tendencies: a first strong evolution of the frequency shift, probably corresponding to the liquid state of the sample, while this evolution is softer at higher pressures due to the sample densification. However no sharp transition between these two regimes can allow to derive a transition pressure. Indeed, Brillouin frequency is known to be representative of the elastic modulus of the sample, which may not be the most appropriate parameter to highlight a phase transition.

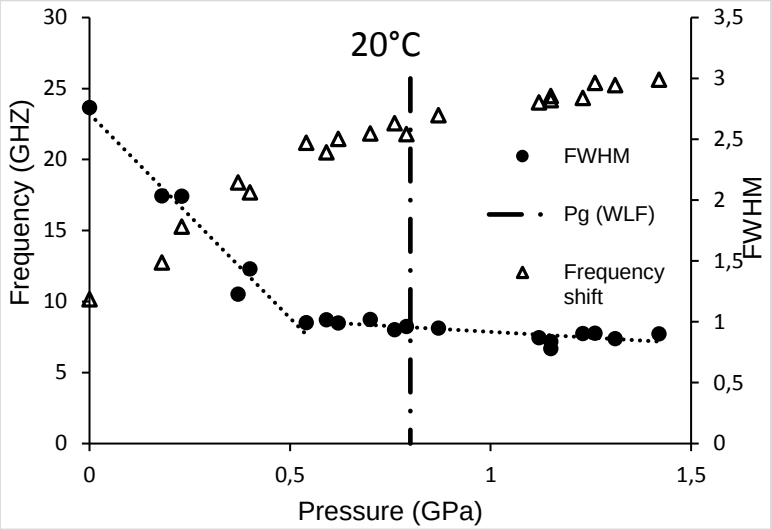

Figure III-18: Brillouin spectroscopy results obtained at 20°C.

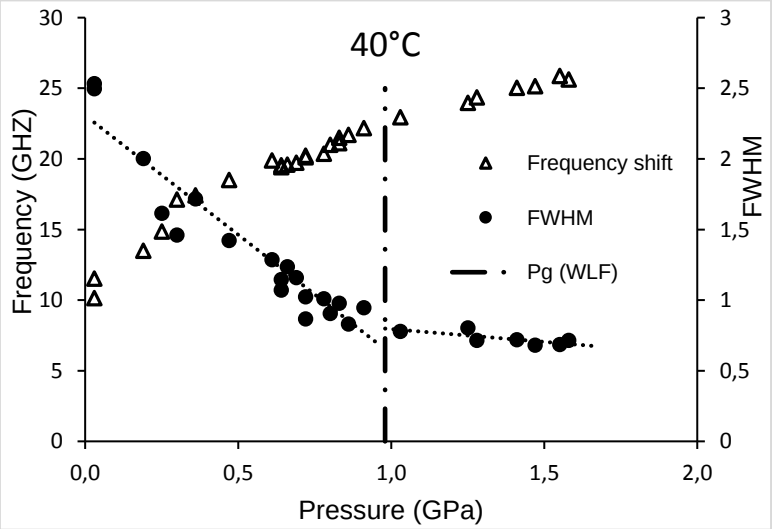

Figure III-19: Brillouin spectroscopy results obtained at 40°C

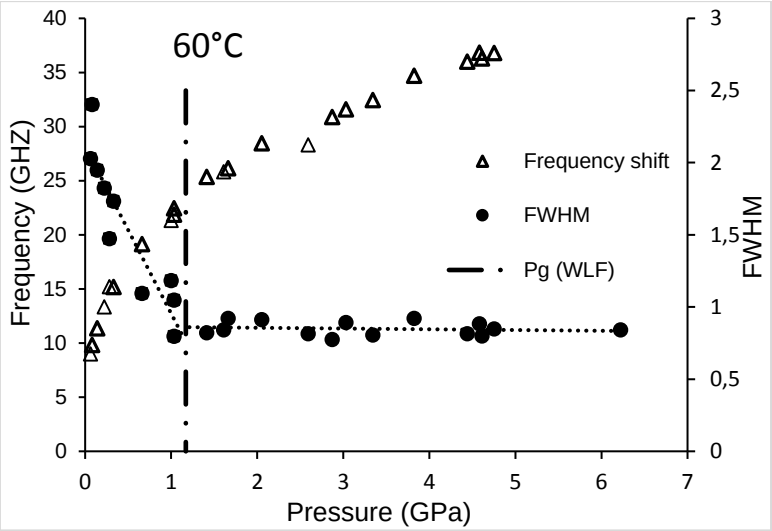

Figure III-20: Brillouin spectroscopy results obtained at 60°C

Therefore, the FWHM parameter (derived from the Gaussian fit of the peaks) has been superimposed on Figure III-18 to Figure III-20 (see the axis on the right). Indeed, this parameter is representative of the attenuation of the acoustic wave propagation, correlated in literature with the sample viscosity [115]. Basically, the thinner the FWHM, the lower the viscosity, with very thin peaks corresponding to solids. It should thus be sensitive to the sample densification. From these figures, a tendency appears much more clearly than with the frequency analysis. A sharp transition occurs between a first regime during which the FWHM strongly decreases with pressure, and a second regime for which (almost) no dependency of the FWHM with pressure is observed. From viscosity considerations, the first regime could be attributed to the high sensitivity of the sample viscosity with pressure in liquid state, whereas the second regime could be representative of a “solid-like” behavior of the sample with no further evolution of its viscosity. This result reminds the evolution of the effective viscosity derived from friction tests and presented in the first part of this chapter. Indeed, this effective viscosity was found to be constant beyond the transition pressure derived from the modified WLF model.

Based on Brillouin spectroscopy, the transition experienced by the material occurs at pressures of order of 0.5 GPa, 1 GPa and 1.2 GPa at 20°C, 40°C and 60°C respectively. These pressures of transition are of the same order of magnitude as those found in Raman spectroscopy and are close to those derived from the modified WLF Yasutomi model, showed by the vertical lines on Figure III-18 to Figure III-20.

It can be noticed that the transition pressures at 20°C display the highest discrepancies among the three experimental methods. The glass transition is a consequence of relaxation times associated with molecular motions becoming inordinately long over a small temperature interval as the temperature is lowered to the transition. This may be due to room temperature fluctuations which affect temperature regulation at 20°C.

III.4 Correlation between the scales investigated

First, the transition pressures derived from the three experimental methods previously described are compared. These pressures are summarized in *Table III-6*. It have already been mentioned that an overall good agreement was obtained.

P_g(GPa)	20°C	40°C	60°C
Raman	0.5	0.9	NM
Brillouin	0.5	1	1.2
WLF	0.8	1	1.2

Table III-6: Summary of the transition pressures (in GPa) derived from Raman spectroscopy, Brillouin spectroscopy and the modified WLF Yasutomi model. "NM" stands for "not measured".

It must first be noted that on *Table III-6*, some transition pressures are to be considered with caution and preferably as orders of magnitude. Indeed the transition pressures from the WLF model were obtained through an extrapolation of the experimental domain allowing to reach a 10^{12} Pa.s viscosity in the material. This is an arbitrary value commonly taken in literature to represent the onset of a "solid-like" behavior, so a more precise transition pressure value could be meaningless. However, these transition pressure values seem to be relatively robust by construction of the modified Yasutomi WLF model. Indeed, a modification of the reference viscosity of one order of magnitude ([10^{11} -10^{13}] Pa.s) in the model would lead to the same transition pressure value +/- 2%, for the three temperatures investigated. This can be assumed to be far below the pressure range over which the fluid transition actually takes place and whose extent is unknown, to our knowledge.

Then, despite the consistency of values presented in *Table III-6*, it is very difficult to ensure that the same physical properties are characterized by the three different methods. On one hand, Raman transition pressures were expected to be slightly lower than the ones derived from Brillouin measurements. However these values are very close to one another (Figure III-21 to Figure III-22).

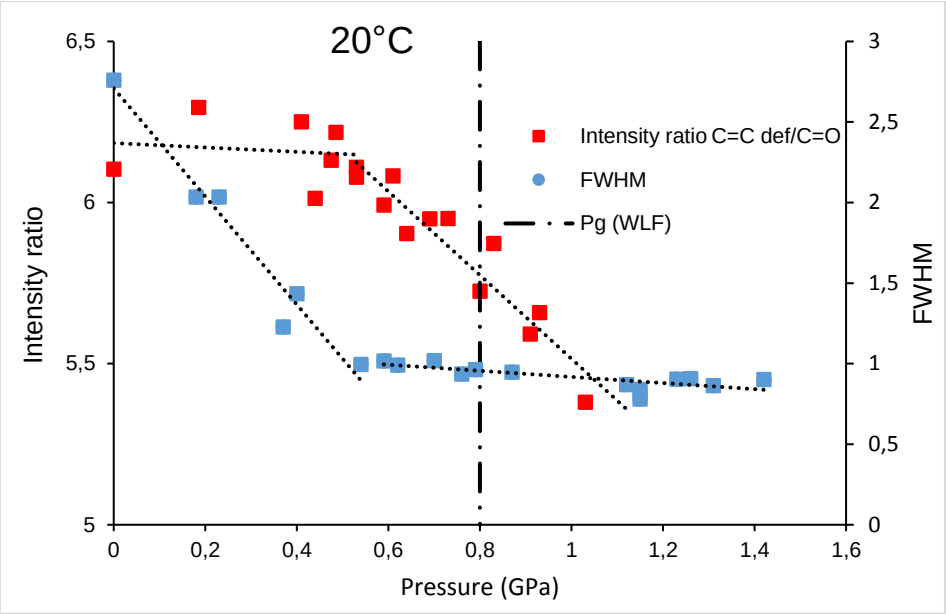

Figure III-21: Spectroscopy measurements relatively to pressure at 20°C. Left axis: C=C ring deformation/C=O Raman peak intensity ratio. Right axis: FWHM of the Brillouin peak.

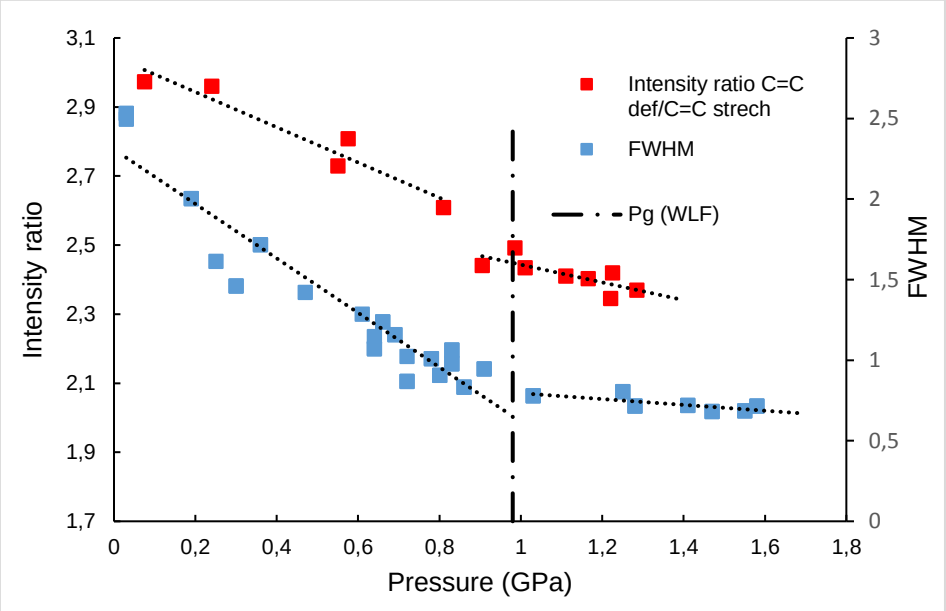

Figure III-22: Spectroscopy measurements relatively to pressure at 40°C. Left axis: C=C ring deformation/C=C ring stretching Raman peak intensity ratio. Right axis: FWHM of the Brillouin peak.

On the other hand, the modified WLF Yasutomi model has been fitted on static, permanent shear tests, so the excitation mode of the sample does not correspond to those of spectroscopic measurements. Surprisingly, the transition pressures derived from the WLF model match well with spectroscopic ones.

In a second part, the transition pressures have been compared to the Hertzian pressures of the friction tests from which LSS triggered, see *Table III-7*.

P_{Hertz} (GPa)	20°C	40°C	60°C
no LSS	0.79	0.98	1.11
LSS	0.99	1.10	1.21

Table III-7: Summary of the Hertzian pressures (in GPa) performed in friction tests leading to a measurable LSS. The first line "no LSS" indicates the highest Hertzian pressure for which no LSS could be measured whereas the second line "LSS" indicates the smallest Hertzian pressure leading to a measurable LSS (according to our LSS criterion).

It appears a good correlation between the "solid-like" state of the benzyl benzoate and the LSS. Indeed, the benzyl benzoate transition measured from friction tests, between curves where no LSS can be measured and curves where LSS appears, occurs at Hertzian pressures which correspond to the glass transition pressure, at least for the 40°C and 60°C temperatures. Experiments performed at 20°C show the highest discrepancy. Surprisingly, for this temperature, the transition pressure derived from the WLF model seems to show the best agreement with friction tests, whereas it was expected to be less accurate than the one derived from spectroscopy measurements.

Moreover, the good correlation between transition pressures from spectroscopic techniques and critical Hertzian pressures leading to a measurable LSS for friction measurements suggests that a small volume of glassy fluid only is sufficient to trigger the LSS, even if the fluid is mainly in a liquid state in the contact. This is a result that contradicts some ancient statement, which suggested that the entire volume of the fluid had to be in a "solid-like" state for the LSS to occur, or vice versa.

Therefore, the glass transition which occurs in the material seems to be a necessary condition for the LSS to occur. However, this is not sufficient. Indeed, looking at a friction curve, the LSS only triggers beyond a critical SRR. The dynamical shearing of the fluid thus appears to be a major ingredient of its asymptotic behavior, which has not been investigated in detail in this work.

So two fundamental questions are still pending. The first one concerns the influence of the contact dynamics on the glass transition pressure of the benzyl benzoate. Indeed glass transition comes from a densification of the fluid, so it refers to intermolecular distances. Therefore, molecules orientation due to shear could influence the occurrence of this transition (and probably increase the transition pressure value).

The second question is of course the role of the contact dynamics on the LSS onset. We will need to answer this question to correctly understand the physical origin of the LSS.

III.5 Conclusion

In the first part of this chapter, we derived an effective viscosity from friction measurements of both benzyl benzoate and a mineral lubricating oil. We showed that the lubricant effective viscosity increases exponentially with pressure below glass transition pressure given by the modified WLF Yasutomi model. Beyond this transition pressure, the effective viscosity was found to be nearly constant.

In a second part of this chapter, a correlation has been made between the benzyl benzoate properties derived from Raman and Brillouin spectroscopy and friction measurements. Transition pressures derived from the three experimental methods showed a rather good agreement at 20°C, and an even better agreement at 40°C and 60°C. For each temperature, the transition pressure obtained with spectroscopic measurements was compared to the Hertzian pressure of friction measurements leading to a measurable LSS. It was found that benzyl benzoate exhibits a measurable LSS beyond this transition pressure. This result first proves the potential of Raman and Brillouin spectroscopy to characterize the microstructure of a fluid under controlled pressure and temperature. These two techniques are complementary, as focusing on different spatial scales. Then, both results suggest the strong correlation between the “solid-like” state of the lubricant and the onset of a limiting shear stress in a contact.

Obviously, a lot of work still needs to be done to achieve a better understanding of the LSS physical origins. First, further measurements of benzyl benzoate should be performed with spectroscopic methods to better characterize its rheological (“liquid-like” or “solid-like”) state. Then, benzyl benzoate must be characterized under EHD contacts, near both the transition pressure and the onset of the LSS. Indeed, it was concluded that glass transition was a necessary condition for the LSS to be measured, but it must be kept in mind that this asymptotic behaviour only triggers beyond a critical SRR, which has not been studied in this work. For that purpose, in situ measurements are needed to simultaneously investigate friction and the microstructure evolution of the fluid.

Finally, this study should be extended to other fluids, and if possible industrial lubricants, to gain credibility. This should not be an easy task as fluids should be carefully selected to provide a measurable spectroscopic signal.

IV Summary and conclusion

This work was devoted to understanding the complex behavior of lubricants in highly loaded contacts. A deeper knowledge of these contacts characteristics and behavior is mandatory for improvement of friction prediction, e.g. in rolling element bearings.

First of all, the environmental and economic impact of friction reduction was presented. Nowadays, significant effort are being devoted to minimize energy consumption due to friction, not only for economic reasons, but also to fight against global warming. Friction reduction in lubrication implies a deep understanding of the multi-physical phenomena that take place in a lubricated contact. Therefore, the main motivation of this work was to improve our understanding on friction in highly loaded lubricated contacts as those formed in rolling element bearings working under full film conditions. Under such high loads, friction reaches a plateau due to the asymptotic behaviour of the lubricant, which is caused by its limiting shear stress.

The first chapter of this manuscript was devoted to an overview of the different scenarios proposed in literature to explain the limiting shear stress physical origin, and also its dependence to the operating conditions. First, some rheological models including a limiting shear stress derived either from high pressure cells, disc machine or impacting ball devices were presented: they describe the lubricant behavior under extreme pressure and shear rate conditions. Then, the different scenarios which may trigger the LSS were reviewed to give a better insight of the various phenomena which could come into play when dealing with such an asymptotic behaviour. However it has been highlighted that none of the scenarios has never been validated as LSS has never been measured simultaneously to them. Finally, the different existing models to describe the pressure and temperature dependence of LSS were also reviewed. Indeed, literature provides several empirical expressions of the LSS which either consider the pressure influence only, or both pressure and temperature, always through a coupling term between both parameters. In the light of these works, we made the assumption that the shear heating might be responsible for the coupled terms.

In the second chapter, we investigated the pressure and temperature dependence of the LSS. In a first step, a series of experiments was performed on two lubricants, a pure diester fluid (benzyl benzoate), and a commercial turbine mineral oil (Shell T9) with different entrainment velocities. This allowed us first to directly observe the influence of the lubricant shear heating on the LSS values. In addition, this led us to determine experimental conditions which limit this shear heating while ensuring an EHD regime with a full film, in order to focus in the following, on a mechanically-driven friction property of the lubricant.

Then a large panel of friction measurements performed with different contacting materials was performed under nominal isothermal conditions and pressures ranging up to 3GPa. We established a new bilinear model to describe the temperature and pressure dependence of the limiting shear stress of benzyl benzoate under highly loaded conditions. This bilinear model was then validated on the mineral oil T9. As far as we know, this is the first time that such LSS model with pressure and temperature uncoupled dependencies is reported. This model contradicts the previous expressions from literature in which both contributions are generally coupled.

The third chapter aimed at improving our understanding of the microscopic behavior of lubricants under extreme shear and pressure conditions. Focus was made on the lubricant solid-like behavior, which is believed to be a necessary condition to trigger the limiting shear stress.

An effective viscosity was derived from the slope of the friction curves in the linear regime. Its variations were studied relatively to the glass transition pressure, derived from the modified WLF variation model. For both fluids investigated, it was found that the effective viscosity increases exponentially with pressure for P lower than P_g, which may be associated to a viscous behavior of the lubricant. However, for P higher than P_g, the effective viscosity remains almost constant, which can be associated to a solid-like behavior of the lubricant. It was finally found that LSS in friction measurements occurs as soon as the Hertzian pressure is of order of the glass transition pressure. Therefore we concluded that a (very) small portion of the lubricant in the glassy state in the contact can lead to the limiting lubricant behaviour in the contact.

In addition, we investigated the lubricant phase changes under pressure with Raman and Brillouin spectroscopy. Both techniques allowed us to determine a critical pressure representative of a change in the behavior of the fluid under pressure, which we identified as a glass transition pressure. However, these critical pressures showed a good agreement between them, and with those estimated from the WLF viscosity model, at the two highest temperatures investigated. However, a discrepancy was found between spectroscopy measurements and the modified WLF model at 20°C, which is still under discussion and would require further experiments.

Recommendation for future work

In spite of the work accomplished during this study, several questions remain to be answered. This section is an overview of the possible directions to consider in order to improve the predictions of friction and to go deeper into the understanding of the microstructure evolution of lubricants under highly loaded conditions.

First, the limiting shear stress models were derived from experiments carried out over a limited temperature range, up to 80°C. However, to gain credibility and significance, this study might be extended to lubricants of different molecular structure, also to a wider temperature range, representative to those encountered in real systems. This might allow a direct correlation between the lubricant nature (or its chemical composition) and its frictional behavior.

Coupling spectroscopy and friction measurements would be of great interest to investigate simultaneously the frictional behavior and the microstructure evolution of the lubricant. Indeed, the contact dynamics seems to play a major role on the onset of the LSS. Therefore, such experiments would enable to measure the influence of the contact dynamics on the glass transition of the lubricant, and to correlate the onset of LSS with the microstructure behavior. This may help to explain the physical origin of the limiting shear stress.

Finally, ccomparing these results with molecular dynamics simulations would also be of high interest for the understanding of the mechanisms responsible for the LSS. Likewise, numerical investigations on the local behavior of lubricant under highly loaded conditions would give information on how the limiting shear stress develops in the contact area.

Bibliography

[1] G. Amontons, “De la resistance causee dans les machines,” in *Memoires de l’Academie Royal des Sciences*, 1699, pp. 275–282.

[2] C. A. Coulomb, “Mémoires relatifs à la physique,” in *Société Française de Physique*, 1784.

[3] H. Hertz, “On the contact of rigid elastic solids and on hardness, chapter 6: Assorted papers by H,” *MacMillan*, 1882.

[4] O. Reynolds, “On the Theory of Lubrication and Its Application to Mr. Beauchamp Tower’s Experiments, Including an Experimental Determination of the Viscosity of Olive Oil,” *Proc. R. Soc. London*, vol. 40, no. 242–245, pp. 191–203, 1886.

[5] F. P. Bowden and D. Tabor, “Friction and Lubrication of Solids,” *Clarendon, Oxford*, vol. I, p. 337, 1950.

[6] A. Dorinson and K. C. Ludema, “Mechanics and Chemistry in Lubrication,” *Tribol. Ser.*, vol. 9, pp. 241–250, 1985.

[7] M. H. Jones and D. Scott, *Industrial tribology: The practical aspects of friction, lubrication and wear*, vol. 8. Elsevier, 1983.

[8] S. Boyde, “Green lubricants. Environmental benefits and impacts of lubrication,” *Green Chem.*, vol. 4, no. 4, pp. 293–307, 2002.

[9] K. Holmberg, P. Andersson, and A. Erdemir, “Global energy consumption due to friction in passenger cars,” *Tribol. Int.*, vol. 47, pp. 221–234, 2012.

[10] K. Holmberg, P. Kivikytö-Reponen, P. Härkisaari, K. Valtonen, and A. Erdemir, “Global energy consumption due to friction and wear in the mining industry,” *Tribol. Int.*, vol. 115, no. 4, pp. 116–139, 2017.

[11] M. Charlotte, “Physico-chemistry, high pressure rheology and film-forming capacity of polymer-base oil solutions in EHL,” Thesis, Insa de Lyon, 2014.

[12] V. S. J. Craig, C. Neto, and D. R. M. Williams, “Shear-Dependent Boundary Slip in an Aqueous Newtonian Liquid,” *Phys. Rev. Lett.*, vol. 87, no. 5, p. 54504, 2001.

[13] Y. Zhu and S. Granick, “Limits of the hydrodynamic no-slip boundary condition,” *Phys. Rev. Lett.*, vol. 88, no. 10, p. 106102, 2002.

[14] P. A. Thompson and S. M. Troian, “A general boundary condition for liquid flow at solid surfaces,” *Nature*, vol. 389, no. 6649, pp. 360–362, 1997.

[15] E. Schnell, “Slippage of water over nonwettable surfaces,” *J. Appl. Phys.*, vol. 27, no. 10, pp. 1149–1152, 1956.

[16] H. Hervet and L. Léger, “Flow with slip at the wall: From simple to complex fluids,” *Comptes Rendus Phys.*, vol. 4, no. 2, pp. 241–249, 2003.

[17] X. M. Li, F. Guo, and P. L. Wong, “Shear rate and pressure effects on boundary slippage in highly stressed contacts,” *Tribol. Int.*, vol. 59, pp. 147–153, Mar. 2013.

[18] R. Pit, H. Hervet, and L. Léger, “Direct experimental evidence of slip in hexadecane: solid interfaces,” *Phys. Rev. Lett.*, vol. 85, no. 5, pp. 980–983, 2000.

[19] C. R. Evans and K. L. Johnson, “The rheological properties of elastohydrodynamic lubricants,” *Proc. Inst. Mech. Eng. Part C J. Mech. Eng. Sci.*, vol. 200, no. 5, pp. 303–312, 1986.

[20] L. Chang, “On the Shear Bands and Shear Localizations in Elastohydrodynamic Lubrication Films,” *J. Tribol.*, vol. 127, no. 1, p. 245, 2005.

[21] S. Bair and F. Qureshi, “Observations of Shear Localization in Liquid Lubricants Under Pressure,” vol. 115, no. July. pp. 507–513, 1993.

[22] M. A. Plint, “Third paper: traction in elastohydrodynamic contacts,” *Proc. Inst. Mech. Eng.*, vol. 182, no. 1, pp. 300–306, 1967.

[23] S. Bair and C. McCabe, “A study of mechanical shear bands in liquids at high pressure,” *Tribol. Int.*, vol. 37, no. 10, pp. 783–789, 2004.

[24] B. O. Jacobson, “An experimental determination of the solidification velocity for mineral oils,” *ASLE Trans.*, vol. 17, no. 4, pp. 290–294, 1974.

[25] P. Šperka, I. Křupka, and M. Hartl, “Evidence of plug flow in rolling–sliding elastohydrodynamic contact,” *Tribol. Lett.*, vol. 2, no. 54, pp. 151–160, 2014.

[26] M. Alsaad, S. Bair, D. M. Sanborn, and W. O. Winer, “Glass transitions in lubricants: its relation to elastohydrodynamic lubrication (EHD),” *J. Tribol.*, vol. 100, no. 3, pp. 404–416, 1978.

[27] A. Ponjavic, M. Chennaoui, and J. S. S. Wong, “Through-thickness velocity profile measurements in an elastohydrodynamic contact,” *Tribol. Lett.*, vol. 50, no. 2, pp. 261–277, 2013.

[28] K. L. Johnson and J. L. Tevaarwerk, “Shear behaviour of elastohydrodynamic oil films,” in *Proceedings of the Royal Society of London A: Mathematical, Physical and Engineering Sciences*, 1977, vol. 356, no. 1685, pp. 215–236.

[29] E. Höglund and B. O. Jacobson, “Experimental investigation of the shear strength of lubricants subjected to high pressure and temperature,” *J. Tribol.*, vol. 108, no. 4, pp. 571–577, 1986.

[30] W. Hirst and A. J. Moore, “Elastohydrodynamic Lubrication at High Pressures,” *Proc. R. Soc. A Math. Phys. Eng. Sci.*, vol. 360, no. 1702, pp. 403–425, 1978.

[31] L. Houpert, L. Flamand, and D. Berthe, “Rheological and thermal effects in lubricated EHD

contacts," *J. Tribol.*, vol. 103, no. 4, pp. 526–532, 1981.

[32] B. O. Jacobson, "A high pressure-short time shear strength analyzer for lubricants," *J. Tribol.*, vol. 107, no. 2, pp. 220–223, 1985.

[33] C. Mary, D. Philippon, L. Lafarge, D. Laurent, F. Rondelez, S. Bair, and P. Vergne, "New insight into the relationship between molecular effects and the rheological behavior of polymer-thickened lubricants under high pressure," *Tribol. Lett.*, vol. 52, no. 3, pp. 357–369, 2013.

[34] J.-D. Wheeler, N. Fillot, P. Vergne, D. Philippon, and G. Morales Espejel, "On the Crucial Role of Ellipticity on EHD Film Thickness and Friction," *Proc. Inst. Mech. Eng. Part J J. Eng. Tribol.*, vol. 203, no. 12, pp. 1503–1515, 2016.

[35] H. S. Cheng and B. Sternlicht, "A numerical solution for the pressure, temperature, and film thickness between two infinitely long, lubricated rolling and sliding cylinders, under heavy loads," *J. Basic Eng.*, vol. 87, no. 3, pp. 695–704, 1965.

[36] H. S. Cheng, "A refined solution to the thermal-elastohydrodynamic lubrication of rolling and sliding cylinders," *ASLE Trans.*, vol. 8, no. 4, pp. 397–410, 1965.

[37] W. Habchi, S. Bair, and P. Vergne, "On friction regimes in quantitative elastohydrodynamics," *Tribol. Int.*, vol. 58, pp. 107–117, 2013.

[38] B. J. Hamrock and D. Dowson, "Isothermal elastohydrodynamic lubrication of point contacts: part III—fully flooded results," *J. Lubr. Technol.*, vol. 99, no. 2, pp. 264–275, 1977.

[39] C. J. Pierre, D. Gérard, and P. Vergne, "Experimental Results and Analytical Predictions of EHL Film Thickness," *arXiv Prepr. arXiv0704.2356*, 2007.

[40] J. Molimard, "Etude expérimentale du régime de lubrification en film mince. Application aux fluides de laminage." Thesis, Insa de Lyon, 1999.

[41] S. Bair and W. O. Winer, "The high pressure high shear stress rheology of liquid lubricants," *J. Tribol.*, vol. 114, no. 1, pp. 1–9, 1992.

[42] S. Bair, C. Mary, N. Bouscharain, and P. Vergne, "An improved Yasutomi correlation for viscosity at high pressure," *Proc. Inst. Mech. Eng. Part J J. Eng. Tribol.*, vol. 227, no. 9, pp. 1056–1060, 2013.

[43] K. L. Johnson and R. Cameron, "Fourth paper: shear behaviour of elastohydrodynamic oil films at high rolling contact pressures," *Proc. Inst. Mech. Eng.*, vol. 182, no. 1, pp. 307–330, 1967.

[44] Y. Nakamura, A. Takimoto, and M. Matsui, "Rheological study of solidified lubricant oils under very high pressure by observing microsphere deformation and viscosity prediction," *Lubr. Sci.*, vol. 22, no. 10, pp. 417–429, 2010.

[45] H. K. Mao, J.-A. Xu, and P. M. Bell, "Calibration of the ruby pressure gauge to 800 kbar under quasi-hydrostatic conditions," *J. Geophys. Res. Solid Earth*, vol. 91, no. B5, pp. 4673–4676,

1986.

[46] S. M. Lindsay, M. W. Anderson, and J. R. Sandercock, “Construction and alignment of a high performance multipass vernier tandem Fabry–Perot interferometer,” *Rev. Sci. Instrum.*, vol. 52, no. 10, pp. 1478–1486, 1981.

[47] H. A. Spikes, “Sixty years of EHL,” *Lubr. Sci.*, vol. 18, no. 4, pp. 265–291, 2006.

[48] A. N. Grubin, I. E. Vinogradova, and K. F. Ketova, *Investigation of the Contract of Machine Components*. Central Scientific Research Institute for Technology and Mechanical Engineering, 1949.

[49] D. Dowson and G. R. Higginson, “A numerical solution to the elasto-hydrodynamic problem,” *J. Mech. Eng. Sci.*, vol. 1, no. 1, pp. 6–15, 1959.

[50] D. Dowson and G. R. Higginson, *Elasto-hydrodynamic lubrication: the fundamentals of roller and gear lubrication*, vol. 23. Pergamon Press, 1966.

[51] C. Barus, “Isothermals, isopiestics and isometrics relative to viscosity,” *Am. J. Sci.*, vol. 45, no. 266, pp. 87–96, 1893.

[52] A. W. Crook, “Elastohydrodynamic lubrication of rollers,” *Nature*, vol. 190, no. 4782, pp. 1182–1183, 1961.

[53] J. F. Archard and M. T. Kirk, “Lubrication at point contacts,” in *Proceedings of the Royal Society of London A: Mathematical, Physical and Engineering Sciences*, 1961, vol. 261, no. 1307, pp. 532–550.

[54] R. Gohar and A. Cameron, “Optical measurement of oil film thickness under elasto-hydrodynamic lubrication,” *Nature*, vol. 200, no. 4905, pp. 458–459, 1963.

[55] C. A. Foord, Wc. Hammann, and A. Cameron, “Evaluation of lubricants using optical elastohydrodynamics,” *ASLE Trans.*, vol. 11, no. 1, pp. 31–43, 1968.

[56] S. Bair and M. Kotzalas, “The Contribution of Roller Compliance to Elastohydrodynamic Traction,” *Tribol. Trans.*, vol. 49, no. 2, pp. 218–224, 2006.

[57] A. W. Crook, “The lubrication of rollers IV. Measurements of friction and effective viscosity,” *Philos. Trans. R. Soc. London A Math. Phys. Eng. Sci. Phys. Eng. Sci.*, vol. 255, no. 1056, pp. 281–312, 1963.

[58] W. E. TENNAPEL, H. Moes, and R. Bosma, “Traction in elastohydrodynamic lubrication at low sliding speeds,” in *Industrial Lubrication and Tribology*, 1971, vol. 23, no. 6, p. 208.

[59] A. Cameron, *Principles of Lubrication*. Longman, Harlow, Essex, 1966.

[60] F. W. Smith, “Lubricant behaviour in concentrated contact systems—the Castor oil-steel system,” *Wear*, vol. 2, no. 4, pp. 250–263, 1959.

[61] F. W. Smith, “The effect of temperature in concentrated contact lubrication,” *ASLE Trans.*, vol. 5, no. 1, pp. 142–148, 1962.

[62] A. Dyson, “Frictional traction and lubricant rheology in elastohydrodynamic lubrication,” *Philos. Trans. R. Soc. London A Math. Phys. Eng. Sci.*, vol. 266, no. 1170, pp. 1–33, 1970.

[63] S. Bair, “Shear Strength Measurements of Lubricants at High Pressure,” *J. Lubr. Technol.*, vol. 101, no. July, pp. 251–257, 1979.

[64] W. Hirst and A. J. Moore, “Non-Newtonian behaviour in elastohydrodynamic lubrication,” in *Proceedings of the Royal Society of London A: Mathematical, Physical and Engineering Sciences*, 1974, vol. 337, no. 1608, pp. 101–121.

[65] S. Bair and W. O. Winer, “The high shear stress rheology of liquid lubricants at pressures of 2 to 200 MPa,” *J. Tribol.*, vol. 112, no. 2, pp. 246–252, 1990.

[66] J. A. Brandao, M. Meheux, J. H. O. Seabra, F. Ville, and M. J. D. Castro, “Traction curves and rheological parameters of fully formulated gear oils,” *Proc. Inst. Mech. Eng. Part J J. Eng. Tribol.*, vol. 225, no. 7, pp. 577–593, 2011.

[67] B. O. Jacobson, “Rheology and elastohydrodynamic lubrication,” vol. 19, Elsevier New York USA, 1991, pp. 1–382.

[68] C. W. Wu, P. Zhou, and G. J. Ma, “Squeeze fluid film of spherical hydrophobic surfaces with wall slip,” *Tribol. Int.*, vol. 39, no. 9, pp. 863–872, 2006.

[69] K. L. Johnson and J. G. Higginson, “A non-Newtonian effect of sliding in micro-EHL,” *Wear*, vol. 128, no. 3, pp. 249–264, 1988.

[70] Y. Zhu and S. Granick, “Rate-dependent slip of Newtonian liquid at smooth surfaces,” *Phys. Rev. Lett.*, vol. 87, no. 9, p. 96105, 2001.

[71] P. L. Wong, X. M. Li, and F. Guo, “Evidence of lubricant slip on steel surface in EHL contact,” *Tribol. Int.*, vol. 61, pp. 116–119, May 2013.

[72] J. Richmond, O. Nilsson, and O. Sandberg, “Thermal properties of some lubricants under high pressure,” *J. Appl. Phys.*, vol. 56, no. 7, pp. 2065–2067, 1984.

[73] Y. Zhang and K. T. Ramesh, “On the compressibility of a glass-forming lubricant: experiments and molecular modeling,” *J. Mech. Phys. Solids*, vol. 46, no. 10, pp. 1699–1722, 1998.

[74] M. Kaneta, H. Nishikawa, and K. Kameishi, “Observation of wall slip in elastohydrodynamic lubrication,” *J. Tribol.*, vol. 112, no. 3, pp. 447–452, 1990.

[75] S. Bair, F. Qureshi, and W. O. Winer, “Observations of shear localization in liquid lubricants under pressure,” *J. Tribol.*, vol. 115, no. 3, pp. 507–513, 1993.

[76] A. Ponjavic, L. Mare, and J. S. S. Wong, “Effect of pressure on the flow behavior of polybutene,”

J. Polym. Sci. Part B Polym. Phys., vol. 52, no. 10, pp. 708–715, 2014.

[77] S. Butler and P. Harrowell, “Simulation of the coexistence of a shearing liquid and a strained crystal,” *J. Chem. Phys.*, vol. 118, no. 9, pp. 4115–4126, 2003.

[78] R. G. Horn and J. N. Israelachvili, “Direct measurement of structural forces between two surfaces in a nonpolar liquid,” *J. Chem. Phys.*, vol. 75, no. 3, pp. 1400–1411, 1981.

[79] J. Gao, W. D. Luedtke, and U. Landman, “Layering transitions and dynamics of confined liquid films,” *Phys. Rev. Lett.*, vol. 79, no. 4, p. 705, 1997.

[80] J. Gao, W. D. Luedtke, and U. Landman, “Structure and solvation forces in confined films: Linear and branched alkanes,” *J. Chem. Phys.*, vol. 106, no. 10, pp. 4309–4318, 1997.

[81] K. L. Johnson and A. D. Roberts, “Observations of viscoelastic behaviour of an elastohydrodynamic lubricant film,” in *Proceedings of the Royal Society of London A: Mathematical, Physical and Engineering Sciences*, 1974, vol. 337, no. 1609, pp. 217–242.

[82] N. Ohno, N. Kuwano, and F. Hirano, “Effect of bulk modulus of solidified oils under high pressure on tractional behavior,” *Japanese J. Tribol.*, vol. 38, no. 10, pp. 1361–1372, 1993.

[83] A. J. Barlow, G. Harrison, J. B. Irving, M. G. Kim, J. Lamb, and W. C. Pursley, “The effect of pressure on the viscoelastic properties of liquids,” in *Proceedings of the Royal Society of London A: Mathematical, Physical and Engineering Sciences*, 1972, vol. 327, no. 1570, pp. 403–412.

[84] B. J. Briscoe and D. Tabor, “Rheology of Thin Organic Films,” *ASLE Trans.*, vol. 17, no. 3, pp. 158–165, Jan. 1974.

[85] E. Höglund, “The relationship between lubricant shear strength and chemical composition of the base oil,” *Wear*, vol. 130, no. 1, pp. 213–224, 1989.

[86] S. Bair and W. O. Winer, “Some Observations in High Pressure Rheology of Lubricants,” *J. Lubr. Technol.*, vol. 104, no. 3, pp. 357–364, 1982.

[87] K. T. Ramesh and R. J. Clifton, “A pressure-shear plate impact experiment for studying the rheology of lubricants at high pressures and high shearing rates,” *J. Tribol.*, vol. 109, no. 2, pp. 215–222, 1987.

[88] H.-S. S. Hsiao and B. J. Hamrock, “A complete solution for thermal-elastohydrodynamic lubrication of line contacts using circular non-Newtonian fluid model,” *J. Tribol.*, vol. 114, no. 3, pp. 540–551, 1992.

[89] W. Habchi, “A Full-System Finite Element Approach to Elastohydrodynamic Lubrication Problems : Application to Ultra-Low-Viscosity Fluids,” Thesis, Insa de Lyon, 2008.

[90] J. P. Chaomleffel, G. Dalmaz, and P. Vergne, “Experimental results and analytical film thickness predictions in EHD rolling point contacts,” *Tribol. Int.*, vol. 40, no. 10–12 SPEC. ISS., pp. 1543–1552, 2007.

[91] V. Wikström and E. Hoglund, “Investigation of parameters affecting the limiting shear stress-pressure coefficient: a new model incorporating temperature,” *J. Tribol.*, vol. 116, no. 3, pp. 612–620, 1994.

[92] W. O. Winer, “Shear strength measurements of lubricants at high pressure,” *J. Lubr. Technol.*, vol. 101, no. 3, pp. 251–257, 1979.

[93] G. Harrison and E. G. Trachman, “The role of compressional viscoelasticity in the lubrication of rolling contacts,” *J. Tribol.*, vol. 94, no. 4, pp. 306–312, 1972.

[94] J. J. Kalker, “On the rolling contact of two elastic bodies in the presence of dry friction,” thesis, TU Delft, Delft University of Technology, 1967.

[95] D. J. Gardiner, E. Baird, A. C. Gorvin, W. E. Marshall, and M. P. Dare-Edwards, “Raman spectra of lubricants in elastohydrodynamic entrapments,” *Wear*, vol. 91, no. 1, pp. 111–114, 1983.

[96] I. Jubault, J. L. Mansot, P. Vergne, and D. Mazuyer, “In-situ Pressure Measurements Using Raman Microspectroscopy in a Rolling Elastohydrodynamic Contact,” *J. Tribol.*, vol. 124, no. 1, pp. 114–120, 2002.

[97] I. JUBAULT, “Application de microspectometrie Rman aux mesures in situ dans les contacts dynamiques,” Thesis, Université des Antilles et de la Guyane, 2002.

[98] H. Kobayashi and Y. Fujita, “Mechanisms for three kinds of limiting shear stresses appearing in the traction modes of viscous, viscoelastic, and glassy states of lubricants,” *J. Appl. Phys.*, vol. 115, no. 22, p. 223509, 2014.

[99] F. Li, Q. Cui, T. Cui, Z. He, Q. Zhou, and G. Zou, “In situ Brillouin scattering study of water in high pressure and high temperature conditions,” *J. Phys. Condens. Matter*, vol. 19, no. 42, p. 425205, 2007.

[100] G. Kavitha and C. Narayana, “Raman Scattering Studies on n-Heptane under High Pressure,” *J. Phys. Chem. B*, vol. 110, no. 17, pp. 8777–8781, 2006.

[101] S. Roy, B. Chamberlin, and A. J. Matzger, “Polymorph discrimination using low wavenumber Raman spectroscopy,” *Org. Process Res. Dev.*, vol. 17, no. 7, pp. 976–980, 2013.

[102] D. Himmel, J. L. Mansot, Y. Bercion, and A. A. Lubrecht, “In situ Raman microspectrometry of lubricated tribologic contacts. Part two: Simultaneous measurements of pressure, lubricant film thickness and temperature distributions in a running EHD contact,” *Tribol. Lett.*, vol. 41, no. 1, pp. 131–144, 2011.

[103] S. Zhang, “In situ observation of the molecular ordering in the lubricating point contact area,” *J. Appl. Phys.*, vol. 116, p. 6, 2014.

[104] S. Zhang and Y. Liu, “Experimental study on molecular arrangement of nanoscale lubricant films—A review,” *Chinese J. Mech. Eng.*, vol. 28, no. 5, pp. 896–903, 2015.

[105] R. J. Sabharwal, Y. Huang, and Y. Song, “High-pressure induced conformational and phase transformations of 1,2-dichloroethane probed by Raman spectroscopy,” *J. Phys. Chem. B*, vol. 111, no. 25, pp. 7267–7273, 2007.

[106] Z. Dong, N. G. Beilby, Y. Huang, and Y. Song, “Conformational and phase transformations of chlorocyclohexane at high pressures by Raman spectroscopy,” *J. Chem. Phys.*, vol. 128, no. 7, p. 74501, 2008.

[107] E. Whalley, A. Lavergne, and P. T. T. Wong, “Hydrostatic optical cell with glass windows for 25 kilobar,” *Rev. Sci. Instrum.*, vol. 47, no. 7, pp. 845–848, 1976.

[108] J. S. Schilling, *Physics of solids under high pressure: proceedings of the International Symposium on the Physics of Solids under High Pressure, Bad Honnef, Germany, August 10-14, 1981*. North Holland, 1981.

[109] D. Zhi-Xue and Z. Hai-Fei, “Raman spectroscopic studies of pressure-induced phase transitions on 1-dodecene,” *Chinese Phys. Lett.*, vol. 25, no. 5, p. 1875, 2008.

[110] E. Qiao, H. Zheng, and C. Long, “In situ high-pressure and high-temperature experiments on n-heptane,” *Appl. Spectrosc.*, vol. 66, no. 2, pp. 233–236, 2012.

[111] A. Picard, P. M. Oger, I. Daniel, H. Cardon, G. Montagnac, and J.-C. Chervin, “A sensitive pressure sensor for diamond anvil cell experiments up to 2 GPa: FluoSpheres®,” *J. Appl. Phys.*, vol. 100, no. 3, p. 34915, 2006.

[112] F. Datchi, R. LeToullec, and P. Loubeyre, “Improved calibration of the SrB 4 O 7: Sm 2+ optical pressure gauge: Advantages at very high pressures and high temperatures,” *J. Appl. Phys.*, vol. 81, no. 8, pp. 3333–3339, 1997.

[113] J. L. Mansot and J. M. Martin, “Measurements of local pressure in a static sphere/plane interface containing organic compounds by means of Raman spectroscopy,” in *Mechanisms and Surface Distress, Proceedings of the 12th Leeds-Lyon Symposium on Tribology*, 1985, pp. 234–237.

[114] S. S. Bair, *High pressure rheology for quantitative elastohydrodynamics*, vol. 54. Elsevier, 2007.

[115] K. Nishibe and H. Kawakami, “Measurement of physical properties of lubricants under high pressure by Brillouin scattering in a diamond anvil cell,” *J. Tribol.*, vol. 117, no. 3, pp. 519–523, 1995.

[116] Sylvia-Monique Thomas, “https://serc.carleton.edu/NAGTWorkshops/mineralogy/mineral_physics/brillouin.html,” *University of Nevada Las Vegas*. .

[117] M. F. N. Murli H. Manghnani, W. J. Nellis, *Science and Technology of High Pressure: Proceedings of the International Conference on High Pressure Sciene and Technology (AIRAPT-17), Honolulu, Hawaii, 25-30 July, 1999*. Universities Press.

[118] C. Sonneville, D. De Ligny, A. Mermet, B. Champagnon, C. Martinet, G. H. Henderson, T. Deschamps, J. Margueritat, and E. Barthel, “In situ Brillouin study of sodium alumino silicate glasses under pressure,” *J. Chem. Phys.*, vol. 139, no. 7, p. 74501, 2013.

Appendices

Appendix A

Rheological properties of benzyl benzoate

- Temperature dependence of viscosity

The rheological characterization of benzyl benzoate has been performed following the approach described in [33]. In the first step, viscosity measurements have been performed at atmospheric pressure for temperatures between -10°C to 120°C in an Anton Paar Couette rheometer (Physica MCR 301). In the range of accessible shear rate ($\dot{\gamma}\epsilon[10^{-1} - 10^{2}]s^{-1}$] s^{-1}) the lubricant remains Newtonian. The viscosity temperature evolution can be represented by the Vogel-Fulcher-Tammann equation as shown on Figure A1.

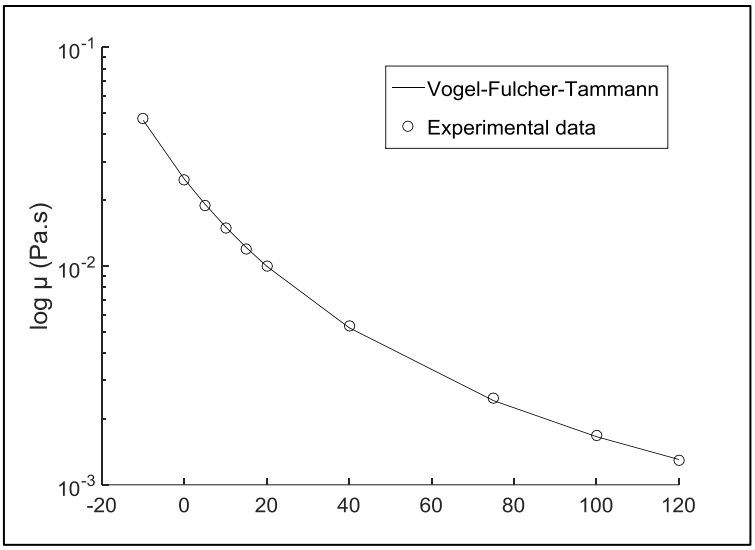

Figure A1: Viscosity-temperature dependance of benzyl benzoate

- Pressure dependence of viscosity

Then a high-pressure falling-body viscometer, was used over an extended pressure range (0-800 MPa) to characterize the benzyl benzoate under pressure. Temperature was varied from 40 to 150 °C, and shear stress was between 1.5 Pa and 70 Pa. The viscosity-temperature-pressure evolution can be describe by the modified WLF model [42], as shown on Figure A2. The model coefficients are gathered in Table A1.

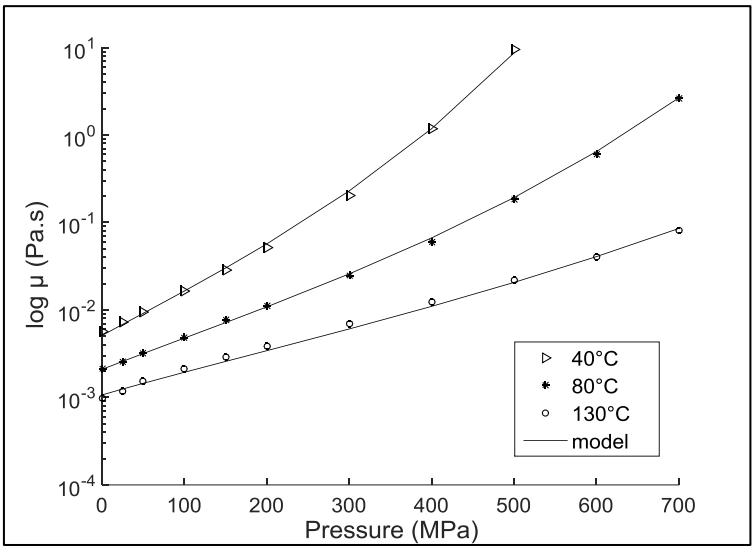

Figure A2: Viscosity-pressure and temperature dependance of benzyl benzoate.

Parameter	Units	Value
A_1	(°C)	400.19
A_2	(GPa^{-1})	0.363
b_1	(GPa^{-1})	5.391
b_2	(-)	-0.399
C_1	(-)	16.00
C_2	(°C)	14.55
$T_{g,0}$	(°C)	-81.73
μ_g	(Pa.s)	10^{+12}

Table A1: Values of WLF model parameters for benzyl benzoate.

The viscosity-pressure dependence at constant temperature is estimated by the reciprocal asymptotic isoviscous pressure coefficient, α*. It is calculated at the friction measurement temperatures (20, 40, 60 and 80°C) from the modified WLF-Yasutomi model [42] and its values together with the viscosity at ambient pressure are given in Table A2.

Temperature (°C)	Viscosity η_0 (mPa.s)	Piezo viscosity coefficient α^* (GPa^{-1})
20	9.97	15.0
40	5.40	12.01
60	3.09	9.93
80	2.09	8.40

Table A2: Pressure-viscosity coefficient of benzyl benzoate.

Appendix B

Rheological properties of T9

- Temperature dependence of viscosity

The rheological characterization of T9 has been performed following the same experimental approach than the one described for benzyl benzoate. Experimental results are summarized in Figure B1. Its viscosity temperature variation is described by the Vogel-Fulcher-Tammann equation.

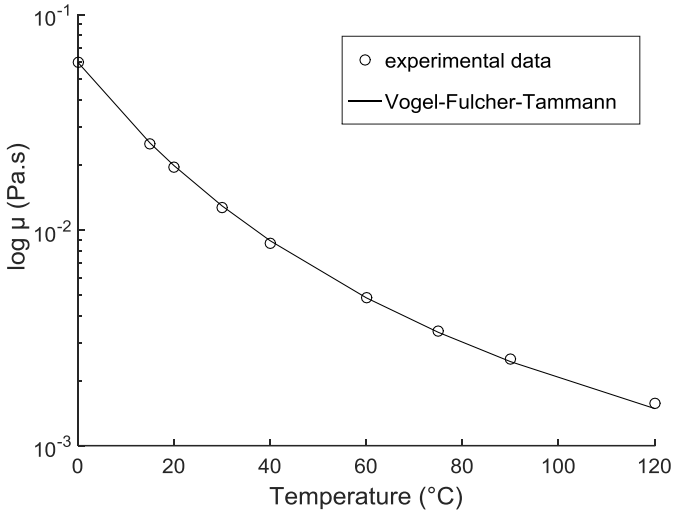

Figure B1: T9 viscosity as function of temperature

- Pressure dependence of viscosity

For the mineral oil T9, the high-pressure falling-body viscometer led to a characterization of pressure dependence of viscosity over a wide range, up to 800 MPa. Temperature was varied from 30 to 150 °C. The data are summarized in Figure B2. The viscosity pressure evolution is fitted by the modified WLF model, whose coefficients are given in Table B1.

Parameter	Units	Value
A_1	(°C)	188.951
A_2	(MPa^{-1})	$5.33.10^{-4}$
b_1	(-)	$7.37.10^{-3}$
b_2	(MPa^{-1})	-0.617
C_1	(-)	15.903
C_2	(°C)	14.159
$T_{g,0}$	(°C)	-68.470
μ_G	(Pa.s)	10^{+12}

Table B1: Values of WLF model parameters for T9

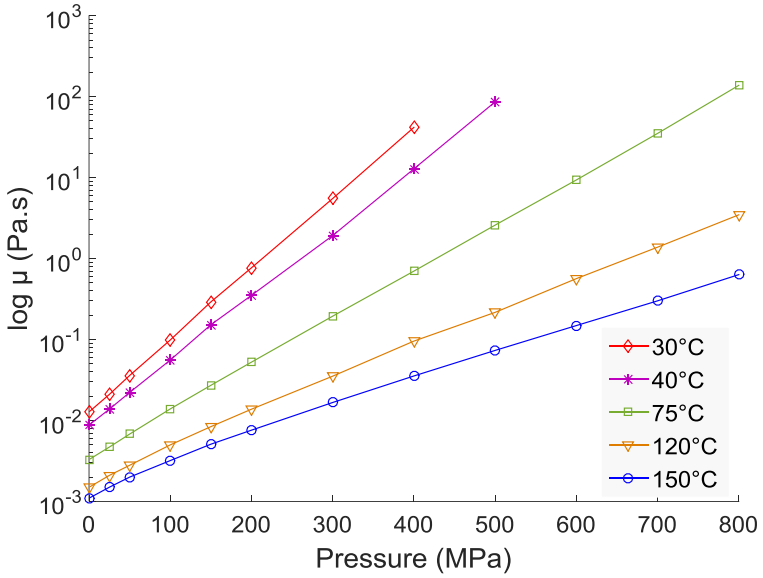

Figure B2: T9 viscosity as function of pressure

The viscosity-pressure dependence at constant temperature is estimated by the reciprocal asymptotic isoviscous pressure coefficient, α*. The results are gathered in Table B2 for the three temperature used for friction measurements.

Temperature (°C)	**Viscosity η_0 (mPa.s)**	**Piezo viscosity coefficient α^* (GPa^{-1})**
20	19.6	23.1
40	8.67	18.6
80	3.001	13.9

Table B2: Pressure-viscosity coefficient of T9

Appendix C

Operating conditions for friction measurements of benzyl benzoate and resulting LSS values.

	Steel/Steel					Steel/Sapphire					
F_z (N)	31	60	107	164	294	39	66	101	179	300	384
P_H (GPa)	0.79	0.99	1.20	1.38	1.67	1.00	1.20	1.38	1.67	1.98	2.15
φ_T (-)	0.99	0.99	0.99	0.98	0.98	0.99	0.99	0.99	0.99	0.98	0.98
h_c (nm)	115	110	106	103	99	112	108	105	101	97	96
$\overline{\tau_L}$ (MPa)	N.A.	42.8	52.4	63.7	79.1	42.4	58.0	64.1	79.3	97.2	108.2

Table C1: Operating conditions for friction measurements with benzyl benzoate in steel/steel and steel/sapphire contacts at 20°C and U_e=1.3 m/s, and resulting LSS values.

	Steel/Steel								Steel/Sapphire			
F_z (N)	31	40	51	59	84	107	166	297	102	182	302	401
P_H (GPa)	0.79	0.86	0.93	0.98	1.10	1.20	1.38	1.68	1.38	1.68	1.99	2.19
φ_T (-)	0.98	0.98	0.98	0.98	0.98	0.98	0.98	0.98	0.98	0.98	0.98	0.98
h_c (nm)	105	104	102	101	99	97	94	91	96	92	89	87
$\overline{\tau_L}$ (MPa)	N.A.	N.A.	N.A.	N.A.	39.5	43.4	54.0	69.7	54.0	69.6	86.4	94.3

Table C2: Operating conditions for friction measurements with benzyl benzoate in steel/steel and steel/sapphire contacts at 40°C and U_e=2.5 m/s, and resulting LSS values.

	Steel/Steel							Steel/Sapphire			
F_z (N)	32	48	61	86	110	165	293	98	172	300	380
P_H (GPa)	0.80	0.92	0.99	1.11	1.21	1.38	1.67	1.37	1.65	1.98	2.15
φ_T (-)	0.98	0.98	0.98	0.98	0.98	0.97	0.98	0.98	0.97	0.97	0.97
h_c (nm)	104	101	100	97	96	93	90	95	91	88	87
$\overline{\tau_L}$ (MPa)	N.A.	N.A.	N.A.	N.A.	34.8	45.0	59.6	42.8	60.9	75.0	87.7

Table C3: Operating conditions for friction measurements with benzyl benzoate in steel/steel and steel/sapphire contacts at 60°C and U_e=5 m/s, and resulting LSS values.

T (K)	20						40			
U_e (m/s)	1.3						2.5			
F_z (N)	38	62	79	123	154	210	38	78	122	208
P_H (GPa)	1.69	2.0	2.16	2.51	2.7	3	1.69	2.15	2.50	2.99
φ_T (-)	0.99	0.99	0.99	0.99	0.99	0.99	0.99	0.99	0.99	0.98
h_c (nm)	105	102	100	97	96	94	96	92	89	86
$\overline{\tau_L}$ (MPa)	84.5	95.6	109.3	127.4	134.6	152.1	74.7	96.9	116.2	139.6.

Table C4: Operating conditions for friction measurements with benzyl benzoate in WC/WC contacts at 20 and 40, and resulting LSS values.

	Steel/Sapphire				WC/WC				
F_z (N)	39	107	178	296	37	60	108	153	208
P_H (GPa)	1.00	1.41	1.67	1.97	1.68	1.97	2.40	2.70	2.99
φ_T (-)	0.98	0.98	0.98	0.97	0.98	0.98	0.98	0.98	0.98
h_c (nm)	85	79	77	74	80	78	75	73	71
$\overline{\tau_L}$ (MPa)	N.A.	N.A.	49.0	64.5	55.0	68.4	85.2	109.4	118.5

Table C5: Operating conditions for friction measurements with benzyl benzoate in steel/sapphire and WC/WC contacts at 80°C and U_e=6.5 m/s, and resulting LSS values.

Appendix D

Operating conditions for friction measurements of T9 and resulting LSS values.

T (K)	20				40				80			
U_e (m/s	0.5				1.3				6.5			
F_z (N)	26	38	53	109	31	54	111	157	32	81	109	290
P_H (GPa)	0.75	0.85	0.95	1.20	0.79	0.95	1.21	1.36	0.80	1.09	1.20	1.67
φ_T (-)	0.99	0.99	0.99	0.99	0.99	0.99	0.99	0.99	0.97	0.97	0.97	0.97
h_c (nm)	122	119	116	111	118	113	108	106	146	137	134	126
$\overline{\tau_L}$ (MPa)	N.A.	N.A.	52.0	66.4	N.A.	46.3	60.7	72.8	N.A.	32.5	38.5	64.5

Table D1: Operating conditions for friction measurements with T9 in steel/steel contacts, and resulting LSS values.

T (K)	20			40				80			
U_e (m/s	0.5			1.3				6.5			
F_z (N)	107	190	306	39	107	189	305	39	107	189	304
P_H (GPa)	1.41	1.70	2.00	1.00	1.41	1.70	1.99	1.00	1.41	1.70	1.99
φ_T (-)	0.99	0.99	0.99	0.99	0.99	0.99	0.98	0.97	0.97	0.97	0.96
h_c (nm)	109	105	101	114	106	102	99	141	132	127	123
$\overline{\tau_L}$ (MPa)	83.7	105.2	124.6	43.4	74.7	93.8	113.6	N.A.	51.5	68.7	85.0

Table D2: Operating conditions for friction measurements with T9 in steel/sapphire contacts, and resulting LSS values.

T (K)	20				40				80			
U_e (m/s	0.5				1.3				6.5			
F_z (N)	61	110	156	211	62	110	156	210	62	109	155	209
P_H (GPa)	1.98	2.42	2.71	3.00	2.00	2.42	2.71	3.00	2.00	2.41	2.71	2.99
φ_T (-)	0.99	0.99	0.99	0.99	0.99	0.99	0.99	0.99	0.97	0.97	0.97	0.97
h_c (nm)	107	102	100	98	104	100	98	96	129	124	121	119
$\overline{\tau_L}$ (MPa)	127.7	150.4	167.4	202.9	121.5	142.8	157.6	190.3	93.7	111.1	125.2	155.3

Table D3: Operating conditions for friction measurements with T9 in WC/WC contacts, and resulting LSS values.

Appendix E

Temperature cell

A voltage was used to induce heating within the sample. The following figure shows the schematic representation of the temperature cell.

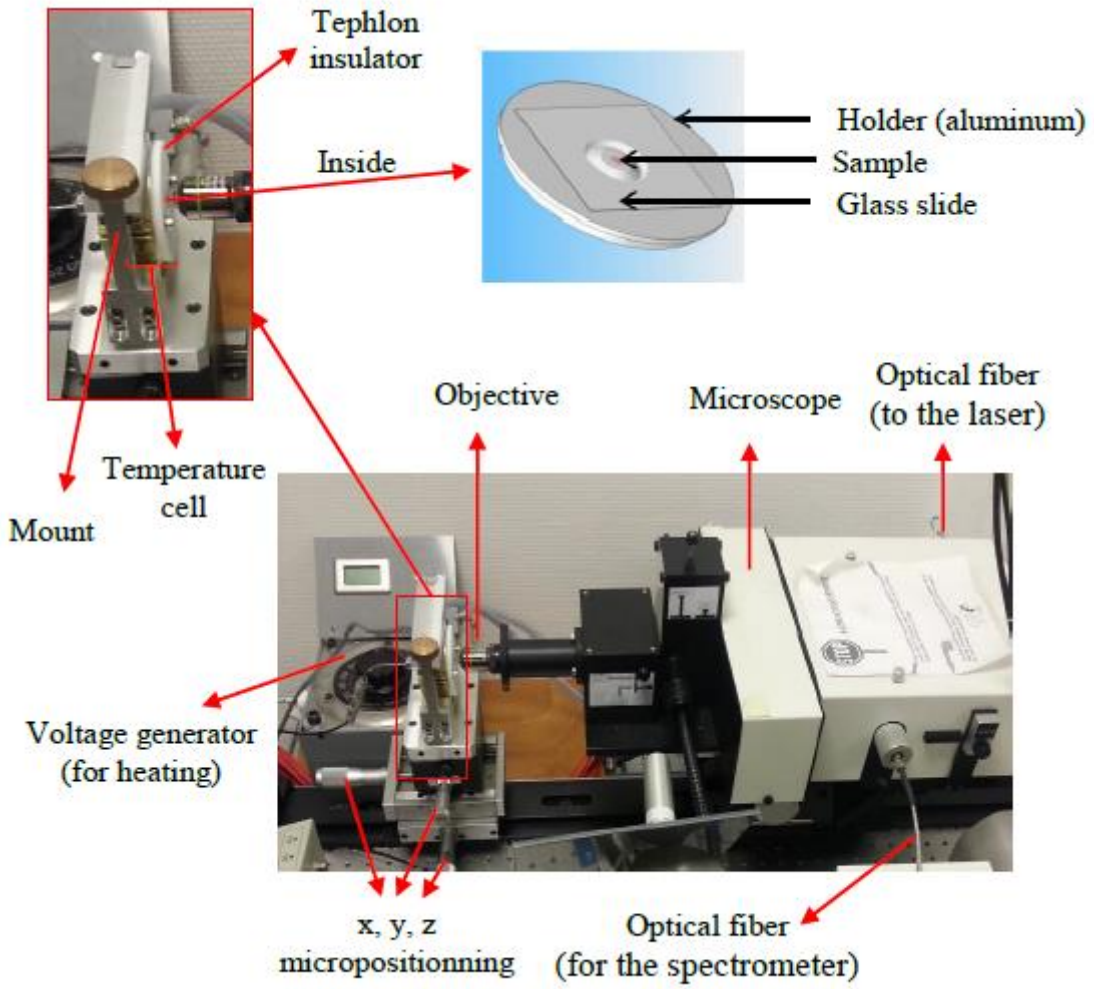

Figure B1: Temperature cell

High pressure cell

Pressure is generated by compressing a pressure chamber into a nickel gasket between opposing diamond anvils. The thickness and the inner radius of the gasket is equal to 250, 200 µm, respectively. Approximate volume of 100 nl of the sample is deposited inside the gasket, and hydrostatic pressure condition is maintained. The following figure shows the schematic of this cell, and the coupling of the cell with the optical system is shown in the following figure B2.

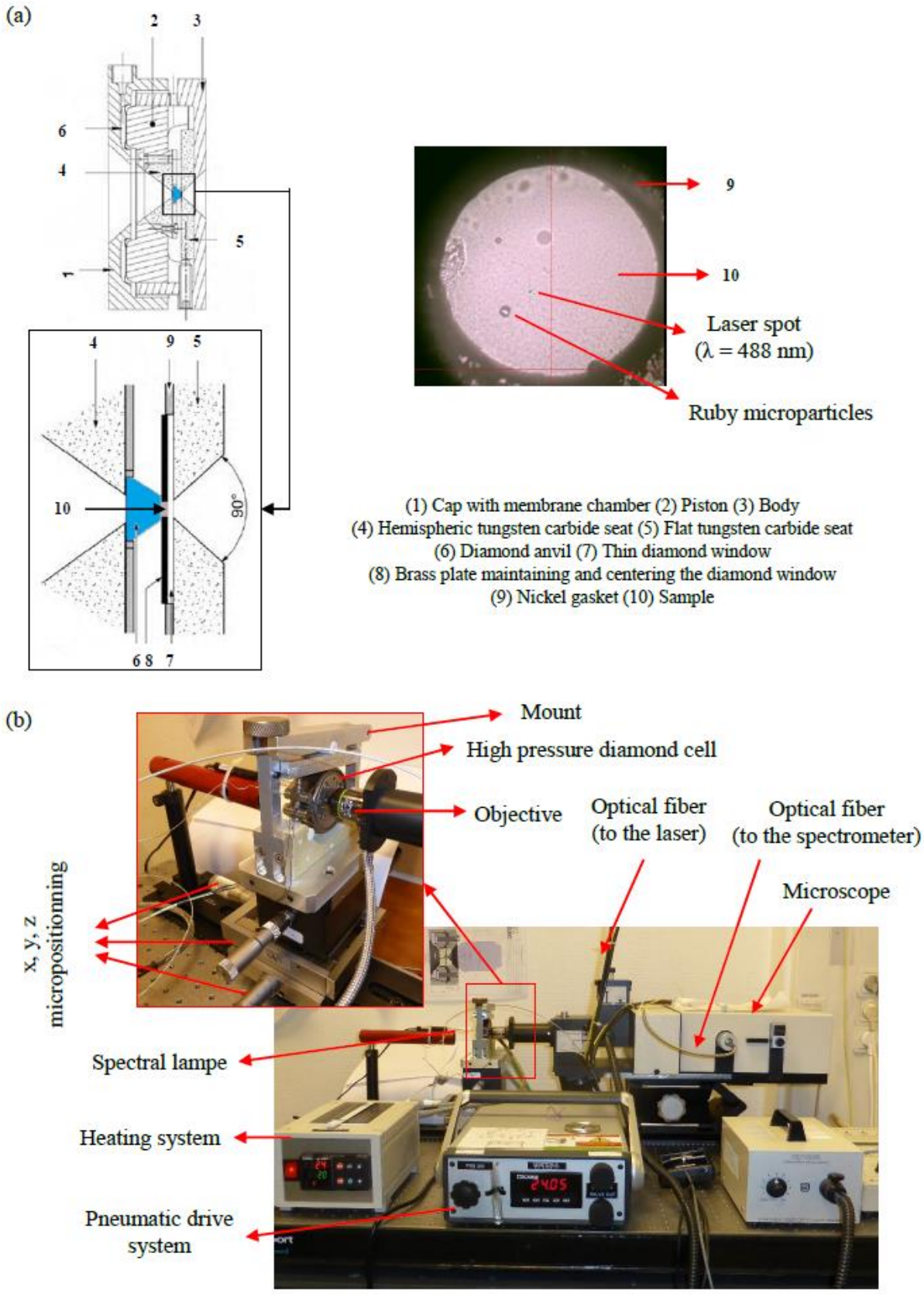

Figure B2: (a) The different parts of the high pressure diamond cell, (b) The coupling of the high pressure cell with the optical system (microscope and spectrometer).

FOLIO ADMINISTRATIF

THESE DE L'UNIVERSITE DE LYON OPEREE AU SEIN DE L'INSA LYON

NOM : NDIAYE DATE de SOUTENANCE : 0.3/11/207

Prénoms : Serigne Ndiaga

TITRE : Ultimate behavior of confined fluids under very high pressure and shear stress

NATURE : Doctorat Numéro d'ordre : 2017LYSEI104

Ecole doctorale : MEGA

Spécialité : Génie Mécanique

RESUME : L'étude du frottement dans les contacts lubrifiés fortement chargés est un sujet complexe. En effet, le frottement dépend fortement du comportement rhéologique du lubrifiant dans le centre du contact et, celui-ci n'est pas bien connu à pression et taux de cisaillement élevé. Diverses méthodes expérimentales ont été développées pour expliquer le comportement plateau dans les courbes de frottement, associé à l'existence d'une contrainte limite de cisaillement, mais aucune d'elles n'a fourni une image complète des mécanismes réels impliqués. Dans la continuité de ces efforts, des études sont présentés dans ce mémoire.

Le premier défi dans ce travail est d'effectuer des mesures de frottement dans des conditions isothermes nominales, ce qui signifie que même si des effets thermiques doivent se produire dans toute mesure de frottement, il est possible de les minimiser et de rendre les résultats insensibles à une faible dissipation d'énergie dans le volume expérimental d'intérêt. La minimisation de l'échauffement du lubrifiant aide à se focaliser sur l'origine mécanique de la contrainte limite de cisaillement et de mieux caractériser sa dépendance à la pression et à la température. C'est pourquoi, tout d'abord, une série d'expériences a été réalisée sur deux lubrifiants, un diester pur (benzoate de benzyle) et une huile minérale de turbine (Shell T9) avec des vitesses d'entraînement variables. Cela nous permet d'abord d'observer directement l'influence des effets thermiques sur les valeurs de la contrainte limite de cisaillement et ensuite, de déterminer les conditions expérimentales qui limitent ces effets tout en assurant un régime en film complet.

Le deuxième objectif est de caractériser le comportement en frottement des lubrifiants sous conditions isothermes nominales et sur une large gamme de pression (jusqu'à 3 GPa) et de température afin d'établir un nouveau modèle découplé permettant de décrire la dépendance à la température et à la pression de la contrainte limite sous fortes charges.

Enfin, l'étude se focalise sur la compréhension du comportement microscopique des lubrifiants dans des conditions extrêmes de cisaillement et de pression. Des mesures in situ de spectroscopie Raman et Brillouin ont été également effectuées sous conditions statiques, afin d'étudier le changement de phase du lubrifiant.

MOTS-CLÉS : contrainte limite de cisaillement, lubrification élastohydrodynamique, contacts lubrifiés fortement chargés, mesure in situ, coefficient de frottement, transition vitreuse.

Laboratoire (s) de recherche : LAMCOS

Directeur de thèse : Philippe Vergne, Laetitia Martinie, David Philippon

Président de jury :

Composition du jury : BRUNETIERE Noël, Martinie Laetitia, PHILIPPON David, POLL Gerhard, SEABRA Jorge,

VERGNE Philippe